

AD-A037 441

PURDUE UNIV LAFAYETTE IND PROJECT SQUID HEADQUARTERS
LAMINARISCENT TURBULENT BOUNDARY LAYERS: EXPERIMENTS ON NOZZLE --ETC(U)
JAN 77 R L SIMPSON, C R SHACKLETON
SQUID-SMU-2-PU

F/6 20/4

N00014-75-C-1143

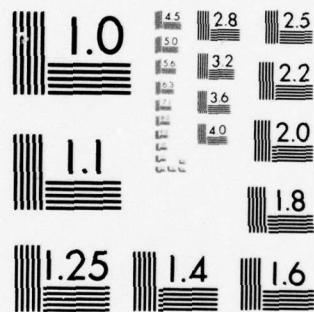
NL

UNCLASSIFIED

1 OF 2

AD
A037441





MICROCOPY RESOLUTION TEST CHART
NATIONAL BUREAU OF STANDARDS-1963-A

ADA 037441

12

PROJECT SQUID

TECHNICAL REPORT SMU-2-PU

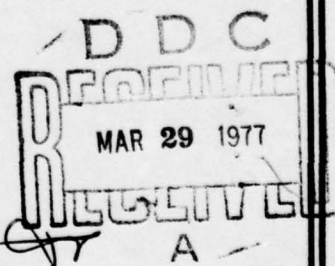
LAMINARISCENT TURBULENT BOUNDARY LAYERS: EXPERIMENTS ON NOZZLE FLOWS

by

ROGER L. SIMPSON AND C. R. SHACKLETON
SOUTHERN METHODIST UNIVERSITY
DALLAS, TEXAS

COPY AVAILABLE TO DDC DOES NOT
PERMIT FULLY LEGIBLE PRODUCTION

PROJECT SQUID HEADQUARTERS
CHAFFEE HALL
PURDUE UNIVERSITY
WEST LAFAYETTE, INDIANA 47907



Project SQUID is a cooperative program of basic research relating to Jet Propulsion. It is sponsored by the Office of Naval Research and is administered by Purdue University through Contract N00014-75-C-1143, NR-098-038.

This document has been approved for public release and sale;
its distribution is unlimited.

DDC FILE COPY

14 SQUID-SMU-2-FU

9 Technical Report SMU-2-PU ✓

P R O J E C T S Q U I D

A COOPERATIVE PROGRAM OF FUNDAMENTAL RESEARCH
AS RELATED TO JET PROPULSION
OFFICE OF NAVAL RESEARCH, DEPARTMENT OF THE NAVY

15 CONTRACT N00014-75-C-1143 NR-098-038

6 LAMINARISCENT TURBULENT BOUNDARY LAYERS:
EXPERIMENTS ON NOZZLE FLOWS

by

10 Roger L. Simpson and C. R. Shackleton
SOUTHERN METHODIST UNIVERSITY

11 January 1977

12 107p.

PROJECT SQUID HEADQUARTERS
CHAFFEE HALL
PURDUE UNIVERSITY
WEST LAFAYETTE, INDIANA 47907

403 617

This document has been approved for public release and sale; its
distribution is unlimited.

copy

LAMINARISCENT TURBULENT BOUNDARY LAYERS:
EXPERIMENTS ON NOZZLE FLOWS

by

Roger L. Simpson* and C. R. Shackleton**

ABSTRACT

ACCESSION FOR	
NTIS	Write Section <input checked="" type="checkbox"/>
DDC	Buff Section <input type="checkbox"/>
DRANDONCE	<input type="checkbox"/>
JUSTIFICATION	
BY	
SUBSCRIPTION/AVAILABILITY CODES	
Dist.	AVAIL. and/or SPECIAL
A	

Because a turbulent boundary layer in a nozzle undergoes strong acceleration, a laminariscient boundary layer with the benefit of a lower surface heat transfer rate can result for some short distance. Here and in a previous report (Simpson and Wallace, 1975) several phenomena which accompany laminariscence produced by strong acceleration are examined for nozzle-flow and sink-flow accelerational distributions, respectively. Several different type measurements of the structure of two nozzle-type flows are reported to determine how an initially normal turbulent boundary layer approaches the laminar-like state, including mean velocity and Reynolds stresses profiles, spectra, turbulent/non-turbulent interfacial structure, and wall bursting and sublayer spanwise spatial structure.

As a result of these experiments, it appears that the surface skin-friction is not reduced to laminar values in sink flows unless $K(=vU_{\infty}^2 du/dx)$ is greater than about 3.6×10^{-6} . In nozzle-type flows, K must also be greater than this value over a short distance in order to produce a short relaminarized region downstream. The large-eddy structure of the outer region governs the bursting frequency, the intermittent bulge passage frequency, and influences the wall flow behavior downstream. After the cessation of entrainment of free-stream fluid, these frequencies approach constant values. The wall spanwise structure appears to lag behind local conditions and to reflect upstream flow behavior. After retransition to a low acceleration turbulent boundary layer downstream, much larger spanwise scale structures are observed.

The entrainment rate of non-turbulent fluid decreases to zero at about the streamwise location at which the shape factor reaches a minimum value. The cessation of entrainment by the eruption and

* Professor of Mechanical Engineering, Southern Methodist University.

** Research Assistant, Dept. of Mechanical Engrg., Southern Methodist University.

and engulfment action of the large eddies can be traced to the reduction of available turbulence energy for diffusion to free-stream fluid. This reduction of available energy is due to the negative normal stresses turbulence energy production term. Spectral distributions of the streamwise fluctuation $F(n)$ possess a frequency region where $nF(n)$ is constant for laminar-like boundary layers at large K values.

TABLE OF CONTENTS

ABSTRACT	i
TABLE OF CONTENTS	iii
NOMENCLATURE	iv
1. INTRODUCTION	1
2. EXPERIMENTAL APPARATUS	2
3. EXPERIMENTAL RESULTS	11
3.1. Description of the test flows	11
3.2. Mean velocity profile measurements	13
3.3. Skin-friction results	21
3.4. Reynolds stresses distributions	25
3.5. Spectra measurements and dissipation estimates . . .	31
3.6. Wall bursting frequencies and spanwise structure . .	41
3.7. Intermittency measurements	58
4. DISCUSSION	65
5. CONCLUSIONS AND RECOMMENDATIONS	71
REFERENCES	73
APPENDIX A - Mean velocity and streamwise fluctuation profile data, flow C, linearly increasing K	76
APPENDIX B - Mean velocity and streamwise fluctuation profile data, flow D, nozzle flow	81
APPENDIX C - Errata for Report SMU-1-PU	87

NOMENCLATURE

A, B, C, D	constants.
$C_f/2$	$= \tau_w / \rho U_\infty^2$, friction factor.
E, e	mean and fluctuation voltages.
F(n)	spectral density defined by equation (9).
F, F_δ	defined by equations (18) and (20), respectively.
f, f'	U/U_∞ and $\partial f / \partial \eta$, respectively.
H	$= \delta^* / \theta$, shape factor.
K	$= \frac{\nu}{U_\infty^2} \frac{dU_\infty}{dx}$; also a constant in equation (12).
L_z	integral length scale defined by equation (14).
M	constant.
m	exponent in split-film calibration curve.
n	frequency, Hz.
n_{iy}	frequency of intermittent bulge passage at \bar{Y} .
dP/dx	pressure gradient.
$\frac{Q_i}{q}$	power dissipation in split-film sensor i. $= \overline{u^2} + \overline{v^2} + \overline{w^2}$.
$\hat{sR}_{\tau\tau}(z, T_s)$	normalized spatial cross-correlation of two τ surface fluctuation signals during sample time T_s .
$\hat{sR}(z)$	$\hat{sR}(z, T_s)$ as T_s becomes very large.
Re_θ	$= U_\infty \theta / \nu$, momentum thickness Reynolds number.
Re_λ	$= \frac{(\overline{u^2})^{1/2} \lambda}{\nu}$, microscale Reynolds number.
T_s	length of sample time.
t	time delay; time.

U_τ	$= (\tau_w/\rho)^{1/2}$, shear velocity.
$u, v, w,$	velocity fluctuations in the streamwise, normal, and spanwise directions.
U, V, W	mean velocities in the streamwise, normal, and spanwise directions.
$-\overline{uv}$	kinematic Reynolds shearing stress.
V_E	entrainment velocity.
x, y, z	cartesian co-ordinates in the streamwise, normal, and spanwise directions, respectively.
\bar{Y}	distance from the wall to where $\gamma = 0.5$.

SUBSCRIPTS

b	denotes "bursting" value.
eff	denotes effective cooling velocity.
i	split-film sensor index.
l	denotes linearized signal.
w	denotes wall value.
∞	free-stream condition.

GREEK

α	constant in equation (10); split-film probe yaw parameter.
γ	intermittency, long-time averaged fraction of time that the flow is turbulent.
δ	$\delta_{0.99} = y$ where $f = 0.99$; $\delta_{0.995} = y$ where $f = 0.995$.
δ^*	$= \int_0^\infty \left(1 - \frac{U}{U_\infty}\right) dy$, displacement thickness.
ϵ	dissipation rate
η	$= yU_\infty/\nu$
θ	$= \int_0^\infty \frac{U}{U_\infty} \left(1 - \frac{U}{U_\infty}\right) dy$, momentum thickness.

λ	$= (15\overline{vu^2}/\epsilon)^{1/2}$, a turbulence microscale.
λ_z	spanwise wavelength in wall sensors cross-correlations.
$\lambda_{z1}^+, \lambda_{z2}^+$	defined by equations (15).
ν	kinematic viscosity.
ρ	density.
σ	standard deviation for intermittency distribution.
τ	shearing stress.
ϕ	angle of flow incidence to split-film probe.
Ω	logarithmic equation (5) constant.

1. INTRODUCTION

The strong acceleration of turbulent boundary layers in a nozzle can produce the benefit of a substantially reduced convective heat transfer rate when relaminarization occurs (Moretti and Kays, 1965). The accelerational parameter K , defined as $\nu U_\infty^{-2} dU_\infty/dx$, must increase to a value in excess of about 3.6×10^{-6} (Kline et al., 1967) for relaminarization to occur. The practical consideration that flow acceleration extends over a finite length then requires that K decrease to zero downstream. Narasimha and Sreenivasan (1973) reexamined the behavior of this type of flow from the time-averaged results of many previous experiments. However, there is little information on the flow structure that would explain the mechanisms for relaminarization. Exceptions are the space-time correlations of Blackwelder and Kovaszny (1972) for the large-scaled motion and the wall region structure reported by Schraub and Kline (Kline, et al., 1967).

The work described here is the second part of a program to provide experimental flow structure information for strongly-accelerated turbulent boundary layers under different K distributions. In the first part (Simpson and Wallace, 1975) results were obtained for two asymptotic sink-flow type turbulent boundary layers with constant K distributions (flow A, $K = 2.17 \times 10^{-6}$; flow B, $K = 3.19 \times 10^{-6}$). Here results are presented for a flow in which K increases linearly with x (flow C) and a flow in which K increases linearly with x to a maximum value, stays constant at this level for a short distance, and then decreases linearly with x (flow D). Flow C models the rapid increase

in K encountered in nozzles while flow D models both the increase and decrease in K . Since the acceleration of both flows took place in the same length of wind tunnel test section, dK/dx for the increasing K portion of flow D was more than double dK/dx for flow C.

The type of measurements reported here for flows C and D are similar to those obtained for flows A and B. In addition to mean velocity and Reynolds' stresses measurements, spectra of the streamwise fluctuations were obtained. This was partly motivated by the presence of a flat $nF(n)$ spectrum for flow B and the question as to whether this behavior accompanies true relaminarization. Other measurements are the turbulent/non-turbulent interfacial intermittency and frequency of passage of intermittent turbulent bulges, the wall "bursting" frequencies or rate of passage of eddies over the wall, and the spanwise spatial structure at the wall. This latter group of measurements provides further insight as to the roles that the bursting behavior, spanwise structure, and intermittency play in relaminarization. Since these measurements have been obtained for four different K distribution flows on the same apparatus, the effect of the K distribution on the developing flow structure can be determined.

2. EXPERIMENTAL APPARATUS

In general, all of the apparatus and instrumentation described by Simpson and Wallace (1975) for flows A and B were used for flows C and D. The SMU wind tunnel with a sixteen feet long, three feet wide, test section was used to produce the desired boundary layer on the flat bottom wall by adjusting the plexiglas top wall. In the current

experiments the freestream flow upstream of the acceleration was uniform within 0.066% in the spanwise direction and within 1% in the vertical direction, with a streamwise turbulence intensity of 0.6% at 9.1 fps. At the tunnel exit the free-stream streamwise turbulence intensity dropped to below 0.55% and 0.5% for flows C and D, respectively. Of this intensity, about 0.5% was due to unsteadiness at about 20 Hz. Figure 1 is a side view schematic of the test section with the upper wall locations for flows A, C, and D. In all four flows the flat upper wall was 15 inches above the test wall at the entrance and 19.5 inches above it at the 96 inches location. For flow C the parabolic-shaped upper wall section began at 96 inches and was 1.72 inches above the test wall at the exit at 190.8 inches. For flow D the antisymmetric ogee-shaped upper wall began at 96 inches and was 1.84 inches above the test wall at 189.7 inches. All experimental data were obtained with the temperature maintained constant at $77 \pm 1/2^\circ\text{F}$ and a constant stagnation pressure at the exit.

The 1/4 inches blunt leading edge trip on the test wall and the boundary layer smoke injection arrangement upstream of the trip were the same as used for flows A and B. The same smoke generation system with a mean particle size of about 1 micron was used when smoke was used to mark turbulent fluid upstream of relaminarization. For these intermittency measurements the optics and traversing equipment of the SMU laser anemometer were used as for flows A and B.

Standard Thermo-Systems, Inc., model 1050 constant temperature anemometers, model 1055 linearizers, model 1057 signal conditioners,

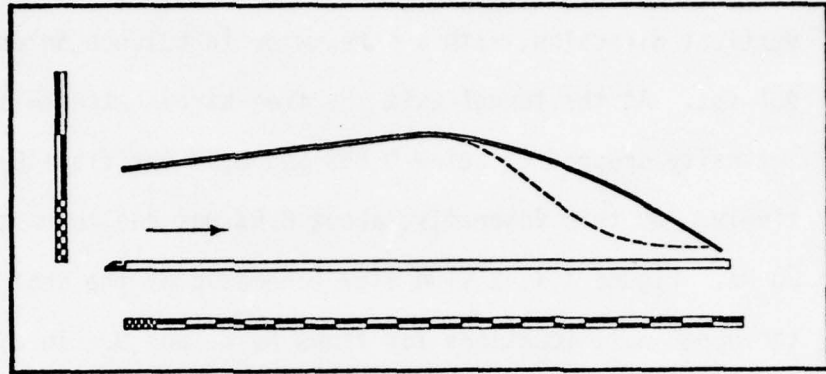


Figure 1. Sideview schematic of the test section: solid line, flow C; dashed line, flow D. Major divisions on abscissa and ordinate: 10 inches. Note 2:1 scale ratio.

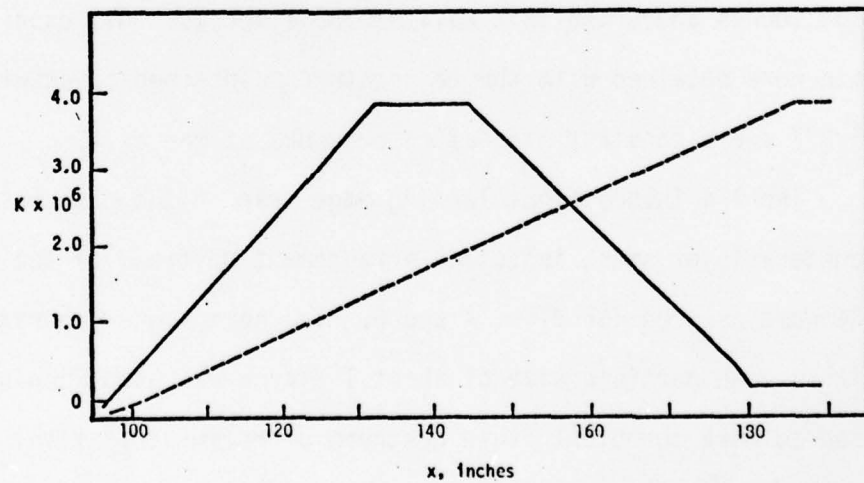


Figure 2. K distributions for flows C and D: flow C - dashed line; flow D - solid line.

and model 1015C correlator were used. A TSI model 1274-10 boundary layer hot-film probe was used in measuring the mean and streamwise fluctuation velocities in flow C while a model 1218-T1.5 boundary layer hot-wire probe was used for flow D. The sensing element for the hot-film is a 0.001 inches diameter platinum coated quartz rod with a sensing length of 0.04 inches. The 0.00015 inches diameter platinum-plated tungsten wire had a 0.05 inches sensing length. Based on the Collis and Williams (1959) equation for the anemometer bridge output calibration, the linearizers were adjusted. The linearizer output was directly checked with the known calibrator velocity for accuracy and linearity, the maximum tolerable deviation being less than about 1/2%. Consequently, the uncertainty on velocity measurements is about $\pm 1/2\%$.

The split-film probe (TSI model 1287) was used to determine U , V , $\overline{u^2}$, $\overline{v^2}$, and $-\overline{uv}$ for flow C. This relatively new hot-film probe was selected because of its relatively small size since the boundary layers under study were thin. The split-film sensor is a modification of the basic platinum coated cylindrical film sensor. Two electrically independent films each cover one-half of the circumference of a 0.006 inches diameter quartz rod. Each film is operated by a separate constant temperature circuit. The non-uniform heat transfer distribution around a constant temperature cylinder is utilized to measure the fluctuating components of the instantaneous velocity vector. To avoid thermal variations in the substrate the sensors must be held at closely identical temperatures. The resulting output

voltages are used in the same manner as those from an x-wire probe to determine mean and fluctuation quantities.

Using a right-handed coordinate system, the plane of the two splits that separate the two platinum films from one another are in the x-z plane, being nominally parallel to the test wall in these experiments. Following Spencer and Jones (1971), the power dissipated in each film can be related to the velocity by

$$Q_i = (A + BU_{\text{eff}}^m)(1 + \alpha_i \frac{V}{U_{\text{eff}}}) \quad i = 1, 2$$

neglecting axial cooling. The constants A, B, and m were obtained by velocity calibration as done for a single sensor probe; α_i was determined by azimuthal yaw calibration. The power dissipated is proportional to the square of the anemometer bridge output minus the zero flow voltage:

$$E_i = M_i(Q - Q_0)_i = M_i U_{\text{eff}}^m (1 + \alpha_i \frac{V}{U_{\text{eff}}})$$

The voltage E_i can be linearized directly in terms of U_{eff} using $m = 0.5$. Thus

$$E_{\ell i} = M_{\ell i} E_i^{1/m} = MU_{\text{eff}} (1 + \alpha_i \frac{V}{U_{\text{eff}}})^2$$

or when neglecting higher ordered terms the instantaneous voltage is

$$E_{\ell i} + e_{\ell i} = MU_{\text{eff}} [1 + \frac{u}{U_{\text{eff}}} + 2\alpha_i \frac{(V + v)}{U_{\text{eff}}}]$$

When calibrated in a steady flow

$$\frac{(E_{\ell i})}{(E_{\ell i})_{\phi=0}} = 1 + 2\alpha_i \sin\phi$$

Second order effects, which occur for angles larger than 20° , are negligible for this particular flow.

The following calibration procedure was repeated before and after each velocity profile was obtained. The probe was mounted in a specially constructed support with orientation adjustment, the "dial calibrator," that permitted a $\pm 50^\circ$ rotation of the split-film sensor about a fixed location. The sensor was supported over the potential core of the near jet produced by a TSI model 1125 calibrator. The dial calibrator was used for both the velocity and azimuthal yaw calibrations. The uncertainty in the angle was less than 0.2° . The use of the split-film probe requires closely equal temperatures of the films, so that very fine overheat adjustment of one film is mandatory to match temperatures.

Both films were exposed to 77° air flow directed along the plane of splits. Cold resistances were measured and found to be about 11 and 12 ohms. Both films were then overheated by a factor of 0.5. One film was left without further adjustment while the other film overheat was adjusted using a 1 ohm precision ten turn potentiometer. The temperature matching was achieved when the ratio of the two output bridge voltages remained constant (within 0.2%) as the velocity directed along the plane of the splits was varied from 9 fps to 70 fps. Temperature matching was checked again immediately after taking data from flow C in order to estimate any possible anemometer drift.

The bridge outputs were then each linearized and checked with the known calibrator velocity. A calibration equation of the form:

$$E_{li} = C_i U_{eff} + D_i$$

was determined from a least squares fit with less than 4% standard deviation. The background noise level in the steady laminar calibrator flow was also measured. This noise took the form of a triangular wave with no phase change between channels. We suspect the noise was due to vortex shedding off of the relatively large diameter sensor. The probe was then calibrated for several azimuthal yaw angles to determine α_i . Yaw characteristics were found to be independent of the magnitude of U_{eff} .

The equations governing the split film are a combination of the above equations

$$E_{li} + e_i = C_i U_{eff} [1 + u/U_{eff} + 2\alpha_i(V + v)/U_{eff}] + D_i$$

$$i = 1, 2$$

or
$$E_{l1} = C_1 [U_{eff} + 2\alpha_1 V] + D_1$$

and
$$E_{l2} = C_2 [U_{eff} + 2\alpha_2 V] + D_2$$

Since C_i , D_i , and α_i are known from calibration, then E_{l1} and E_{l2} are measured and U_{eff} and V are derived. The angle of flow, ϕ , at a point is then found from

$$\sin\phi = V/U_{eff}$$

Similarly, the fluctuation quantities are found from:

$$\begin{aligned} \overline{(e_{l1})^2} &= C_1^2 \overline{u^2} + 4C_1^2 \alpha_1 \overline{uv} + (2C_1 \alpha_1)^2 \overline{v^2} \\ \overline{(e_{l1} + e_{l2})^2} &= (C_1 + C_2)^2 \overline{u^2} + 4(C_1 \alpha_1 + C_2 \alpha_2)(C_1 + C_2) \overline{uv} + (C_1 \alpha_1 + C_2 \alpha_2)^2 \overline{v^2} \\ \overline{(e_{l1} - e_{l2})^2} &= (C_1 - C_2)^2 \overline{u^2} + 4(C_1 \alpha_1 - C_2 \alpha_2)(C_1 - C_2) \overline{uv} + (C_1 \alpha_1 - C_2 \alpha_2)^2 \overline{v^2} \end{aligned}$$

$\overline{e_1^2}$, $\overline{(e_{\lambda 1} + e_{\lambda 2})^2}$, and $\overline{(e_{\lambda 1} - e_{\lambda 2})^2}$ were measured, corrected for the above mentioned noise, and used to solve simultaneously for $\overline{u^2}$, $-\overline{uv}$, and $\overline{v^2}$ using the latter equations. These results are discussed in section 3.4 below.

The traversing mechanism used for the boundary layer velocity measurements was mounted on the supporting frame for the upper wall and provided for precise positioning of the probe sensors as described by Strickland and Simpson (1973). A cathetometer was used to accurately locate the probe sensor from the wall within an uncertainty of about ± 0.001 inches. The detailed streamwise free-stream velocity distributions were obtained using a TSI model 1210-20 hot-film probe (0.002 inches diameter platinum-coated quartz rod) attached to a probe support rod inserted from the tunnel exit or mounted on the toy racing car shown in figure 3 of Simpson and Wallace (1975). The car was easily positioned along the flow by fishing line. It could not be used near the exit since substantial flow blockage effects would have been produced.

The flush surface mounted hot-film sensors for the wall "bursting" and spanwise measurements are described in detail by Strickland and Simpson (1973). The basic sensing part is a very thin layer of platinum (Engelhard Ind. Liquid Bright Platinum #05) fired on the end of a 2mm diameter quartz rod. Gold leads (Engelhard Ind. Gold Alloy Paste A-1199) were fired on the sides of the rod and short wire leads were soldered to the gold. A casing made from 1/4 inch diameter plexiglas rod was used to protect the sensor from damage due to handling.

The resulting unit was mounted in the wind tunnel wall with the platinum portion flush with the test wall. A unit containing two flush surface 0.020 inches diameter platinum sensors was also fabricated to permit one of the sensors to be traversable. This unit was used in the surface spanwise structure measurements and is described in more detail by Simpson and Wallace (1975). All of these sensors were operated at an overheat ratio of 0.03 in the current experiments. A higher overheat ratio would have permanently damaged the sensors. The constant temperature frequency response for each sensor was determined to be down 3 db at 4 KHz using the method of Freymuth (1967).

Other electronic equipment included Krohn-Hite model 3202 and 330B filters, HP model 400E rms voltmeters, an Anadex model CF-600 timer-frequency counter, a SAICOR model 41 digital correlation and probability analyzer, an Applied University Research four-channel FM tape recorder (response down 3 db at 2 KHz), a voltage comparator or schmitt trigger using an operational amplifier integrated circuit and a multiplier using an Analog Devices AD533 JH integrated circuit trimmed to within $\pm 1\%$ fullscale nonlinearity error. A true integrating voltmeter consisting of a voltage-controlled oscillator (Tektronix FG501 Function Generator) and a digital counter (Tektronix DC503 Universal Counter) was found to be superior to RC-type meter circuits used in most voltmeters. A HP 5451A/71A Fast Fourier Analyzer System was used to process data recorded on the tape recorder.

For the intermittency measurements in flow C, the laser optics, and photo-multiplier tube of the SMU laser anemometer (Simpson, et al., 1974) was used to scatter light from the smoke filled boundary layer

and collect the signal. A focal volume of 0.32 mm diameter and 3.56 mm long was produced from a laser beam 1.1 mm in diameter at the $1/e^2$ intensity locations. Since the laser anemometer is mounted on a single traversable cart, accurate location of the focal volume could be determined.

3. EXPERIMENTAL RESULTS

3.1 Description of the test flows

Because of the strong influence of acceleration on these boundary layers, careful measurements of the freestream velocity were made every one inch along the test section using the rake and car probe mounts. For flow C the following velocity and K distributions were obtained:

$$1/U_{\infty} = -1.525 \times 10^{-2} + (2.307 \times 10^{-3})(x) - (1.133 \times 10^{-5})(x^2)$$

for $96 \leq x \leq 178$ inches and

$$1/U_{\infty} = 4.273 \times 10^{-1} - (2.466 \times 10^{-3})(x) + (1.473 \times 10^{-6})(x^2)$$

for $178 \leq x \leq 190$ inches with

$$K = -4.622 \times 10^{-6} + (4.5427 \times 10^{-8})(x)$$

for $96 \leq x \leq 185$ and $K = 3.83 \times 10^{-6}$ for $186 \leq x \leq 191$ inches. U_{∞} is in fps and x is in inches. The maximum deviation of U_{∞} data from these equations is less than 0.4% while the rms deviation is about 0.1%. The different x ranges for the $1/U_{\infty}$ distributions and their respective K distribution reflect the fact that the upstream velocity equation produces K values in closer agreement with data for $178 < x < 185$ inches. The single-sample uncertainty (Kline and McClintock, 1953) in K at 20:1 odds is about 2%.

For flow D, with both increasing and decreasing K regions, the following velocity and K distributions are presented:

$$1/U_{\infty} = 9.898 \times 10^{-2} + (6.568 \times 10^{-5})(x)$$

for $64 < x < 96$ inches

$$1/U_{\infty} = -1.449 \times 10^{-1} + (5.167 \times 10^{-3})(x) - (2.675 \times 10^{-5})(x^2)$$

for $96 < x < 132$ inches

$$1/U_{\infty} = 3.243 \times 10^{-1} - (1.917 \times 10^{-3})(x)$$

for $132 < x < 144$ inches

$$1/U_{\infty} = 8.497 \times 10^{-1} - (9.1869 \times 10^{-3})(x) + (2.5138 \times 10^{-5})(x^2)$$

for $144 < x < 180$ inches and

$$1/U_{\infty} = 2.475 \times 10^{-2} - (7.8147 \times 10^{-5})(x)$$

for $180 < x < 190$ inches.

$$K = -1.32 \times 10^{-7} \text{ for } 64 < x < 96 \text{ inches}$$

$$K = -1.037 \times 10^{-5} + (1.0737 \times 10^{-7})(x) \text{ for } 96 < x < 132 \text{ inches}$$

$$K = 3.85 \times 10^{-6} \text{ for } 132 < x < 144 \text{ inches}$$

$$K = 1.8438 \times 10^{-5} - (1.009 \times 10^{-7})(x) \text{ for } 144 < x < 179 \text{ inches}$$

$$K = 1.568 \times 10^{-7} \text{ for } 180 < x < 190 \text{ inches}$$

The maximum deviation of U_{∞} data from these equations is less than 1% while the rms deviation is about 0.2%. The discontinuity in K at the ends of each region is of the order of 10^{-7} . The single-sample uncertainty in K is about 4%. The smoothed K distributions for both flows C and D are shown in figure 2.

As was done for flows A and B, observations were made to assess the three-dimensionality of flows C and D. Because of the care used in adjusting the spanwise elements of the upper wall parallel to the

test wall, the thin boundary layers in a large aspect ratio channel, and the fact that the flow was accelerating, minimal three-dimensional effects were expected. At the 88 inches location there was less than 1% spanwise difference in the momentum thickness, so no gross three-dimensionality due to the upstream flow was present. The side wall boundary layers of the converging section for each flow tended to remain at about a constant thickness due to the reduction of the side wall surface area simultaneously with acceleration of the freestream. Thus convergence or divergence effects on the test wall boundary layer by the side wall boundary layers appears to be negligible.

As discussed in section 3.3 below, the skin friction was deduced by analyzing mean velocity profiles near the wall. The smoothed "best estimate" skin friction coefficients and other required and experimentally deduced quantities were used to check the balance of terms in the two-dimensional momentum integral equation. In both flows C and D this equation was balanced well within the uncertainty of the most uncertain term, $d\theta/dx$, or about 5% of that term.

3.2 Mean velocity profile measurements

Figure 3 shows the mean velocity profile results for flow C. A distinct logarithmic region exists for each upstream profile, with the last evidence of any logarithmic region occurring at about station 160 inches. As shown in figure 4, the shape factor H is near a minimum at station 165 inches. The wake-like tail of each profile near the freestream is observed to progressively decrease in wake strength,

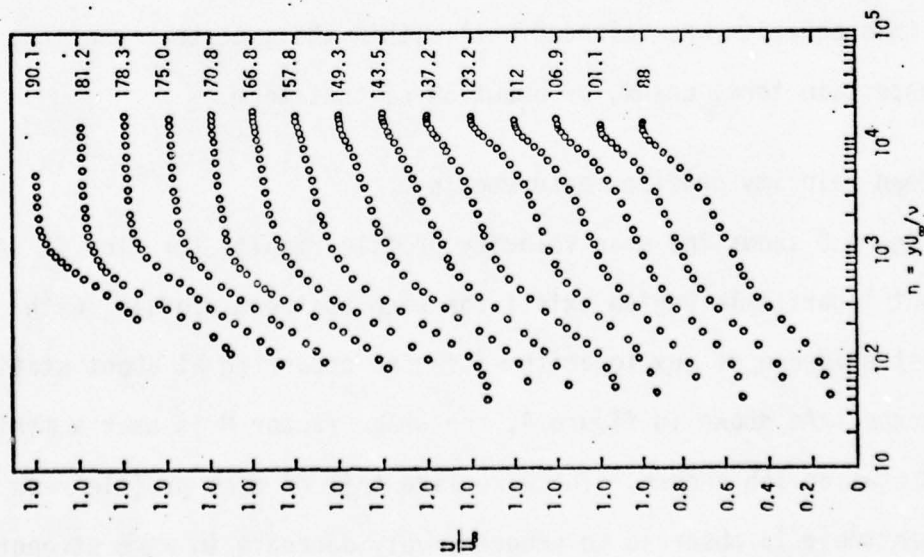


Figure 3. Experimental mean velocity profiles for flow C. Linearly increasing K. Note displace ordinates. Station position in inches at right of each profile.

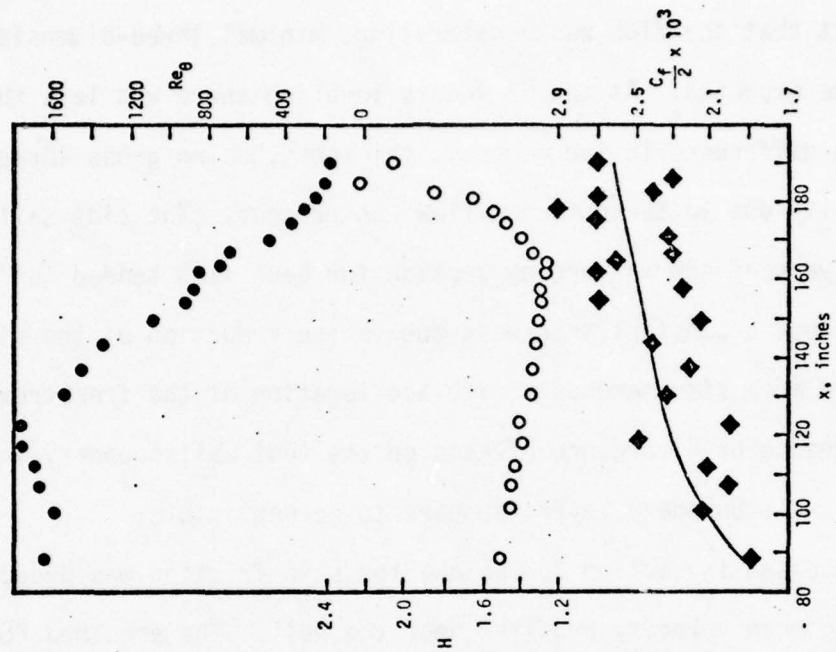


Figure 4. Re_0 , H , and $C_f/2$ for flow C. Friction factors from table 1: solid symbols - wall profile results; line - best estimate curve.

Station (inches)	U_{∞}^a (fps)	$(K \times 10^6)^b$	Re_{θ}	H	$\delta_{0.99}$ (inches)	$\frac{C_f}{2} \times 10^3$	
						wall profile $\pm 15\%$	best estimate ^c $\pm 15\%$
88.0	8.94	-0.59	1647	1.505	2.62	1.90	1.93 ^d
101.1	8.51	-0.029	1600	1.456	2.81	2.15	2.14
106.9	8.59	0.234	1681	1.450	2.91	2.04	2.20
112.0	8.80	0.466	1698	1.437	2.90	2.12	2.23
117.9	9.27	0.733	1765	1.388	2.91	2.48	2.27
123.2	9.71	0.974	1778	1.407	2.89	2.01	2.30
130.6	10.06	1.31	1546	1.344	2.74	2.32	2.34
137.2	10.79	1.61	1465	1.341	2.62	2.2	2.38
143.5	11.42	1.90	1353	1.320	2.53	2.40	2.41
149.3	12.10	2.16	1096	1.313	2.24	2.15	2.44
154.5	13.36	2.40	923	1.290	2.02	2.7	2.46
157.8	14.00	2.55	890	1.307	1.94	2.25	2.48
162.0	15.53	2.74	868	1.274	1.77	2.7	2.50
164.2	16.67	2.84	747	1.262	1.60	2.6	2.51
166.8	17.89	2.96	697	1.335	1.47	2.30	2.52
170.8	20.42	3.14	484	1.407	1.09	2.32	2.54
175.0	23.98	3.33	373	1.481	0.698	2.70	2.56
178.3	29.62	3.48	314	1.559	0.395	2.9	2.57
181.2	33.12	3.61	257	1.647	0.302	2.7	2.58
182.3	36.11	3.66	264	1.850	0.197	2.4	2.58
185.8	44.46	3.82	201	2.223	0.098	2.3	2.60
190.1	80.30	3.83	182	2.049	0.048	2.7	2.61

- (a) measured when velocity profile measured.
(b) from least squares fit of rake and cart data.
(c) with exceptions noted, from faired curve of data on figure 4.
(d) determined from logarithmic velocity profile, equation (5).

Table 1. Values of parameters along flow C.

the wake strength being defined as the maximum deviation of the measured velocity profile from the extrapolated logarithmic region profile. Downstream of the location of the minimum H the velocity profiles take on an increasingly more laminar-like character, although the streamwise fluctuation measurements clearly show that a relatively large turbulence intensity still exists. Since the last 5 inches of the test flow has a constant K of about 3.83×10^{-6} , this is the only region where constant K asymptotic velocity profile similarity of $f(=U/U_\infty)$ and $\eta(=yU_\infty/\nu)$ is possible. In this region the velocity profiles for $\eta > 1000$ are similar well within a deviation of 0.01 f . However, the streamwise fluctuation intensity profiles discussed in section 3.4 do not possess similarity in this region and H and Re_θ do not reach constant values, as required for true asymptotic similarity (Simpson and Wallace, 1975). Re_θ drops well below the value of about 360 (Kays 1966) where normal transition from a laminar to turbulent boundary layer occurs, so true laminar behavior could be expected downstream had the test section been longer and the level of acceleration maintained.

Flow D also has a linearly increasing K distribution but only for $x < 132$ inches. dK/dx is more than twice that for flow C. As in flow C, the initial upstream logarithmic velocity profile progressively decays downstream. Figure 5 shows that the wake strength also decreases to zero near the minimum H location, shown at about 135 inches in figure 6. The location of the minimum H occurs in the region where K is a maximum, while in flow C it occurs at a much

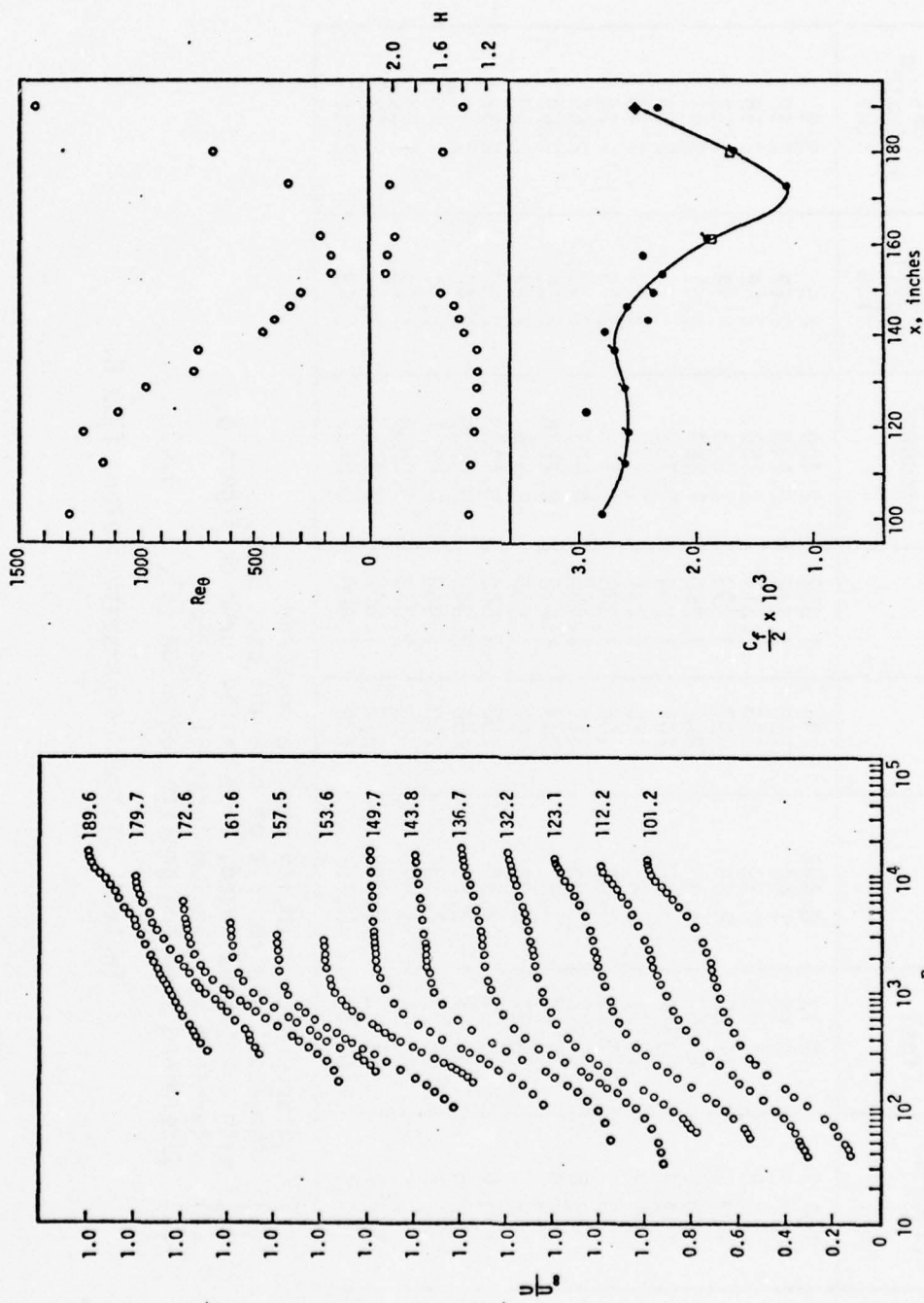


Figure 5. Mean velocity profiles for flow D. Streamwise location in inches to right of each profile. Note displaced ordinate scales.

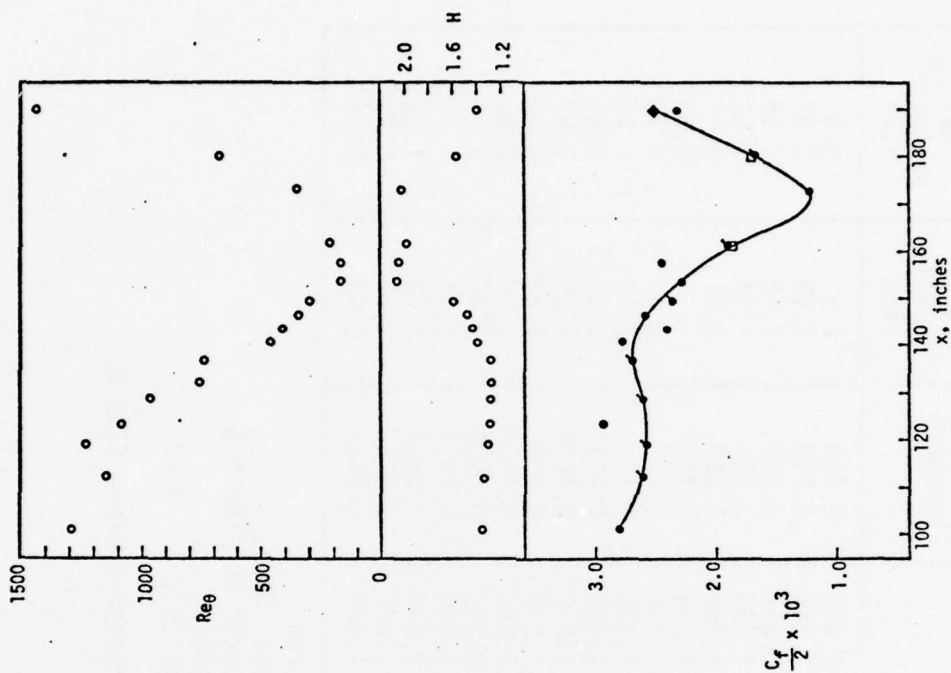


Figure 6. Re_θ , H , and $C_f/2$ for flow D. $C_f/2$ values from table 2: \circ , unshifted wall profile; \diamond , shifted wall profile; \diamond , logarithmic profile with $K = 0.4$; \square , momentum integral equation.

Station (inches)	U_{∞}^a (fps)	$(K \times 10^6)^b$	Re_{θ}	H	$\delta_{0.99}$ (inches)	$\frac{C_f}{2} \times 10^3$	
						wall profile $\pm 10\%$	best estimate ^c $\pm 10\%$
101.2	9.12	0.495	1294	1.352	2.409	2.9	2.9
112.2	9.55	1.68	1156	1.346	2.243	2.62	2.62
118.8	11.26	2.39	1236	1.311	2.168	2.58	2.58
123.1	11.22	2.85	1087	1.293	2.053	2.94	2.58
128.6	13.53	3.44	965	1.286	1.889	2.61	2.61
132.2	13.72	3.85	761	1.264	1.756	?	2.65
136.7	16.71	3.85	740	1.281	1.477	2.70	2.70
140.7	17.75	3.85	464	1.388	1.113	2.79	2.70
143.8	21.02	3.85	419	1.436	0.908	2.42	2.65
146.8	22.67	3.62	347	1.478	0.7544	2.60	2.59
149.7	26.37	3.33	307	1.583	0.535	2.37	2.49
153.6	30.68	2.94	168	2.069	0.1183	2.30	2.32
157.5	37.81	2.55	166	2.043	0.0900	2.46	2.12 ^d
161.6	48.39	2.13	219	1.980	0.0871	1.91	1.87 ^d
172.6	83.55	1.02	355	2.028	0.0984	1.22	1.22 ^d
179.7	94.82	0.306	677	1.567	0.1436	1.67	1.72 ^d
189.6	102.1	0.157	1432	1.408	0.2477	2.43	2.54 ^e

- (a) measured when velocity profile measured.
(b) from least squares fit of rake and cast data.
(c) with exceptions noted, from faired curve on figure 6.
(d) determined by momentum integral equation.
(e) determined from log profile, equation (5), $\Omega = 0.40$.

Table 2. Values of parameters along flow D.

lower K value. Downstream the profiles assume an increasingly more laminar-like character as Re_θ drops below 360 until about 157.5 inches, even though K decreases downstream of 144 inches. No profile similarity is observed.

Between 157.5 inches and about 172.6 inches the momentum and displacement thicknesses, θ and δ^* , remain about constant, giving rise to about a constant shape factor ($H \equiv \delta^*/\theta$) of about 2.0. As noted in section 3.7 below, intermittency measurements downstream of 157.5 inches indicate that considerable turbulence is redeveloping. At the 189.6 inches location a thick logarithmic region $500 < \eta < 5000$ is observed, so that this flow is developing into a typical low acceleration turbulent boundary layer. The wake strength is also observed to be increasing.

Simpson and Wallace (1975) found that for each of flows A and B the location of the H minimum was closely related to where the wake strength was zero and where entrainment of free-stream fluid ceased. For flows C and D, the mass flux in each boundary layer as reflected by $U_\infty(\delta - \delta^*)$ increases until about 165 inches and 135 inches, respectively, as shown in figures 7 and 8. This parameter decreases downstream in both flows but again increases downstream of about 157.5 inches in flow D as a low acceleration turbulent boundary layer develops. These plots of experimentally deduced values indicate that there was entrainment of non-turbulent fluid into each boundary layer until the minimum H locations. As in the cases of flows A and B, the intermittency measurements discussed below indicate that after the

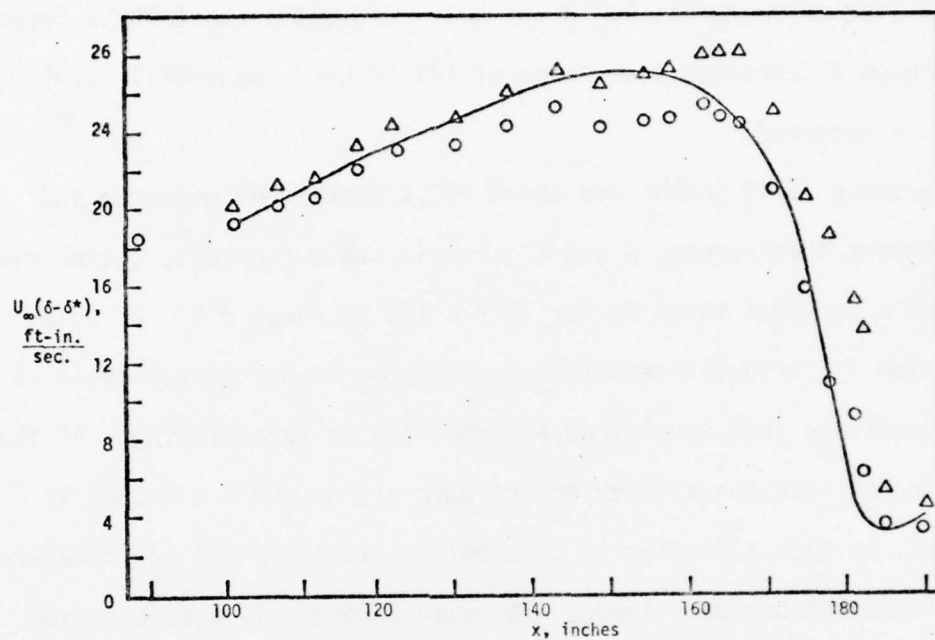


Figure 7. Mass flux in boundary layer of flow C, $U_\infty(\delta - \delta^*)$: \circ , $\delta = \delta_{0.99}$; Δ , $\delta = \delta_{0.995}$. Solid line - equation (21) results.

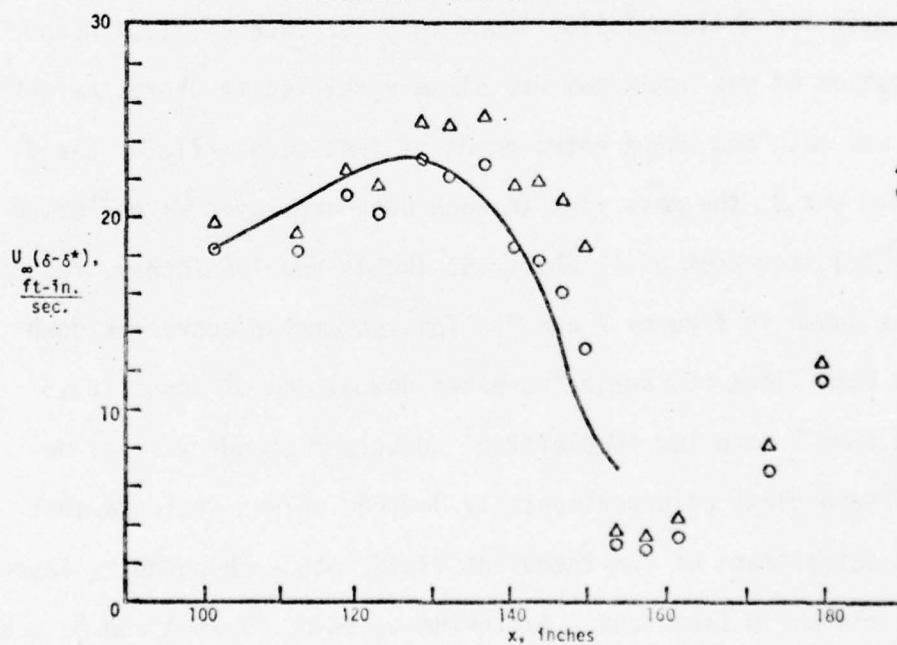


Figure 8. Mass flux in boundary layer of flow D, $U_\infty(\delta - \delta^*)$: \circ , $\delta = \delta_{0.99}$; Δ , $\delta = \delta_{0.995}$. Solid line - equation (21) results.

cessation of entrainment the intermittent turbulent/non-turbulent region lies outside δ . Thus there is no mean velocity gradient $\partial U/\partial y$ and no wake-like tail in this region and no mechanism for engulfment of non-turbulent fluid by the intermittent bulges is possible. The model proposed by Simpson and Wallace for the entrainment process in a strongly accelerated boundary layer is discussed in section 4 below.

3.3 Skin-friction results

The skin-friction coefficient $C_f/2$ was primarily determined by two methods: the velocity profile near the wall and the logarithmic velocity profile relationship for unaccelerated flow regions. The momentum integral equation

$$\frac{C_f}{2} = \frac{d\theta}{dx} + KRe_\theta (2 + H) \quad (1)$$

was used some for flow D when both terms of the right side were positive and relatively certain.

The velocity profile near the wall can be derived from the differential momentum equation, neglecting the convective and turbulent transport terms:

$$\nu \frac{\partial^2 U}{\partial y^2} = \frac{1}{\rho} \frac{dP}{dx} = \frac{-U_\infty^3 K}{\nu} \quad (2)$$

Integrating equation (2) produces

$$\frac{C_f}{2} = \frac{\partial f}{\partial \eta} + K\eta \quad (3)$$

and the velocity profile upon integration of equation (3)

$$\frac{U}{U_\infty} = f = \frac{C_f}{2} \eta - \frac{K\eta^2}{2} \quad (4)$$

Equation (4) was used with experimental velocity measurements for $5 \leq y^+ = \eta \sqrt{C_f/2}$ to determine $C_f/2$. Oka and Kostić (1972) noted that hot-film and hot-wire measurements are strongly influenced by conduction to the test wall for $y^+ < 4$. For velocity profiles with logarithmic regions it is known that equation (4) does not well describe the velocity profile for $y^+ > 6$, so only points in the range $5 < y^+ < 6$ were used. For the more laminar-like profiles experimental data with $y^+ > 6$ were also used.

Logarithmic velocity profiles in unaccelerated or weakly accelerated flow regions are described by the relation

$$\frac{U}{U_\infty \sqrt{\frac{C_f}{2}}} = \frac{1}{\Omega} \ln \left| \eta \left(\frac{C_f}{2} \right)^{1/2} \right| + C \quad (5)$$

where $\Omega = 0.40 (Re_\theta/6000)^{-1/8}$ (Simpson, 1970) for low Reynolds number boundary layers with $Re_\theta < 6000$. A fit of equation (5) to experimental data was made for the two upstreammost profiles of flow C and to the downstreammost profile of flow D. In the latter case $\Omega = 0.40$ was used since a large logarithmic region that normally accompanies high Reynolds number boundary layers was observed. Results using this latter method are about $\pm 10\%$ uncertain.

For flow C the 0.001 inches diameter cylindrical hot-film sensor was located from the test wall within an uncertainty of about 0.001 inches. Considering the $\pm 1/2\%$ uncertainty of the velocity, the $C_f/2$ values shown in figure 4 appear to be about $\pm 15\%$ uncertain at 20:1 odds. This uncertainty value seems reasonable due to the scatter

of the data. The logarithmic velocity profile results from equation (5) are in close agreement with these results.

For flow D the 0.00015 inches diameter hot-wire sensor was located from the test wall with somewhat more uncertainty than for flow C since the wire was more difficult to illuminate and to observe by the cathetometer. This more fragile sensor was located at a safe distance of about 0.005 inches from the wall to prevent breaking the wire. Data from this smaller diameter sensor are less susceptible to velocity gradient effects so the near wall velocity profiles for $y^+ > 4$ are believed to be of higher quality than those of flow C. For each velocity profile point a least squares fit of equation (4) to the five surrounding data points was made to deduce the slope $\partial f / \partial n$ at that point. $C_f/2$ can be eliminated from equations (3) and (4) to produce

$$\eta = \frac{-\frac{\partial f}{\partial n} + \sqrt{\left(\frac{\partial f}{\partial n}\right)^2 + 2Kf}}{K} \quad (6)$$

from which the proper sensor distance from the test wall could be computed from K , f , and $\partial f / \partial n$. For flow D equation (6) was used to determine the required change in the y direction for a self-consistent velocity distribution near the wall. Values within about 5% of one another were obtained for successive points in a given velocity profile. As given in Appendix B these shifts in the y direction are no more than ± 0.005 inches and therefore are reasonable.

Figure 6 shows relatively less scatter in the wall profile results than shown for flow C, thus an estimated uncertainty of $\pm 10\%$

seems reasonable. The logarithmic profile $C_f/2$ result at 189.6 inches is in good agreement with the $C_f/2$ result from equation (4) with no y direction shifting. Results from equation (1) at 161.6 and 179.7 inches are also in good agreement with the wall profile results.

Smooth curves of "best estimate" values for $C_f/2$ are shown on figures 4 and 6 with values given in Tables 1 and 2. While these curves were just faired among the points shown on those figures within about 15% and 10%, respectively, they are probably representative of the variation of $C_f/2$ along each flow. From the laminar sink flow (Schlichting, 1968), i.e. a constant K flow, one can obtain the expression

$$\frac{C_f}{2} = \sqrt{\frac{4}{3}} K \quad (7)$$

so for the maximum K of about 3.83×10^{-6} achieved in these two flows, $C_f/2 = 2.26 \times 10^{-3}$. Near the maximum K for each of flows C and D the experimental $C_f/2$ values are above this value as they should be since considerable turbulent momentum transport is still present. While one cannot exactly compare results from different K distributions, it is interesting that the experimental results shown in figure 6 for flow D are always greater than or about equal to those given by equation (7) with the local K value. In the region near 165 inches where the turbulence intermittency is near zero at the wall, as discussed in section 3.7 below, the skin friction values are about equal. Downstream of this region the experimental $C_f/2$ values increase rapidly as turbulence redevelops.

3.4 Reynolds stresses distributions

Figures 9 and 10 show intensity $\sqrt{\overline{u^2}}/U_\infty$ profiles for flows C and D from the fluctuation portion of the linearized hot-film and hot-wire signals. In flow C the maximum intensity remains at about 0.1 and is located in the range of $300 < \eta < 400$ up until $K > 3.6 \times 10^{-6}$ at about 181 inches, after which the normalized intensity decays and the maximum intensity location moves to a greater η value. The hump in the outer region of the upstream intensity profiles vanishes just downstream of the cessation of entrainment at about 165 inches. Between 165 inches and 181 inches the acceleration of the wall region flow alone is apparently sufficient to maintain the same level of turbulence production as upstream. In other words the entrainment of high momentum free-stream fluid performs no role.

Flow D exhibits the same behavior but the outer region hump does not completely vanish until about 143.8 inches. The maximum intensity is located in the range of $200 < \eta < 400$. Beginning at about 153.6 inches, where $C_f/2$ begins to drop rapidly, the value and η location of the maximum intensity decreases. After retransition to a low acceleration turbulent boundary layer begins, the maximum intensity remains at about 0.08 but the η location of the maximum increases. At 189.6 inches the intensity profile of a normal low acceleration turbulent boundary layer is emerging.

The split-film probe was used to determine $\overline{u^2}$, $\overline{v^2}$, and $-\overline{uv}$ for flow C. No split-film probe measurements were attempted for flow D. The mean velocity profiles showed very good agreement with those

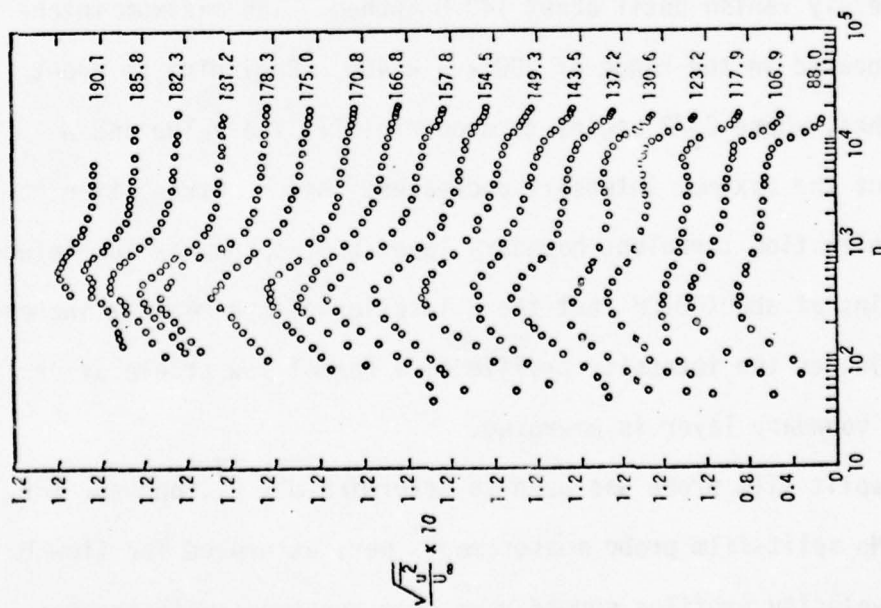


Figure 9. Streamwise intensity profiles for flow C. Note displaced scales. Station position in inches at right of each profile.

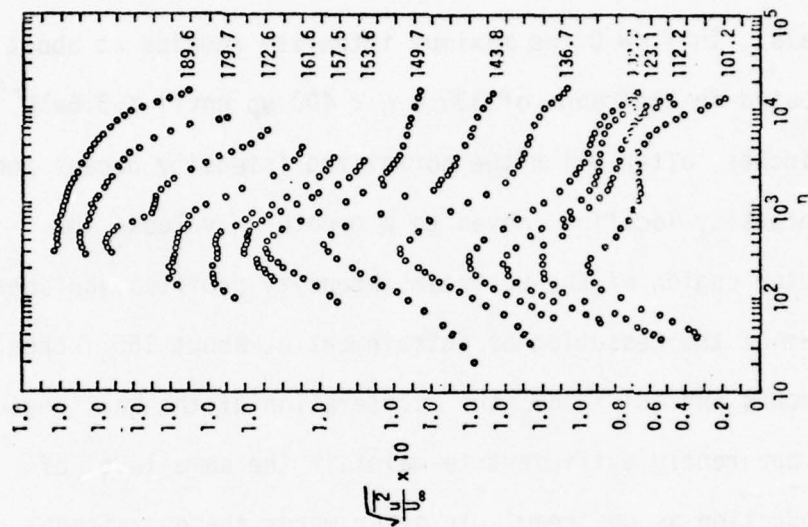


Figure 10. Streamwise intensity profiles for flow D. Note displaced scales. Station position in inches at right of each profile.

measured with a single film boundary layer probe. The deviation was within the uncertainty of the calibration except at locations 171.3, 178.8, and 187.6 inches. At these locations the mean velocities below $\eta = 10^3$ were as much as 47% high nearest the wall yet were less than 2% high at $\eta = 10^3$ and were less than 0.5% high at $\eta = 1300$ and beyond. At locations 101.7, 137.8, 149.6 and 162.4 inches, the mean velocity deviated from the single film probe by less than 3% from the wall to the freestream. The large deviation near the wall at higher freestream velocities may be due to the significantly greater velocity gradient effects which tend to cool the top film more than the bottom film.

The V component of velocity, when normalized against U_{eff} allowed comparison of the angle of flow ϕ with respect to the test wall since $\sin \phi = V/U_{eff}$. After accounting for the angle of the plane of the splits with the test wall, the angle of flow measured by the split-film probe at a point in the freestream was at worst within 1.4° of the flow angle at that point derived from the displacement thickness gradient and freestream velocity gradient. This difference is beyond 0.6° uncertainty in computing ϕ from the calibration equations plus the 0.2° uncertainty in ϕ due to approximation of the displacement thickness gradient. However, for 6 of the 8 profiles taken, the angles measured agree within that 0.6° uncertainty in ϕ .

The $\overline{u^2}$ fluctuations, as seen in figure 11, tend to show very poor agreement with those measured with the single film probe for $\eta < 10^3$. At $x = 137.8$ and 149.6 the discrepancy is apparent to

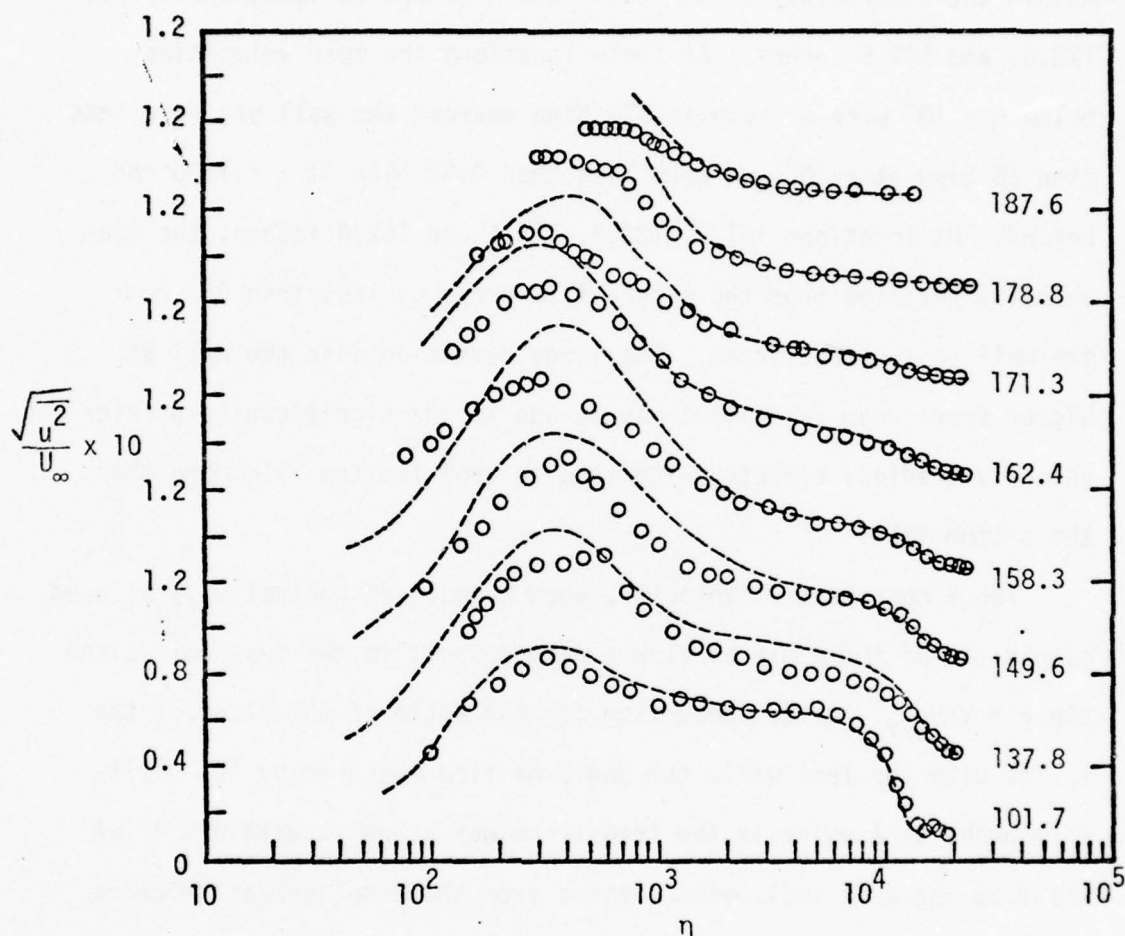


Figure 11. Streamwise fluctuation distributions from the split-film sensor for flow C. Profile location in inches at right of each profile. Dashed lines - normal hot-film results from figure 9 for nearby location. Note displaced ordinate scales.

$\eta = 10^4$. In all other cases the agreement is good from $\eta = 10^3$ to the freestream except at $x = 158.3$ where agreement is poor until η reaches 5000. The kinematic Reynolds shearing stress $-\overline{uv}$ also shares the $\eta = 10^3$ cutoff above which the data begin to seem reasonable. There is a rapid decrease in $-\overline{uv}$ as the flow accelerates as shown in figure 12. Also shown on this figure is the shearing stress profile for 190.1 inches generated from the momentum equation and U/U_∞ vs. η similarity. The outer region mean velocity profiles at 185.8 and 190.1 inches are similar well within 0.01 in U/U_∞ and K is constant. Thus the similarity assumptions are met for an asymptotic flow and the equation

$$\frac{-\overline{uv}}{U_\infty^2} = K \int_\eta^\infty (1 - f^2) d\eta - \frac{df}{d\eta} \quad (8)$$

describes the Reynolds shearing stress (Simpson and Wallace, 1975). The agreement must be considered good for $\eta > 2600$. Thus the results from the split-film for $-\overline{uv}$ are credible at least in locations where $\overline{u^2}$ is credible. The $\overline{v^2}$ quantities measured by the split-film are high in the viscous sublayer due to the high velocity gradient there. The data in the outer region, $\eta > 3000$, are more believable.

Many problems were encountered in using the split-film sensor. The calibration process was time-consuming and frequent checks were required to overcome anemometer drift. Anemometer drift at times caused the films to operate with different temperatures, thus producing thermal interference between films as well as introducing a slight velocity dependence on the yaw characteristics. The resistance

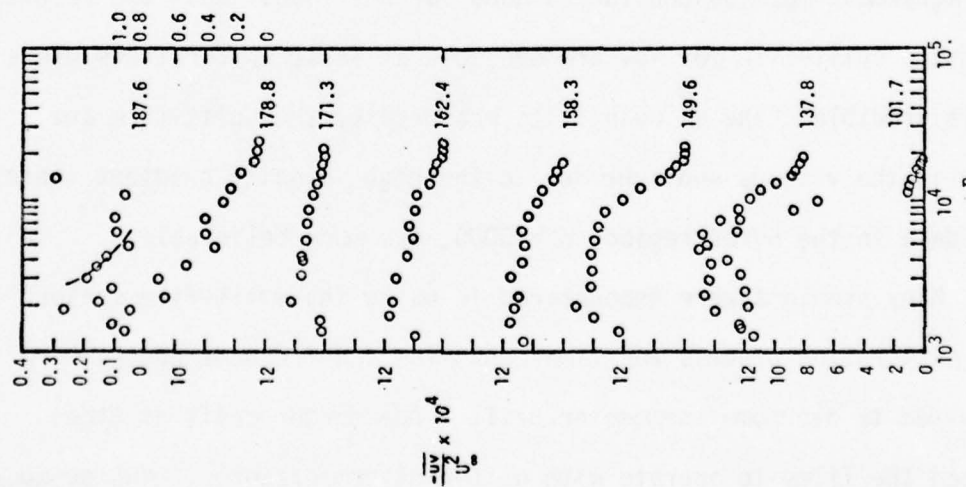


Figure 12. Reynolds shearing stress distributions from split-film sensor for flow C. Profile location in inches at right of each profile. Dashed line - mean velocity profile similarity result from eqn. (8). Note displaced ordinate scale.

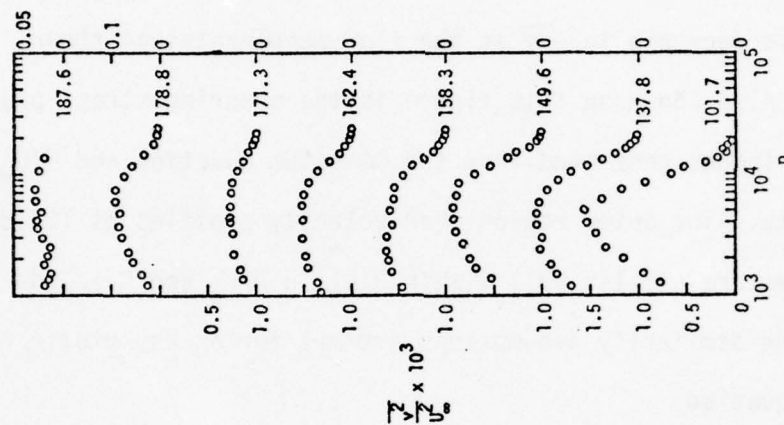


Figure 13. \bar{v}^2/U_0^2 distributions from the split-film sensor for flow C. Profile location in inches at right of each profile. Note displaced ordinate scales.

of the probe support structure sometimes changed when the probe was unplugged and then replaced in its support. Vortex shedding from the sensors produced high noise levels at increasing velocities. This noise introduced greater uncertainty in the fluctuation quantities. Velocity gradients near the wall produced unusually high V values at those points where V should be lowest. Several schemes were tried to correct for the influence of the high velocity gradient. Unfortunately, those corrections did not produce consistent results.

This experience with the split-film probe seems to be reasonably consistent with that of Sandborn (1976). He found $\sqrt{\overline{u'^2}}/U_\infty$ to be closely the same as that measured by a single hot wire parallel to the test wall. $-\overline{uv}$ values from split-film data appeared to be close to the estimated true shear stress profile away from the wall where velocity gradients are sufficiently small. On the other hand, Young (1976) found that the split-film probe consistently produced a low $\sqrt{\overline{u'^2}}$ by about 22% and a low $-\overline{uv}$ by about 26% in a two-dimensional channel flow. Thus, clearly the split-film results should be critically compared with results from other sensors for consistency.

3.5 Spectra measurements and dissipation estimates

The spectrum function $F(n)$ of $\overline{u'^2}$ was obtained throughout each boundary layer at several streamwise locations, where

$$\overline{u'^2} \int_0^\infty F(n) dn = \overline{u'^2} \quad (9)$$

and n is the frequency in Hz. Simpson and Wallace (1975) discovered that a portion of $F(n)$ varied like n^{-1} for locations in the region $n > 1000$ after the cessation of entrainment in flow B. They found that Tchen's high mean vorticity spectral model (Hinze, 1975) relating $F(n)$ to the turbulence dissipation ϵ by

$$\frac{\epsilon v}{U_\infty^4} = \frac{3}{2} \alpha [nF(n)] \left[\frac{\overline{u^2}}{U_\infty^2} \right] \frac{\partial f}{\partial n} \quad (10)$$

seemed to hold.

Their data indicate that α is about 0.77 for flow B. Data from flow B were reanalyzed using equation (10) above. Equation (21) of Simpson and Wallace should have contained $\overline{u^2}$. The spectral data of Laufer (1954) in the logarithmic region of a pipe flow indicate that $\alpha \approx 0.88$ while Klebanoff's (1955) flat plate turbulent boundary layer produced flat $nF(n)$ spectra with $\alpha \approx 0.80$. In both of these latter cases, ϵ was evaluated by the equilibrium relationship

$$\epsilon = -\overline{uv} \frac{\partial U}{\partial y} \quad (11)$$

that is applicable for the logarithmic velocity profile region (Rotta, 1962). Here we wish to examine the spectra obtained for flows C and D and the range of applicability of equation (10) using $\alpha = 0.8$.

Representative first moments of the spectra $nF(n)$ for flows C and D are presented in figures 14 through 23. The hot-film and hot-wire sensor response was down 5% at 15 KHz, and 25 KHz, respectively. The data were recorded on tape and processed on the fast Fourier analyzer with a bandwidth of 2 Hz and 50 seconds record times. The

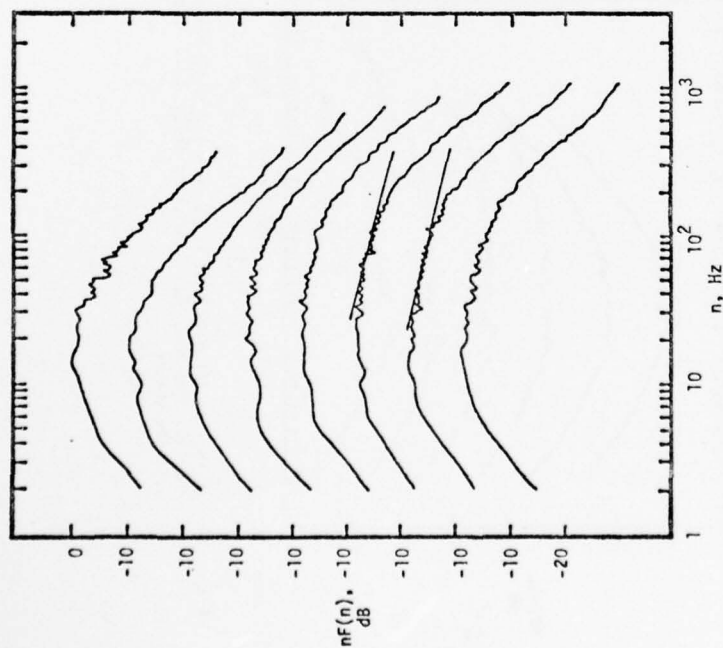


Figure 14. \bar{u}^2 spectra for flow C at 137.2 inches; from top to bottom $n = 54, 108, 350, 673, 1346, 2154, 4307, \text{ and } 8076$. Note displaced ordinate scales. Straight lines, $n^{-2/3}$ slope.

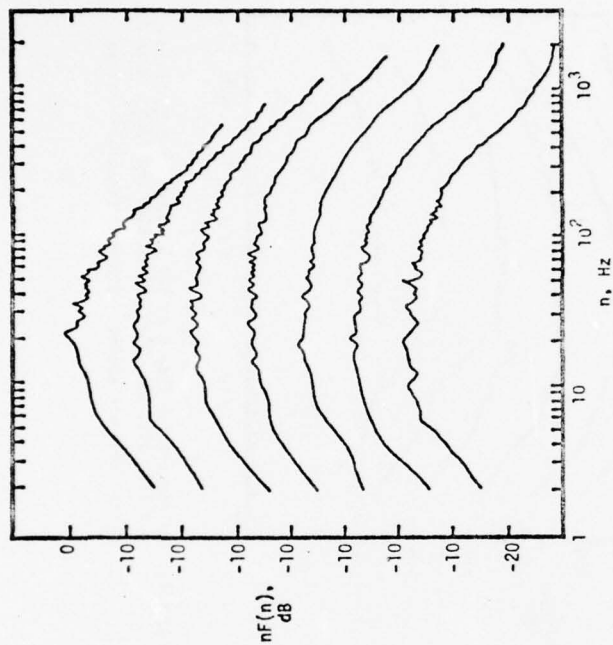


Figure 15. \bar{u}^2 spectra for flow C at 157.8 inches; top to bottom $n = 70, 454, 873, 1397, 2794, 5589, \text{ and } 8733$. Note displaced ordinate scales.

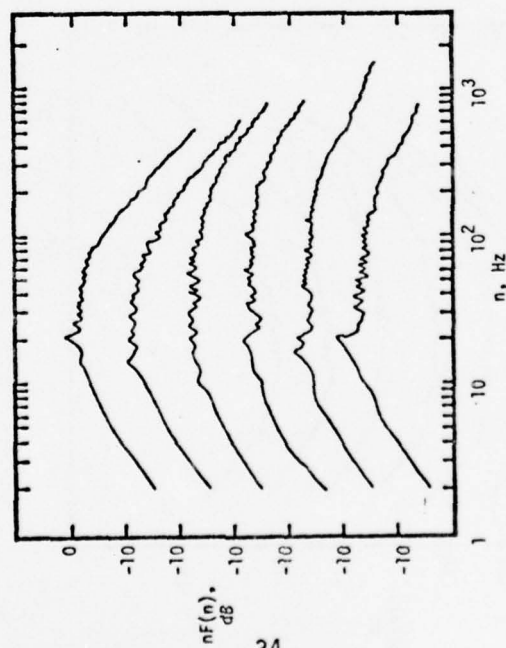


Figure 16. \bar{u}^2 spectra for flow C at 170.8 inches; top to bottom $n = 153, 306, 815, 1528, 3057, \text{ and } 8152$. Note displaced ordinate scales.

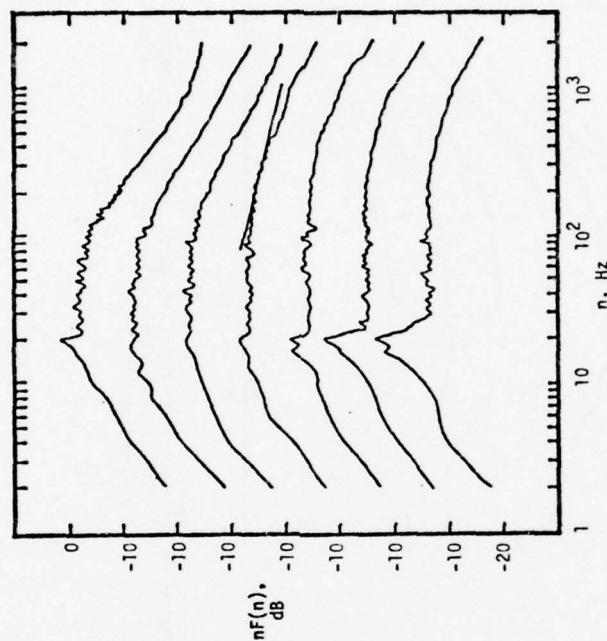


Figure 17. \bar{u}^2 spectra for flow C at 182.3 inches; top to bottom $n = 180, 541, 901, 1532, 2252, 3604 \text{ and } 7208$. Note displaced ordinate scales. Straight line, $n^{-2/3}$ slope.

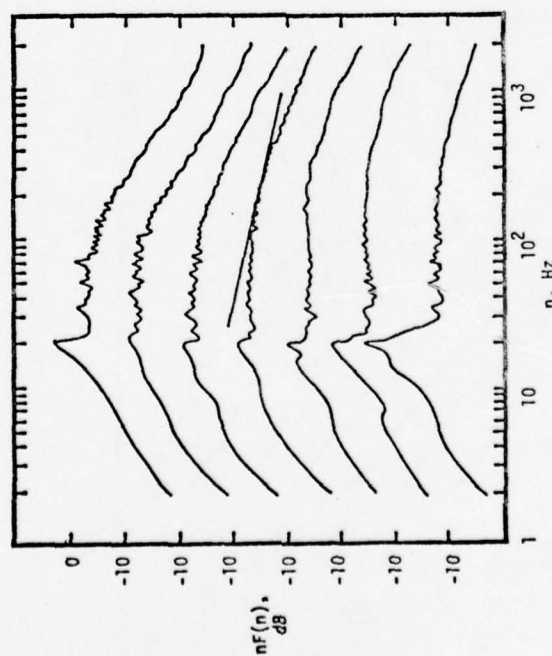


Figure 18. \bar{u}^2 spectra for flow C at 185.8 inches; top to bottom $n = 222, 444, 887, 1331, 1886, 2662, \text{ and } 7765$. Note displaced ordinate scales. Straight line, $n^{-2/3}$ slope.

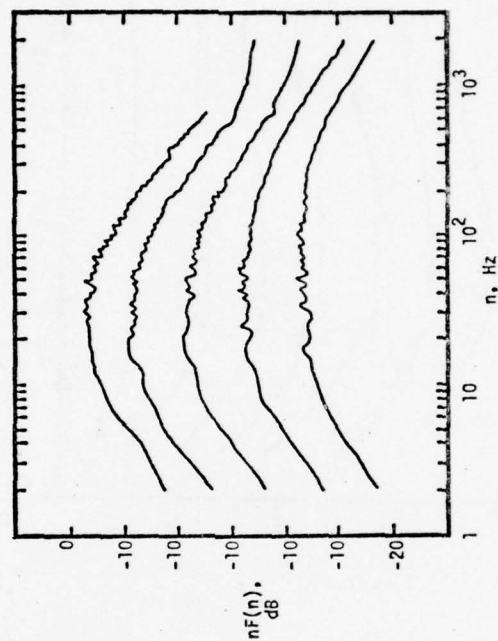


Figure 19. \bar{u}^2 spectra for flow D at 153.6 inches; from top to bottom $n = 153, 367, 673, 1131, \text{ and } 2201$. Note displaced ordinate scales.

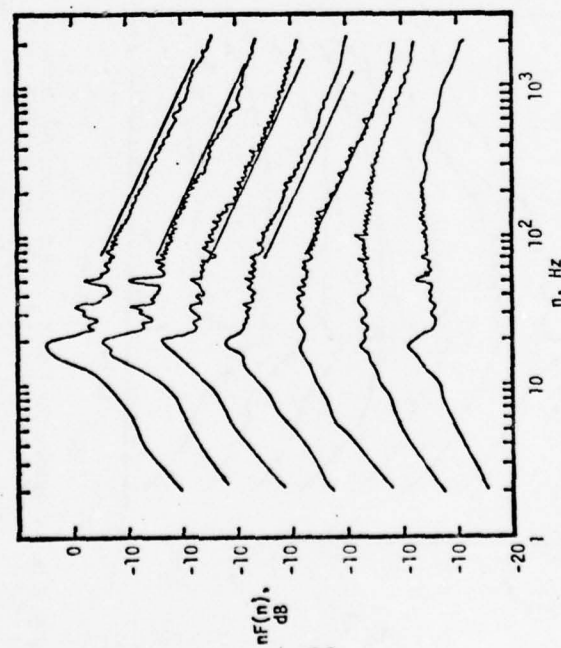


Figure 20. \bar{u}^2 spectra for flow D at 161.6 inches; from top to bottom $n = 135, 231, 328, 473, 834, 1919$ and 3848 . Note displaced ordinate scales. Straight lines, $n^{-1.3}$ slope.

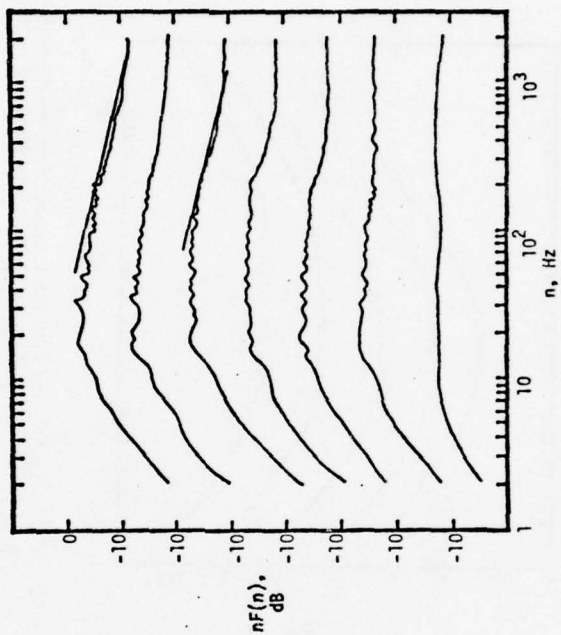


Figure 21. \bar{u}^2 spectra for flow D at 172.6 inches; from top to bottom $n = 333, 791, 1166, 1582, 2623, 4288$ and 6786 . Note displaced ordinate scales. Straight lines, $n^{-2/3}$ slope.

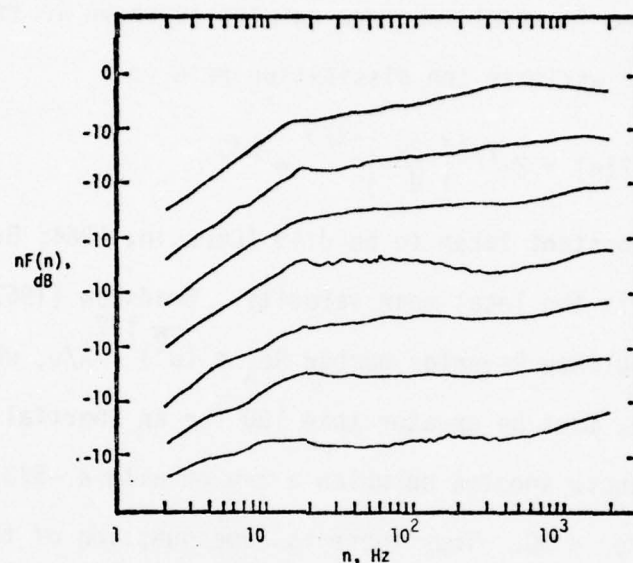


Figure 22. $\overline{u^2}$ spectra for flow D at 179.7 inches; from top to bottom $\eta = 283, 945, 1890, 3780, 5669, 7559, \text{ and } 9449$. Note displaced ordinate scales.

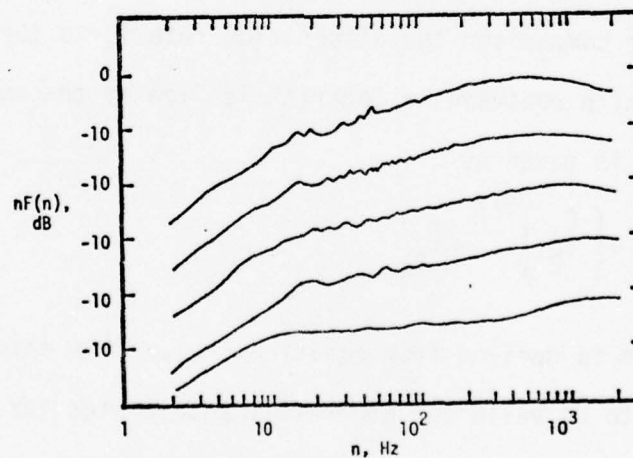


Figure 23. $\overline{u^2}$ spectra for flow D at 189.6 inches; from top to bottom $\eta = 305, 2034, 4069, 8138, \text{ and } 15259$. Note displaced ordinate scales.

2 KHz upper frequency limit on the analyzer was not a serious limitation except for the data at the downstream stations in flow D.

For several of the spectral distributions, a small range of the -5/3 law of the inertial subrange existed as shown in figure 14, so it was used to estimate the dissipation rate ϵ :

$$\overline{u^2} F(n) = K \epsilon^{2/3} \left(\frac{2\pi}{U} \right)^{-2/3} n^{-5/3} \quad (12)$$

Here K is a constant taken to be 0.49 (Corrsin, 1964; Bradshaw, 1967a) and U is the local mean velocity. Bradshaw (1967b) suggested that the turbulence Reynolds number $Re_\lambda = (\overline{u^2})^{1/2} \lambda / \nu$, where $\lambda^2 = 15 \nu \overline{u^2} / \epsilon$, must be greater than 100 for an inertial subrange to exist. For those spectra on which a region with a -5/3 slope was found, $35 < Re_\lambda < 80$. Thus there is some question of the validity of equation (12) even for these cases.

Figures 24 and 25 show the dissipation rate results for flows C and D. For comparison the dissipation rate for a turbulent boundary layer which possesses a logarithmic "law of the wall" mean velocity profile is given by

$$\frac{\epsilon \nu}{U_\infty^4} = \left(\frac{C_f}{2} \right)^{3/2} \frac{1}{0.4 \eta} \quad (13)$$

This equation is derived from equation (11). This result would also be expected to be valid for moderately accelerated turbulent boundary layers since a logarithmic mean velocity profile would still exist. At the upstream stations the dimensionless dissipation $\epsilon \nu / U_\infty^4$ is the same order of magnitude for each flow from equations (10),

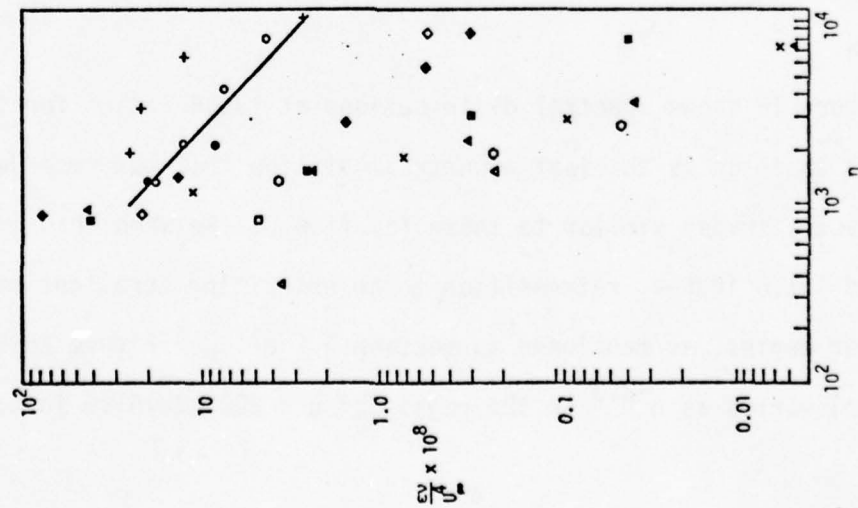


Figure 24. Dissipation results for flow C. Eqn. (12) results: + 106.9, \diamond 137.2, \square 157.8, \triangle 170.8, \times 178.3, \blacktriangle 182.3, (10) results: \bullet 137.2, \diamond 157.8, \square 170.8, \times 178.3, \blacktriangle 182.3, \circ 185.8. Solid line - eqn. (13) with $C_f \times 10^3 = 2.2$.

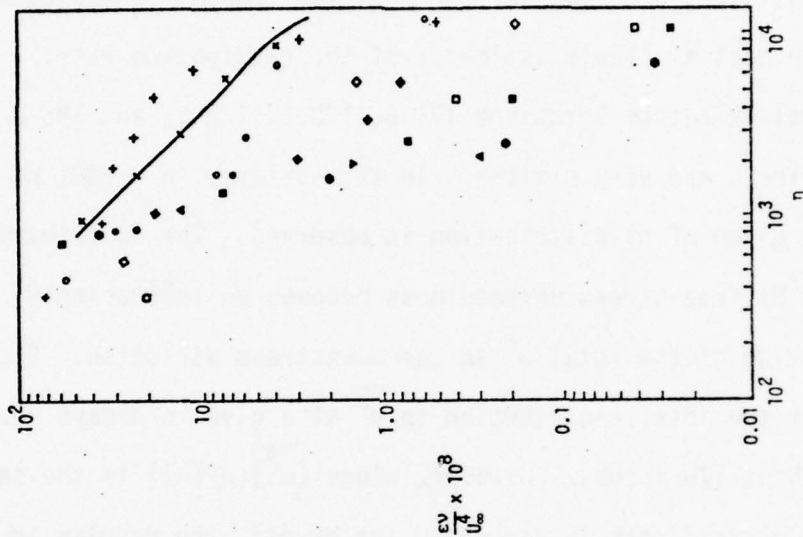


Figure 25. Dissipation results for flow D. Eqn. (12) results: + 101.2, \times 112.2, \circ 123.1, \diamond 132.2, \square 140.7, Eqn. (10) results: \bullet 123.1, \diamond 132.2, \square 140.7, \bullet 146.8, \triangle 153.6, \blacktriangledown 161.1. Solid line - eqn. (13) with $C_f/2 \times 10^3 = 2.9$.

(12), and (13). The results from equation (12) for each flow near the 100 inches location are closely the same. At 137.2 inches in flow C the results from equations (10) and (12) are reasonably close for a given η when $\alpha = 0.8$ is used. Since the $nF(n)$ spectra at downstream stations are flat for $\eta > 800$, the results from equation (10) are the best available estimates of the dissipation rate.

Spectral data from locations 170.8, 178.3, 182.3, and 185.8 inches of flow C are very similar. In the sublayer, $\eta < 800$, no flat region of a given $nF(n)$ distribution is observed. The contribution from the 20 Hz free-stream unsteadiness becomes an increasingly greater portion of the total $\overline{u^2}$ in the downstream direction. Figure 9 shows that the total contribution to $\overline{u^2}$ at a given η decays downstream of about 178 inches. However, since $(\overline{u^2})(nF(n))$ is the same whether the unsteadiness is accounted for or not, the results in figure 24 should be unaffected. For a given η in the outer region, $\epsilon\nu/U_\infty^4$ decreases two orders of magnitude from 137.2 inches to 170.8 inches. Thereafter the decrease is much slower. In the inner region, $\eta < 1000$, $\epsilon\nu/U_\infty^4$ remains about the same order of magnitude all along the flow.

Figure 19 shows spectral distributions at 135.6 inches for flow D. This location is the last downstream station that was recorded with spectra shapes similar to those for flow C. Between this location and 161.6 inches, retransition to an entraining turbulent boundary layer begins, as mentioned in section 3.7 below. Figure 20 shows that $F(n)$ varies as $n^{-2.3}$ in the region of $\eta < 800$ at 161.6 inches,

where the intermittency is about 0.01. In the outer region at this location flat $nF(n)$ spectra are found. Note the relative importance of the 20 Hz unsteadiness. Downstream where the intermittency is progressively increasing, the spectral distributions are flatter. At 179.7 and 189.7 inches the peaks shift progressively toward 1 KHz as the low accelerated turbulent boundary layer redevelops. Notice that 20 Hz unsteadiness does not dominate the near wall spectra.

The dissipation results for flow D from equations (10) and (12) are in reasonably good agreement at 123.1 inches and in fair agreement at 132.2 and 140.7 inches. Between 132.2 and 161.1 inches the results from equation (10) are considered the best available estimates of the dissipation rate. For a given η in the outer region, $\epsilon v/U_\infty^4$ decreases two orders of magnitude from 123.1 to 161.1 inches, as was observed for flow C. As for flow C, $\epsilon v/U_\infty^4$ remains about the same order of magnitude in the inner region along this length of flow. Certainly the spectral behavior downstream of retransition needs further research.

3.6 Wall bursting frequencies and spanwise structure

The more or less periodic lift off or bursting process in the viscous sublayer has become accepted as the sequence of events that create the Reynolds shearing stress near the wall (Wallace et al., 1972; Nychas et al., 1973; Willmarth, 1975). On a short-time basis the velocity fluctuations in the sublayer produced by the bursting process vary across the sublayer in the spanwise direction. The data of Gupta et al. (1971) indicate that the short-record-time

normalized cross-correlation of fluctuations $\hat{sR}_{uu}(z, T_s)$ could be represented by a spanwise periodic function. Their results indicate that the short-record-time T_s over which the cross-correlation is averaged must be less than about 20 bursting periods in order for the periodic spanwise structure to be detectable. Simpson and Wallace (1975) measured the average frequency of bursting and the long-time spanwise cross-correlation of fluctuations for two sink-flow type strongly accelerated turbulent boundary layers, flows A and B. Here the results from flows C and D are presented.

Strickland and Simpson (1973, 1975) assumed that the short-time autocorrelation time scale from a flush wall hot-film sensor and the bursting period were equal. Histograms of the frequency characterized by the time to the first peak on these autocorrelations were constructed and the corresponding frequency of the peak of each histogram was taken as the characteristic frequency. The histograms appeared to have a log-normal probability distribution, so this peak frequency was also the median frequency. They also proved a one to one correspondence between this characteristic frequency and the peak of the first moment of the wall shearing stress spectra $nF(n)$. Also, examination of spectral data from zero pressure gradient boundary layers produced bursting frequencies in agreement with those previously reported. More recently, Simpson (1976) used a pattern recognition algorithm to determine the average bursting frequency from flush surface hot-film signals produced in the Max-Planck-Institut für Strömungsforschung oil channel. This average bursting

frequency closely agreed with the peak of the $nF(n)$ spectral distribution of these signals.

As was done for flows A and B, the peak of each $nF(n)$ curve for flows C and D was deduced as the bursting frequency for a given wall spectral distribution. The results are given in table 3. As it is clear from figures 26 and 27, it is difficult to select a precise single frequency at which $nF(n)$ is a maximum for a given distribution. Consequently, a range over which the peak frequency definitely occurs is also presented in table 3.

Two types of non-dimensionalizing parameters have been used in previous bursting frequency studies, inner variables and outer variables. Inner variables are the shear velocity U_τ for the velocity scale and v/U_τ for the length scale. This scaling does not correlate other available bursting data. The bulk of available bursting frequency results for turbulent boundary layers correlate using the outer flow velocity and length scales, U_∞ and δ . For zero pressure gradient boundary layers $U_\infty/\delta n_b$ is about 5 (Rao et al., 1971) and varies between 11.7 and 8.35 for the separating turbulent boundary layer of Simpson et al. (1974). It should be noted that this large eddy outer variables scaling continued even after the boundary layer separated.

For flow A presented by Simpson and Wallace (1975), $U_\infty/\delta n_b$ started at about 5 at 89.2 inches, decreased to about 3.5 at about 139 inches or the location of minimum H , and then monotonically increased to a value above 50 at the last measurement station. The

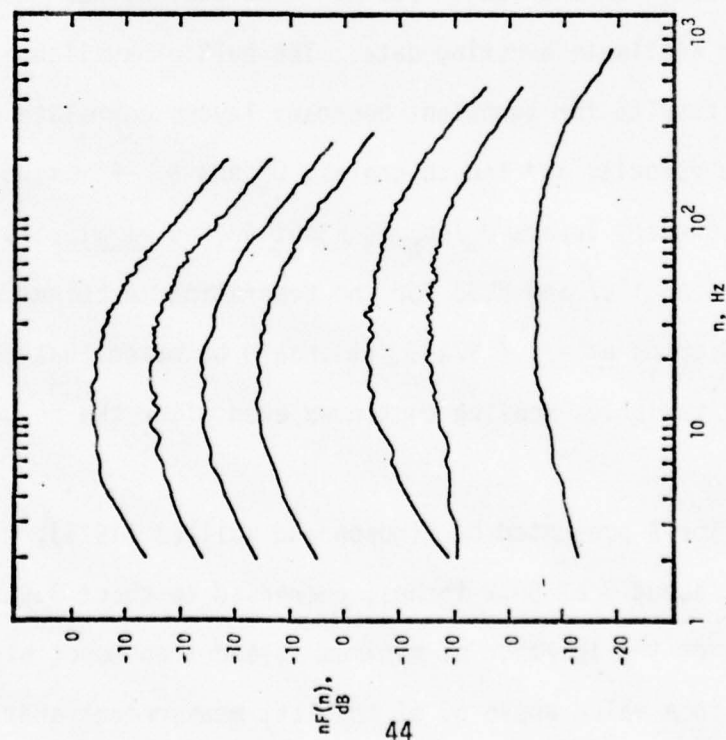


Figure 26. Typical flush-wall hot-film spectra, flow C. Station location from top to bottom: 105.0, 122.0, 135.5, 156.3, 171.8, 184.2, and 186.2. Record times 100 sec. Note displaced ordinate scale.

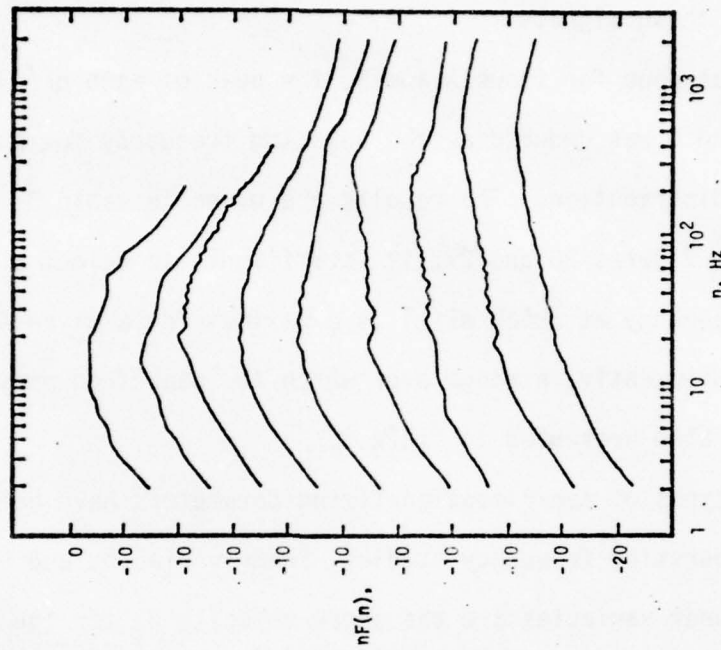


Figure 27. Typical flush-wall hot-film spectra, flow D. Station location from top to bottom: 122.0, 135.5, 158.3, 171.8, 175.2, 177.4, 182.0, 184.2, and 186.2. Record times 50 sec. Note displaced ordinate scale.

bursting frequency n_b apparently reached about a constant value after the asymptotic condition was achieved, so an increasing $U_\infty/\delta n_b$ reflects the fact that U_∞ increases and δ decreases faster than n_b increases. For flow B $U_\infty/\delta n_b$ remained nearly constant at about $3(\pm 1)$ until the location of a minimum in H , downstream of which it also increased monotonically to a value of about 90 at the last measurement station. The bursting frequency n_b was virtually constant all along flow B. The outer variables parameter $U_\infty/\delta n_b$ was no better a correlation parameter for these data.

The results for flow C indicate that the bursting frequency increased up to about 165.3 inches or where H was about a minimum and where entrainment ceased. The plateau on the $nF(n)$ spectral distributions existed over an increasingly wider frequency range at downstream locations. The low frequency end of the plateau remained at about 25 Hz. The results from these three flows indicate that they are non-equilibrium flows at least up until the cessation of entrainment. Thus no equilibrium non-dimensional parameter such as $U_\infty/\delta n_b$ should have a constant value upstream of the minimum in H . Downstream of the minimum H location there was no entrainment, so the large eddy structure and the intermittent turbulent/non-turbulent outer region flow were not creating new bulges. Thus the bursting frequency and the frequency of passage of the intermittent bulges (see section 3.7 below) were constant in this downstream region.

For flow D the bursting frequency increased until near the location where H was a minimum, after which it remained constant until

Flow C			Flow D		
Station (inches)	Peak frequency, n_b , Hz	Range of peak, Hz	Station (inches)	Peak frequency, n_b , Hz	Range of peak, Hz
90.2	15	13-18	105.0	12	10-15
105.0	12	10-15	110.4	15	10-20
110.4	13	10-20	122.0	15	10-20
117.3	15	10-20	129.9	19	15-25
122.0	16	13-20	133.5	18	15-25
129.9	16	11-20	135.5	18	15-20
131.6	16	11-20	139.7	20	15-25
135.5	20	14-22	147.6	20	15-25
138.6	16	10-20	158.3	25	20-30
139.7	16	10-20	171.8	20	15-30
147.6	20	15-30	175.2	25	20-40
156.3	20	15-20	177.4	300	250-350
158.3	20	15-25	182.0	200	150-250
165.3	25	20-30	184.2	500	400-700
171.8	25	20-30	186.2	500	400-700
175.2	25	15-35	189.6	500	400-700
177.4	26	20-30			
182.0	26	20-30			
184.2	--	20-45			
186.2	--	20-100			

Table 3. Peak frequencies of $nF(n)$ spectral distributions from flush surface hot-film sensors.

Station (inches)	Z_{\max}, mm	λ_{Z1}^+	Z_{\min}, mm	λ_{Z2}^+	L_Z, mm	L_Z^+	$\frac{1}{2t_{\min-\max}}, \text{Hz}$
117.3	7.62	6.7	5.59	99	4.88	43.4	19
138.6	---	---	7.11	151	4.46	47.3	16
156.3	10.16	135	5.33	142	3.23	43.0	--
165.3	9.40	157	3.56	119	1.42	23.8	--
182.0	8.38	302	3.86	278	1.79	64.5	28
126.3	14.48	179	5.33	132	2.70	33.3	22
138.6	9.40	160	4.83	164	2.60	44.3	21
156.3	8.38	274	2.41	158	1.11	36.4	22
165.3	7.87	332	3.30	279	3.61	152.5	--
182.0	---	---	21.6	3480	12.50	1007	--

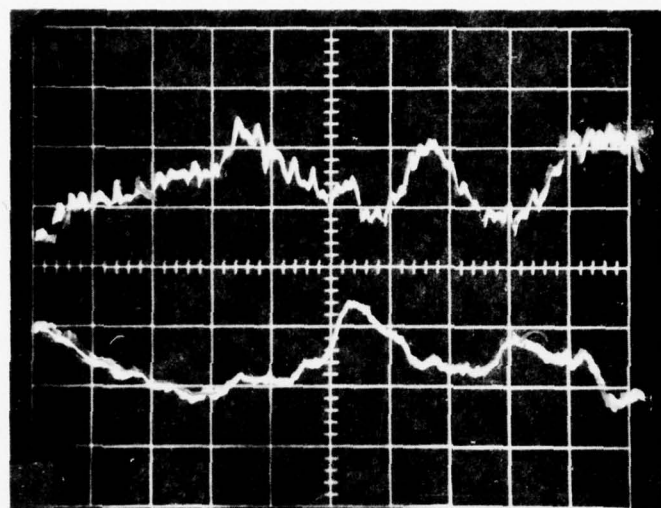
Table 4. Experimental results from the wall spanwise spatial cross-correlatives. First five entries, flow C; second five, flow D.

the beginning of retransition to a low accelerated turbulent boundary layer. As discussed in section 3.7 below, high velocity pulses are first detected at about 165.3 inches. Figure 27 shows that the wall sensor spectra are not appreciably affected until about 175.2 inches.

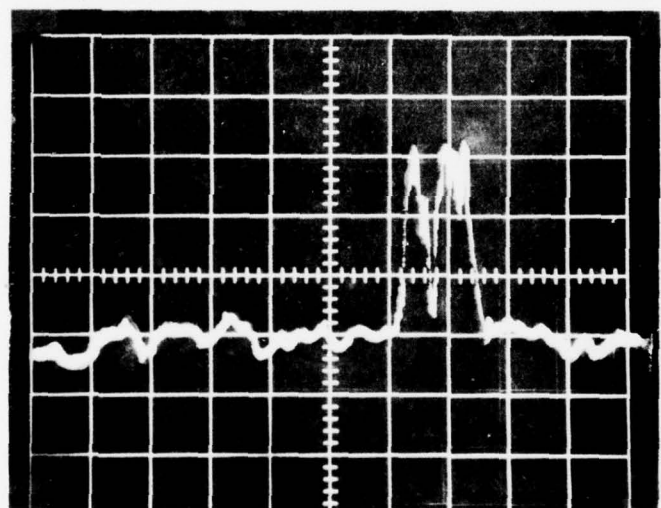
Figure 28(c) shows a typical signal trace for this location. Between 175.2 and 182.0 inches, a distinct local peak is observed in the spectra at frequencies an order of magnitude higher than observed upstream. This indicates that the high frequency oscillations that are contained in the higher velocity pulses are increasingly important. Downstream of 184.2 inches the laminar-like low velocity regions such as seen in figure 31 for 182.0 inches were no longer observed on signal traces. Thus the flow at the wall was always turbulent. Peak frequencies are observed in figure 27 to occur at an even higher frequency of about 500 Hz.

Several researchers have proposed that during the bursting process a hairpin or horseshoe vortex with trailing legs is formed (Willmarth, 1975). With this model, the counter-rotating trailing legs would produce fluctuations in the sublayer that are periodic in the spanwise or z direction on a short-time basis. Simpson (1976) noted that this model suggests motions too coherent to be consistent with experimental observations.

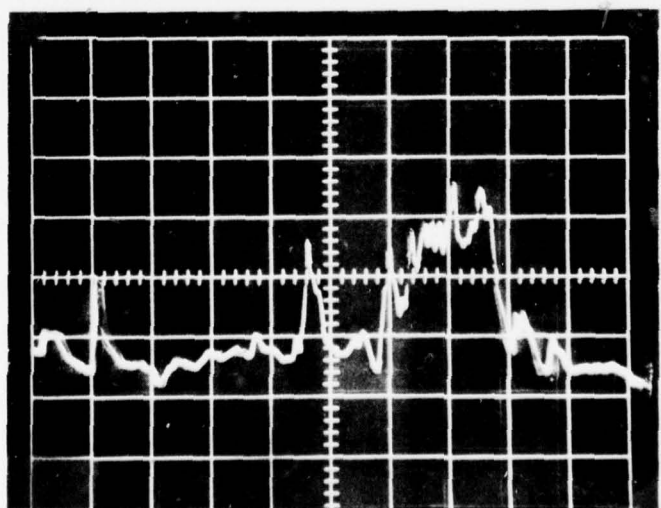
He alternatively proposed that "fingers" of high velocity fluid come from the outer region at a velocity much higher than sublayer mean velocities toward the wall and displace the low velocity fluid



(a)



(b)



(c)

Figure 28. Flush surface hot-film signals for flow D. Top photo: 138.6 inches, $\Delta Z = 4.83$ mm; top trace-movable sensor, 500 Hz low pass filtered, lower trace-fixed sensor, 1 kHz low pass filtered; 10 msec/div. Middle photo: 171.5 inches, 20 msec/div. Bottom photo: 175.0 inches, 5 msec/div.

t →

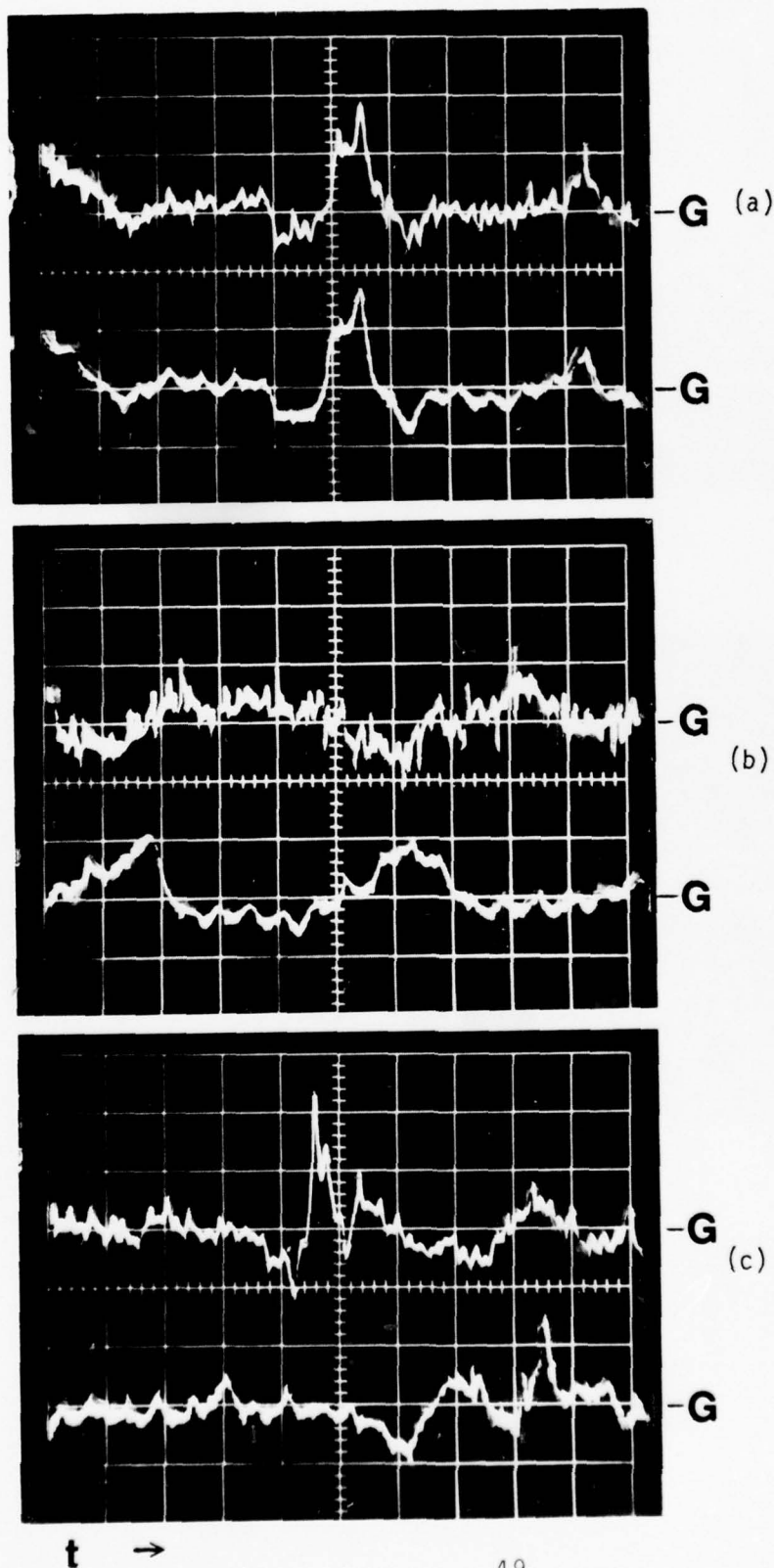


Figure 29. Flush surface hot-film signals from two-sensor unit at 156.3 inches for flow D. Top trace of each photo - moveable sensor; bottom trace - fixed sensor. From top to bottom $Z = 0$ mm, 2.29 mm, and 8.38 mm. Abscissa - 10 msec/div. Low pass filter: 500 Hz moveable sensor; 2 kHz - fixed sensor. G denotes mean signal level.

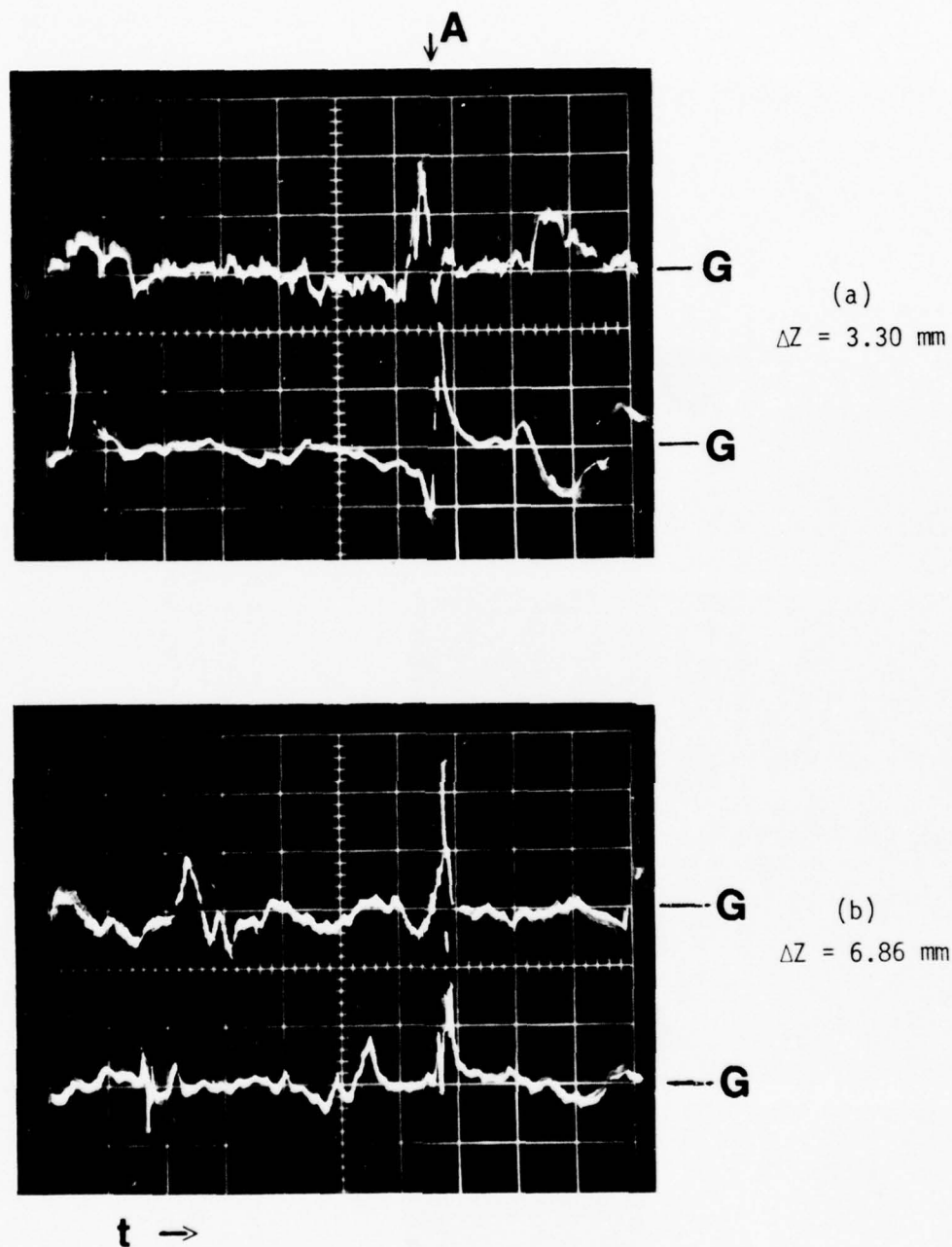


Figure 30. Flush surface hot-film signals from two-sensor unit at 165.3 inches for flow D. Top trace of each photo - moveable sensor; bottom trace - fixed sensor. Abscissa - 10 msec/div. low pass filtered at 2 kHz. G denotes mean signal level.

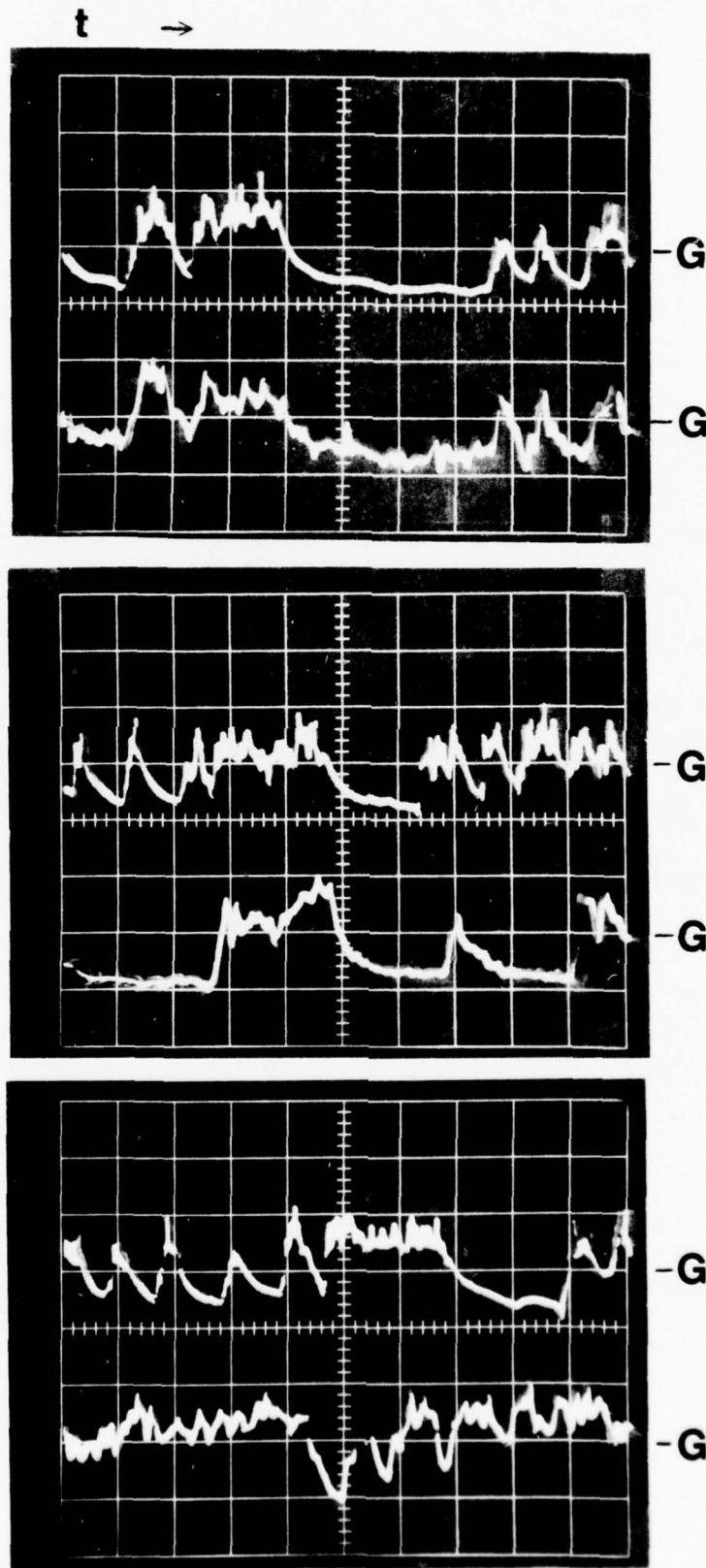


Figure 31. Flush surface hot-film signals from two-sensor unit at 182.0 inches for flow D. Top trace of each photo - fixed sensor; bottom trace - moveable sensor. From top to bottom $\Delta Z = 0$ mm, 8.13 mm, and 19.56 mm. Abscissa - 5 msec/div. Low pass filter: 1 kHz - moveable sensor; 5 kHz - fixed sensor. G denotes mean signal level.

to each side. These fingers of high velocity fluid were found for the MPI oil channel flow to be no less than $\Delta z^+ \approx 11$ nor greater than about $\Delta z^+ \approx 44$ in size and are spaced spanwise across the flow at average distances of about $\lambda_z^+ \approx 100$. There are curved fronts on these higher velocity fluid fingers so that the low velocity fluid just downstream at that instant must move aside to satisfy continuity requirements. Thus low velocity fluid trapped between two high velocity fluid fingers must move outward from the wall.

After the low velocity fluid has been "ejected" away from the wall, the two adjacent higher velocity fluid fingers coalesce. Since this fluid now occupies the wall region it progressively gives up its momentum until new high velocity fingers from the outer region force this fluid away from the wall and the process is repeated downstream. The spanwise locations of these high velocity fingers vary randomly for successive burst occurrences.

An interesting point is that these high velocity fingers must be formed so that the low velocity fluid can be ejected between them. Otherwise a blanket of higher velocity fluid would trap the low velocity fluid beneath. Stability considerations then require regions of high velocity fluid separated by low velocity ejections. The bulk of available experimental results for low pressure gradient flows show that the most preferred spacing of these higher velocity regions is $\lambda_z^+ \approx 100$. It appears unlikely that streamwise vortices that rotate more than one revolution are produced by the ejection process.

Some characteristics of the spanwise sublayer spatial structure for flows C and D were determined using the two sensor wall unit

described by Simpson and Wallace (1975). The unit was located spanwise across the tunnel with the direction of travel of the slider plate perpendicular to the streamwise flow direction. The signals from the two sensors were time-delay cross-correlated using the SAICOR model 41 correlator, with the record time for a given z -spacing time-delayed correlation being 65.5 seconds. For zero time delay, normalized spanwise cross-correlations $\hat{sR}_{\tau\tau}(z)$ such as shown in figures 32 and 34 result. Three characteristic lengths were deduced, the distance to the first correlation maximum z_{\max} , the distance to the first correlation minimum z_{\min} , and the integral length scale

$$L_z = 2 \int_0^{z_i} \hat{sR}(z) dz \quad (14)$$

The limit of integration z_i was taken as the largest available location for which data were available.

Figure 32 and table 4 indicate that for flow C the integral length scale progressively decreased until 165.3 inches and slightly increased thereafter. The parameters z_{\min} and z_{\max} are relatively easy to interpret, within 10% for the former and 20% for the latter. The results of Gupta et al. (1971) and Simpson (1975) indicate that z_{\min} is a somewhat more reliable spatial parameter than z_{\max} . These two parameters are normalized by the wall length scale ν/U_τ to produce the quantities

$$\lambda_{z1}^+ = \frac{U_\tau z_{\max}}{\nu} \quad \text{and} \quad \lambda_{z2}^+ = \frac{2U_\tau z_{\min}}{\nu} \quad (15)$$

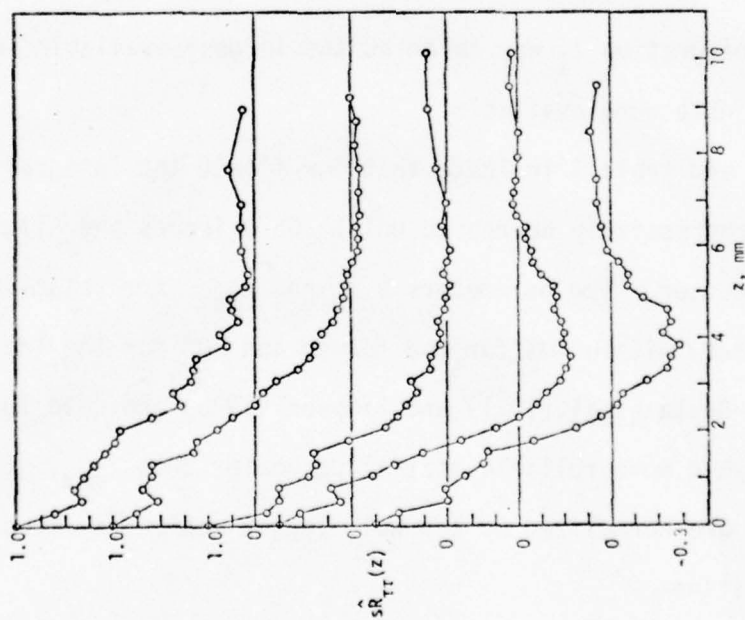


Figure 32. Normalized long time-averaged spanwise correlation $s\hat{R}_{tt}(z)$ results at the wall for flow C. Station locations from top to bottom: 117.3, 138.6, 156.3, 165.3, and 182.0 inches. Note displaced ordinate scales.

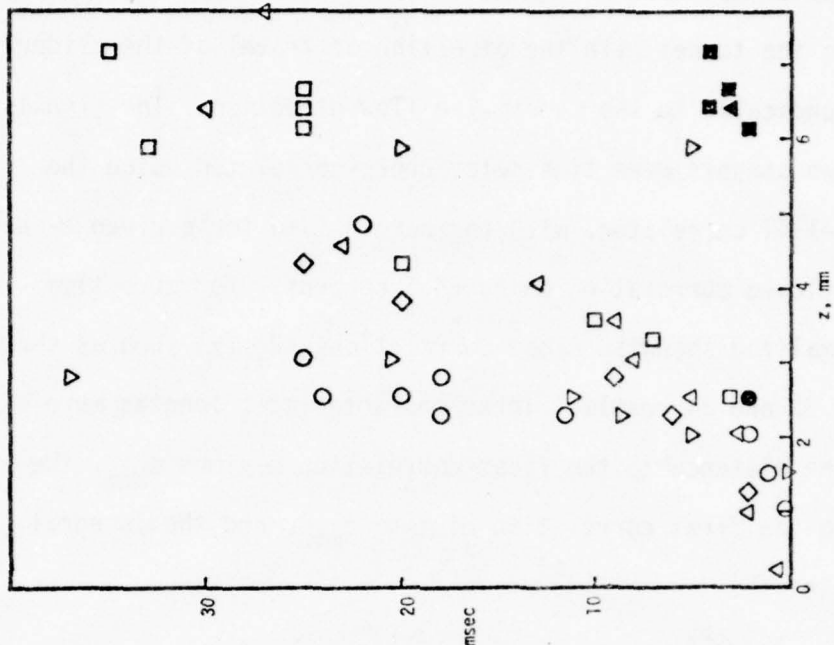


Figure 33. Observed minima and maxima from $\hat{R}_{tt}(z,t)$ data, flow C. Open symbols - maxima; solid symbols - minima: Δ , 117.3; \square , 138.6; \diamond , 156.3; \circ , 165.3; ∇ , 182.0.

which have the value of about 100 for zero pressure gradient boundary layers. Only at 182.0 inches does λ_{zz}^+ increase appreciably from this value. At the two downstream locations, $\hat{sR}_{\tau\tau}(z)$ behaves more like the low Reynolds number cross-correlation computed by Simpson (1976). He used the Gupta et al. spanwise spacing probability distribution to compute $\hat{sR}_{\tau\tau}(z)$ when no large eddy outer region structures were present, i.e. $L_z/z_{\min} \rightarrow 0$.

Figure 34 and table 4 indicate the same type of behavior for flow D up to 156.3 inches with $L_z/z_{\min} \approx 1/2$. Figures 28(a) and 29 shows typical simultaneous signal traces for the two sensors. For the two downstream stations, the signals contained high velocity pulses intermittently as shown in figures 30 and 31 and as discussed in section 3.7 below. The length scale ratio L_z/z_{\min} was about 1.1 at 165.3 inches and 0.579 at 182 inches. The parameter λ_{zz}^+ is significantly larger than 100 at these two stations.

Several different models were examined in an attempt to correlate these λ_{zz}^+ results. As attempted for flows A and B, λ_{zz}^+ was compared with the data of Schraub and Kline(1965) when presented versus K. Just as Schraub and Kline found, λ_{zz}^+ is of the order of 300 for $K \approx 3 \times 10^{-6}$. However, for lower K values λ_{zz}^+ varied rather randomly between 100 to 164. In flow D λ_{zz}^+ remained only at about 158 at 156.3 inches even after the flow had been subjected to a K of 3.85×10^{-6} and K was decreasing. After retransition to a low accelerated turbulent boundary layer had begun λ_{zz}^+ was very large even though K was of the order of 10^{-6} . It does not appear that λ_{zz}^+

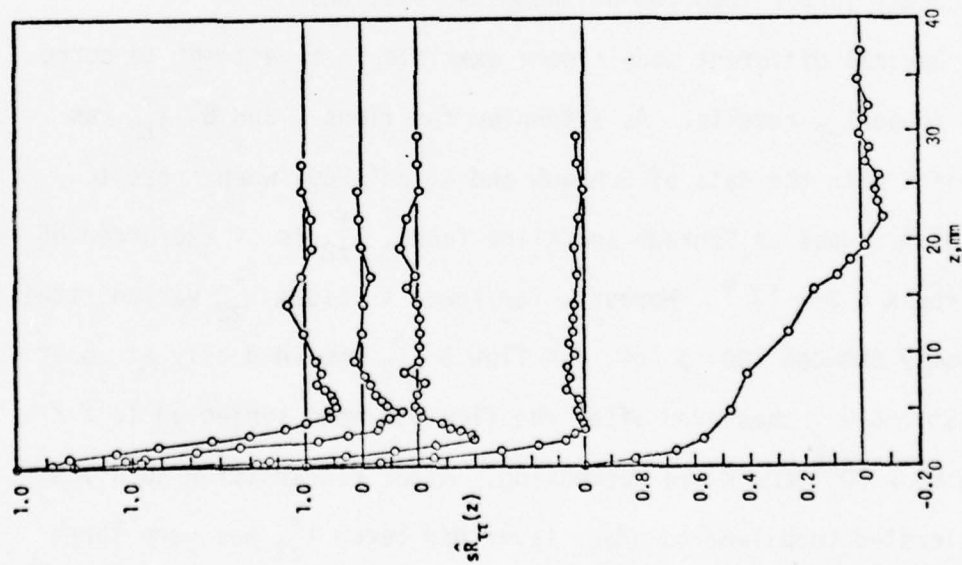


Figure 34. Normalized long time-averaged spanwise correlation $\hat{s}R_{tt}(z)$ results at the wall for flow D. Station locations from top to bottom: 126.3, 138.6, 156.3, 165.3, and 182.0 inches. Note displaced ordinate scales.

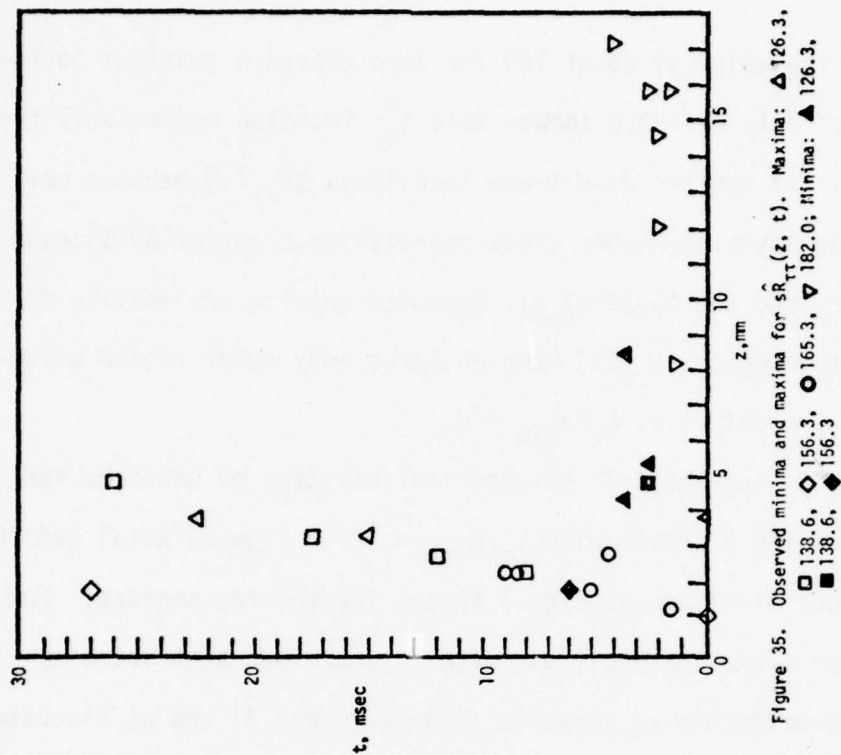


Figure 35. Observed minima and maxima for $\hat{s}R_{tt}(z, t)$. Maxima: Δ 126.3, \square 138.6, \diamond 156.3, \circ 165.3, ∇ 182.0; Minima: \blacktriangle 126.3, \blacksquare 138.6, \blacklozenge 156.3

is solely a function of K . After retransition began, the flow character with high velocity pulses is entirely different than that found upstream.

Simpson et al. (1974) found that for adverse pressure gradient turbulent boundary layers, the maximum turbulent shearing stress should be used in the velocity scale in order to produce $(-\overline{uv}_{\max})^{1/2} z_{\max}/\nu$ values of about 100. This model was not successful for flows A and B (Simpson and Wallace). Unfortunately the split-film results for $-\overline{uv}$ presented in section 3.4 are not reliable in the wall region where it is a maximum. Since $-\overline{uv}/U_{\infty}^2$ decreases along a strongly accelerated flow, $(-\overline{uv}_{\max})^{1/2} z_{\max}/\nu$ would also decrease. This parameter would fall well below 100 since $(-\overline{uv}_{\max})/\tau_w$ would be below 1/4 at say, 156.3 inches. Another correlation parameter, $(KU_{\infty}^2/\nu n_b)(C_f/2)^{-1/2}$, used by Simpson et al. was also not successful in correlating these data.

It appears that the λ_z^+ spacing lags behind local conditions. In other words, the spatial parameters z_{\max} and z_{\min} remain large due to upstream conditions in these non-equilibrium flows. For example, at 182.0 inches in flow C, U_t/ν is more than twice that at 165.3 inches but z_{\min} and z_{\max} are only slightly different. In retrospect, there is no reason to expect flows C and D to possess equilibrium characteristics.

Figures 33 and 35 show the local maxima and minima from the time-delayed cross-correlations for a given z spacing which were clearly distinguishable from noise. The wavelike nature of the

viscous sublayer behavior is illustrated by the fact that the maximum correlation at a given z spacing is time-delayed. The bursting frequency results given in table 3 above are somewhat crudely supported by the frequency corresponding to twice the time delay between the first minima and the first maxima, as given in table 4. In other words, if there is a repetitive wave-like nature of the sublayer flow in both z and t , the time-averaged characteristic bursting frequency should be approximately the same at all z sensor spacings.

For flow D figures 29(b) and 30(a) show that for the z spacings of sensors at which the spanwise cross-correlations were a minimum, the two signals were strongly out of phase. At time A in the latter oscilloscope photograph a short period of high velocity fluid passed over the moveable sensor. At the same time lower velocity fluid passed over the fixed sensor. A short time later, of the order of 3 msec, high velocity fluid passed over the fixed sensor while low velocity fluid passed over the moveable sensor. About 15 msec later the two traces again appear to be strongly out of phase. These data are consistent with the observations of Simpson (1976) regarding fingers of high velocity fluid as mentioned above.

3.7 Intermittency measurements

The intermittency factor γ , or the fraction of time that the flow is turbulent at a given spatial location, was determined for flow C using smoke in the boundary layer as the marker of turbulent fluid and scattered light from this smoke at a given location as the detected signal, using the optical apparatus described in section 2

above. Due to the large-scale mixing in the turbulent region the smoke is rapidly diffused while smoke is carried across the turbulent/non-turbulent interface by the much slower process of molecular diffusion. Thus, the smoke was assumed to be effectively confined to the turbulent regions of the flow. Fiedler and Head (1966) verified that values obtained by this method agree with those obtained by analysis of hot-wire signals.

The signal passed from the photomultiplier tube through a trigger circuit which produced positive rectangular pulses when the input was above a preset discrimination level. The discrimination level was set at approximately 10% of the peak PM tube sign amplitude. The counter-timer determined the fraction of time the positive pulses were present, which is the intermittency. Due to the steep slope of the PM output pulses, γ was not very sensitive to slightly different discriminator levels. Preliminary data taken in a zero pressure gradient flow were found to be in close agreement with the data of Klebanoff (1954).

The intermittency factor γ of this turbulent/non-turbulent interface has been previously found to be well represented by the integral of the normal distribution curve

$$\gamma = \frac{1}{\sqrt{2\pi} \sigma} \int_{\xi}^{\infty} \exp \left[-\frac{1}{2} \frac{\xi^2}{\sigma^2} \right] d\xi \quad (16)$$

where $\xi = y - \bar{Y}$, \bar{Y} is the mean distance from the wall to the interface where $\gamma = 0.5$, and σ is the deviation from the mean. If this interface is viewed as a wavy pattern moving approximately at the

free-stream velocity, then σ characterizes the amplitude of this pattern. γ was in good agreement with equation (16) for flow C. Table 5 presents the characterizing parameters which describe these intermittency distributions.

The results of Fiedler and Head (1966) showed that the parameters \bar{Y}/δ^* and σ/δ^* are strongly dependent on the shape factor H for values of H less than about 2. This dependence is quite strong as the lower limiting value of H is approached. The minimum H found for flow C was about 1.26 at about 165 inches. Upstream of the minimum in H for flow C, at 130.6 and 149.3 inches, values of these parameters were well within the scatter of the Fiedler and Head results for their "normally developing" boundary layers. As pointed out in section 3.2 above, no entrainment of non-turbulent fluid takes place after the minimum H value occurs so it is not unexpected that \bar{Y}/δ^* and σ/δ^* downstream do not follow the results of Fiedler and Head.

The celerity and mean velocity profile measurements for flows A and B reveal that when there is no entrainment, the entire intermittent region is moving with the free-stream velocity. This means that there cannot be any relative streamwise motion of the intermittent region nor any engulfment of non-turbulent fluid by turbulent bulges. $U_\infty(\bar{Y} - \delta^*)$ and $U_\infty\sigma$ remain approximately constant downstream. As for flows A and B, the intermittent region plays no role in the momentum transport after entrainment.

Measurements of the frequency with which turbulent bulges pass a fixed point were made by counting the number of pulses per unit

Station (inches)	$\bar{\gamma}$, inches	σ , inches	$\eta_{\gamma} \times 10^{-4}$	$\frac{\sigma U_{\infty}}{\nu} \times 10^{-3}$	$n_{i\gamma}$, Hz
130.6	3.00	0.491	1.506	2.465	47.7
149.3	2.55	0.417	1.540	2.518	45.4
164.2	1.93	0.440	1.605	3.660	50.2
170.8	1.59	0.437	1.620	4.453	53.0
178.3	1.19	0.306	1.759	4.523	54.8
185.8	0.704	0.193	1.562	4.281	58.7

Table 5. Intermittency parameters for flow C.

Station, inches	γ
165.3	0.02
171.8	0.15
175.2	0.55
177.4	0.78
182.0	0.96
184.2	1.0
186.2	1.0

Table 6. Surface intermittency parameters for flow D.

time from the schmitt trigger output. A serious problem with this method arises due to the fact that several short duration pulses may occur as the probe volume enters and leaves the turbulent bulge thus giving rise to frequencies which are perhaps an order of magnitude higher than the actual.

In order to reduce the effects of this problem, the signal from the schmitt trigger was processed through a low pass filter which attenuated the short duration pulses responsible for the higher frequency. It was found that the resulting frequency obtained was quite dependent on the filter setting, so the filter setting was obtained by visual comparison of the unfiltered PM tube signal with the filtered schmitt trigger signal on a dual trace storage oscilloscope. Typical signal and oscilloscope traces from this method are given by Strickland and Simpson (1973). The filter was set such that there was a single zero crossing from negative to positive for each "significant" peak on the unfiltered PM tube signal. The filter setting chosen for all the results here was 300 Hz.

Figure 33 of Simpson and Wallace (1975) shows a typical bell-shaped frequency distribution such as obtained for flow C. The frequency distributions across the intermittent region for flow C are rather similar when the frequency is normalized on the frequency at \bar{Y}, n_{iY} . As for flows A and B, the peak frequency for each profile occurred at about the location where $\gamma = 0.6$. The n_{iY} for flow C was about twice the bursting frequency n_b when tables 3 and 5 are compared. Since the technique used to obtain the intermittency

frequency requires a certain amount of arbitrary judgment, as do techniques using hot-wires, it cannot be determined if the absolute values of these measurements are accurate. However, since for each flow n_b was proportional to n_{iy} , it appears that the large motion influencing the intermittency also influences the wall bursting frequency even downstream of the cessation of entrainment. Strickland and Simpson (1973) also found n_b to be proportional to n_{iy} for an adverse pressure gradient turbulent boundary layer. Thus, apparently this proportionality is present in turbulent boundary layers over a wide range of pressure gradient conditions.

For flow D the intermittency at the surface was determined for the retransition region downstream from the flush-surface hot-film signals. The taped signals were examined for high frequency content since considerable mixing and high frequency oscillations are associated with turbulent fluid. These signals were passed through the model 330B filter with a 200 Hz-2KHz bandpass and then through the multiplier used as a squarer in order to rectify the negative portions. This signal was low-pass filtered at 300 Hz using the model 3202 filter and passed through a schmitt trigger. The resultant pulses were visually compared with the original signals on a storage oscilloscope for validity as regions of high frequency content. These pulse periods were accumulatively counted for 50 sec. by the digital timer-counter. The fraction of time pulses were present was the intermittency γ . These results are presented in table 6. These same signals were processed by using the schmitt trigger on the

output signal of the model 330B filter. The resulting fraction of time positive pulses were present was doubled to get the intermittency since contributions from negative pulses had not been rectified. These latter results were within 5% of the results of table 6.

The results in table 6 follow a curve of the form of the integral of the normal distribution curve. γ increases slowly from about 165.3 inches to 171.8 inches, increases more rapidly up to 177.4 inches, and thereafter increases slowly to unity at about 184.2 inches. Upstream of 165.3 inches the flow had low frequency oscillations as shown in figures 28(a) and 29. It is clear in figures 30 that higher amplitude pulses were occasionally present at 165.3 inches. Figures 28(b) and (c) show the relatively high frequency oscillations in the high velocity pulses at 171.5 and 175.0 inches. The clearest oscilloscope traces are shown in figures 31 for 182.0 inches. The higher velocity regions contain high frequency oscillations. Regions of laminar-like flow follow each high velocity pulse. These velocity signals slowly decay, not because of limited sensor response but because of temporarily high velocity laminar flow that follows the turbulent pulses.

It is clear that in the low velocity wall regions downstream of the cessation of entrainment in flow D, the flow became progressively more laminar-like. The magnitude of the oscillations in these regions progressively decreased. However, beginning at 165.3 inches, high velocity fluid moved in toward the wall. The average frequency of occurrence of high velocity pulses in this downstream region was

about 25 Hz, as determined by counting these pulses. Further analysis of these data is planned.

4. DISCUSSION

Many aspects of flows C and D are similar to previous results reported by other investigators and by Simpson and Wallace (1975). In flow D and in the flow of Blackwelder and Kovasznay (1972), K increased to a value which exceeded 3.8×10^{-6} and decreased downstream to zero. In both flows, a local maximum in $C_f/2$ occurred at the same streamwise position as the K maximum; the minimum in $C_f/2$ occurred downstream of the minimum of the intermittency at the wall; the maximum H occurred upstream of the $C_f/2$ minimum and approximately at the minimum intermittency at the wall.

In all four flows measured in this research program, the behavior of the turbulent boundary layer after the beginning of strong acceleration was very similar. An initially normal low-pressure-gradient boundary layer first became distorted. The wake-like tail of the mean velocity profile became progressively weaker until at the cessation of entrainment none remained. It appears that the shape factor H is about a minimum at this location. The bursting frequency and intermittent bulge passage frequency downstream either increased or remained about constant along this length. The surface spanwise structure was not appreciably different from a low Reynolds number low-pressure-gradient boundary layer. Downstream the entire intermittent turbulent/non-turbulent interface was outside the

boundary layer thickness δ and the celerity of this region was the free-stream velocity.

Simpson and Wallace (1975) showed that normal stresses production was important in the mean turbulence kinetic energy balance

$$\frac{1}{2} \left\{ U \frac{\partial \overline{q^2}}{\partial x} + V \frac{\partial \overline{q^2}}{\partial y} \right\} + \frac{\partial}{\partial y} \left[\frac{\overline{p}V}{\rho} + \frac{1}{2} \overline{q^2} V \right] + \epsilon = -\overline{uv} \frac{\partial U}{\partial y} - (\overline{u^2} - \overline{v^2}) \frac{\partial U}{\partial x} \quad (17)$$

Here the terms are from left to right: advection, turbulent diffusion, dissipation, shear production, and normal stresses production. This last term is of opposite sign to the shear production term in strongly accelerated flows. The net turbulence energy production is less than the shear production by the factor

$$F = 1 - \frac{(\overline{u^2} - \overline{v^2}) \partial U / \partial x}{(-\overline{uv}) \partial U / \partial y} \quad (18)$$

which represents total production to shear production.

They also found that the normal stresses term reduces the diffusion of turbulence kinetic energy into the freestream, or the entrainment of non-turbulent fluid into the boundary layer. The velocity difference between turbulent fluid in the intermittent region and the irrotational freestream fluid approaches zero with strong acceleration. Thus, velocity profile instabilities which produce the eruption and eventual engulfment of free-stream fluid are eliminated. There could be no creation or merging of adjacent large eddies that accompanies the entrainment process. This also explains why the intermittency and bursting frequencies for all four flows remained about constant after cessation of entrainment.

Simpson and Wallace found that

$$V_E = 10F_\delta (-\overline{uv})_{\max} / U_\infty \quad (19)$$

described the entrainment velocity upstream of cessation for flows A and B. This scale characterizes the large eddy structure that is not only largely responsible for the various turbulence intensity levels in the turbulent fluid, but is directly responsible for the entrainment. When the negative normal stresses turbulence energy production term arises under strong acceleration, the available turbulence kinetic energy in the outer region is reduced so less large eddy energy is available for entrainment. This equation reduces to Bradshaw's relation for low acceleration boundary layers when $F_\delta = 1$. F_δ is given by equation (18) with all quantities evaluated at the boundary layer thickness δ . Using the relations $-\overline{uv} \approx 0.15 \overline{q^2}$, $\overline{u^2} \approx \frac{1}{2} \overline{q^2}$, and $\overline{v^2} \approx 0.2 \overline{q^2}$, which apply to entraining flows, they obtained

$$F_\delta = 1 - \frac{2K}{(\partial f / \partial \eta)_\delta} \quad (20)$$

Figure 36 shows this quantity along flows C and D. Note that negative values of F_δ occur after engulfment of non-turbulent fluid ceases. This does not mean that turbulent fluid is instantaneously reverting to a laminar state, but simply that progressively more turbulent fluid lies outside the δ location.

Figures 7 and 8 show the results obtained by integrating equation (19)

$$U_\infty (\delta - \delta^*) \Big|_{x_0}^x = \int_{x_0}^x V_E dx \quad (21)$$

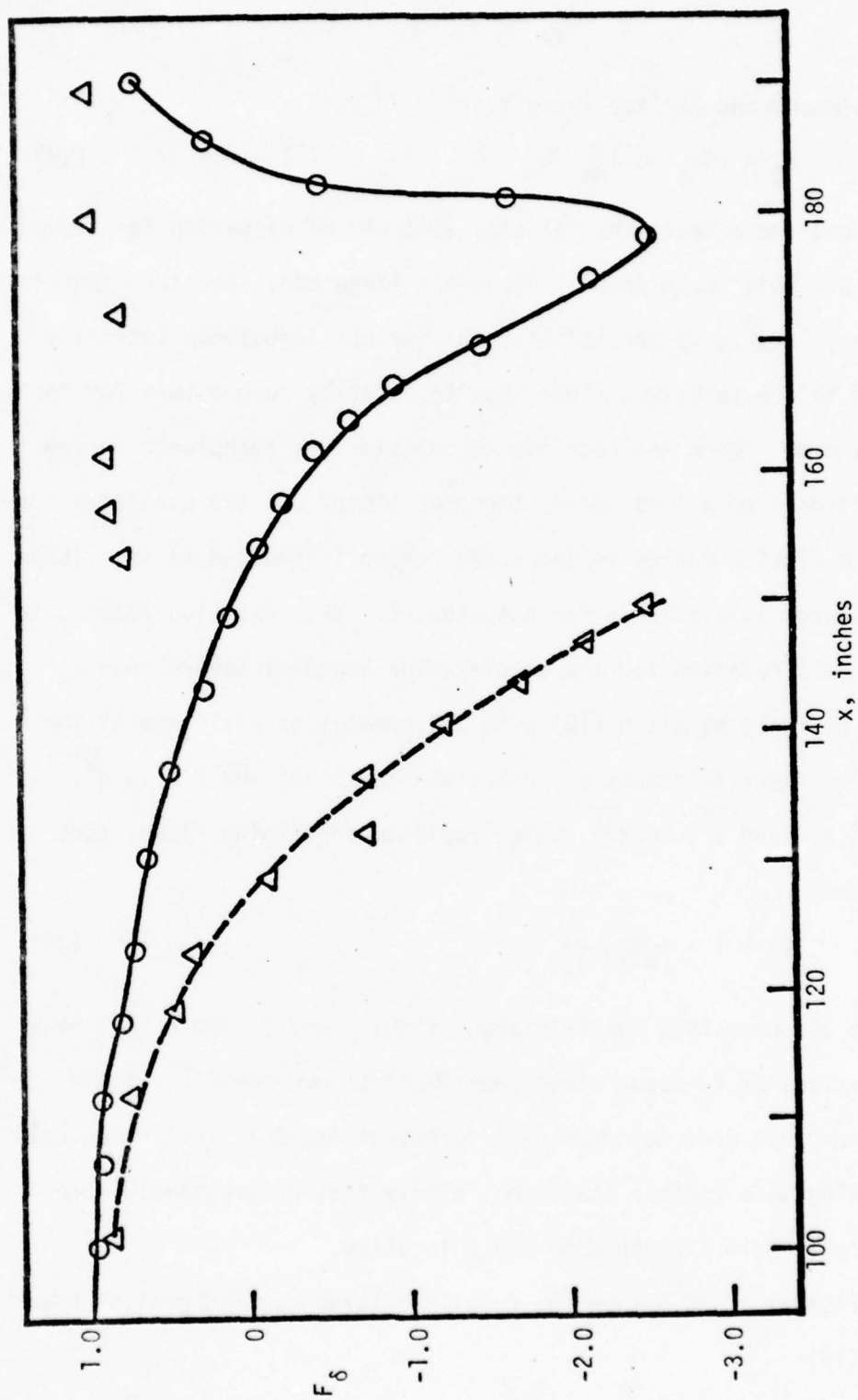


Figure 36. F_δ vs. x . Experimental values in eqn. (20): \circ , flow C; Δ , flow D. Lines for visual aid only.

For these computations the relation $(-\overline{uv})_{\max} \approx 0.3(\overline{u^2})_{\max}$ was used with experimental $(\overline{u^2})_{\max}$ values. The results are in good agreement with values determined directly from the mean velocity profiles, especially for flow C. Thus the growth and decline of the mean flow boundary layer is fairly well predicted by this model, at least to just downstream of the cessation of entrainment.

The observed flat $nF(n)$ region for $\overline{u^2}$ spectra emerges after some length of acceleration. The streamwise location where this behavior is first noticed does not seem to be directly related to the location where entrainment ceases. For flow A with $K = 2.17 \times 10^{-6}$, the $nF(n)$ spectra examined by Simpson and Wallace had no flat region, even downstream of the cessation of entrainment. For flow B with $K = 3.19 \times 10^{-6}$, no flat region was present in the spectra obtained upstream of the minimum H, while such a region was observed for spectra downstream. In flow C presented here, the flat region in some spectra began at about 137 inches while the cessation of entrainment did not occur until about 165 inches. Similarly for flow D entrainment ceased at about 132 inches while the flat $nF(n)$ region began at about 123 inches. A preliminary exploration of this behavior is that with strong acceleration, progressively weaker new low frequency oscillations are produced by the large-scaled motion while the higher frequency oscillations are produced by the breakdown of the more intense upstream large-scaled motions. Further analysis of these data is needed.

In flows A and B, asymptotic similarity flows were approached near the downstream end of the test section. This means that $\sqrt{u^2}/U_\infty$ vs. η similarity was present for $K < 3.19 \times 10^{-6}$. For flow C when $K > 3.6 \times 10^{-6}$, $\sqrt{u^2}/U_\infty$ profiles decayed. This means that had this K level been maintained downstream, true relaminarization would have eventually resulted, as suggested by Kline et al. (1967). Since there is a much shorter distance from the beginning of acceleration to the maximum K in flow D, the intensity $\sqrt{u^2}/U_\infty$ did not begin to decay near the wall until about 157 inches. At 161.6 inches, as shown in figure 20, a considerable amount of the intensity was due to unsteadiness rather than turbulence. Since K decreased downstream of 144 inches, retransition to a low acceleration turbulent boundary layer began at about 165 inches. In this region the flow possessed a highly laminar-like behavior, so $-\overline{uv}$ was extremely small. Evidently $\sqrt{v^2}$ decays considerably. As mentioned above, the surface spanwise structure upstream of the onset of decay of $\sqrt{u^2}/U_\infty$ was not appreciably different from that of a low Reynolds number low pressure gradient boundary layer. After the onset of decay of $\sqrt{u^2}/U_\infty$, λ_z^+ increased. Evidently the upstream λ_z values in these non-equilibrium flows persist downstream, so when normalized with a higher U_τ/ν , λ_z^+ is higher.

In the relaminarizing nozzle-type flow of Schraub and Kline (Kline et al. 1967), λ_z^+ was reported for the region of maximum K to be of the order of 200 for $K = 2.75 \times 10^{-6}$ and of the order of 300 for $K = 3.25 \times 10^{-6}$. On the surface, it would appear that they found

λ_z^+ to vary directly with K . However, their estimates of $C_f/2$ for these two streamwise locations seem high by about a factor of two when compared to the $C_f/2$ behavior in flow D and in the Blackwelder and Kovasznay (1972) nozzle flow. In that case, values of about 150 and 220 for λ_z^+ would result, respectively, and would agree reasonably well with the flow D results in the vicinity of the maximum K .

Schraub and Kline did not present λ_z results downstream of the K maximum, so the data from flow D are the only available on this downstream structure. λ_z^+ is still of the order of 300 while K decreases below 2×10^{-6} . After retransition to a low-accelerated low-pressure-gradient turbulent boundary layer begins, λ_z^+ is an order of magnitude greater. This behavior is as yet incompletely explained, so further analysis of these data is needed.

5. CONCLUSIONS AND RECOMMENDATIONS

The following conclusions can be made about turbulent boundary layers subjected to strong acceleration.

- a. The parameter K must be greater than about 3.6×10^{-6} for the decay of the upstream generated turbulence.
- b. For practical use in a nozzle only one short region downstream of the maximum K will possess a laminar-like behavior with significantly lower $C_f/2$ and heat transfer coefficients.
- c. The large eddy structure of the outer region governs the bursting frequency, the intermittent bulge passage frequency, and influences the wall flow behavior downstream. These frequencies

seem to approach constant values after the cessation of entrainment of non-turbulent fluid.

d. The wall spanwise structure appears to lag behind local conditions and to reflect upstream flow behavior. λ_z^+ seems to steadily increase to about 300 even after K has dropped below its maximum value in a nozzle flow. After retransition to a low accelerated turbulent boundary layer, a large λ_z^+ of the order of 3000 is observed.

e. The proposed modified entrainment model accounts for the reduction of available turbulence kinetic energy by the negative normal stresses production term of the turbulence kinetic energy equation.

f. A $nF(n)$ spectral distribution of $\overline{u^2}$ for $n > 1000$ appears to possess a flat region for laminar like boundary layers at large K values.

As a result of the large quantity of experimental data provided by the research program, the following recommendations for future work are suggested.

a. Further analysis of these data, some of which was not presented in this report because of the lack of time. Afterwards a manuscript should be submitted for journal publication. At that time a more intelligent assessment for future work can be made.

b. A generalized computational effort incorporating flow models reflected by all available data should be undertaken. Communication between the senior author and predictors has begun, but no results are yet available.

REFERENCES

- Blackwelder, R. F. and Kovasznay, L.S.G. (1972), "Large-scale Motion of a Turbulent Boundary Layer during Relaminarization," J. Fluid Mech., 53, pp. 61-83.
- Bradshaw, P. (1967a) "The Turbulence Structure of Equilibrium Boundary Layers," J. Fluid Mech., 29, pp. 625-645.
- Bradshaw, P. (1967b), "Conditions for the Existence of an Inertial Subrange in Turbulent Flow," Nat. Phys. Lab., Aero. Rept. No. 1220.
- Collis, D. C. and Williams, M. J. (1959), "Two-Dimensional Convection from Heated Wires at Low Reynolds Numbers," J. Fluid Mech., 6, pp. 357-384.
- Corrsin, S. (1964), "Further Generalizations of Onsager's Cascade Model for Turbulent Spectra," Phys. Fluids, 7, p. 1156.
- Fiedler, H. and Head, M. R. (1966), "Intermittency Measurements in the Turbulent Boundary Layer," J. Fluid Mech., 25, pp. 719-735.
- Freyruth, P. (1967), "Feedback Control Theory for Constant-Temperature Hot-Wire Anemometers," Rev. Sci. Inst., 38, pp. 677-681.
- Gupta, A. K., Laufer, J., and Kaplan, R. E. (1971), "Spatial Structure in the Viscous Sublayer," J. Fluid Mech., 50, pp. 493-512.
- Hinze, J. (. (1975), Turbulence, Second Edition, McGraw-Hill Book Co.
- Kays, W. M. (1966), Convective Heat and Mass Transfer, McGraw-Hill Book Co.
- Klebanoff, P. S. (1955), "Characteristics of Turbulence in a Boundary Layer with Zero Pressure Gradient," NACA Rept. 1247.
- Kline, S. J., and McClintock, F. A. (1953), "Describing Uncertainties in Single-Sample Experiments," Mech. Eng., 75, pp. 3-8.
- Kline, S. J., Reynolds, W. C., Schraub, F. A., and Runstadler, P. W. (1967), "The Structure of Turbulent Boundary Layers," J. Fluid Mech., 30, pp. 741-773.
- Laufer, J. (1954), "The Structure of Turbulence in Fully-developed Pipe Flow," NACA Rept. 1174.

- Moretti, P. M. and Kays, W. M. (1965), "Heat Transfer to a Turbulent Boundary Layer with Varying Free-stream Velocity and Varying Surface Temperature--An Experimental Study," Int. J. Heat Mass Trans., 8, pp. 1187-1202.
- Narasimha, R. and Sreenivasan, K. R. (1973), "Relaminarization in Highly Accelerated Turbulent Boundary Layers," J. Fluid Mech., 61, pp. 417-447.
- Nychas, S. G., Hershey, H. C., and Brodkey, R. S. (1973), "A Visual Study of Turbulent Shear Flow," J. Fluid Mech., 61, pp. 513-540.
- Oka, S. and Kostić, Ž. (1972), "Influence of Wall Proximity on Hot-Wire Velocity Measurements," DISA Information, No. 13, pp. 29-33.
- Rao, K. Narahari, Narasimha, R., and Badri Narayanan, M. A. (1971), "The 'Bursting' Phenomenon in a Turbulent Boundary Layer," J. Fluid Mech., 48, pp. 339-352.
- Rotta, J. C. (1962), "Turbulent Boundary Layers in Incompressible Flow," Progress in Aeronautical Sciences, Vol. 2, Pergamon Press.
- Sandborn, V. A. (1976), "Effect of Velocity Gradients in Measurements of Turbulent Shear Stress," AIAA Journal, 14, pp. 400-402.
- Schlichting, H. (1968), Boundary Layer Theory, 6th Edition, McGraw-Hill Book Co.
- Simpson, R. L. (1970), "Characteristics of Turbulent Boundary Layers at Low Reynolds Numbers with and without Transpiration," J. Fluid Mech., 42, pp. 769-802.
- Simpson, R. L. (1975), "Interpreting Signals of the Spanwise Spatial Structure in the Viscous Sublayer," Phys. Fluids., 18, pp. 1068-1069.
- Simpson, R. L. (1976), "An Investigation of the Spatial Structure of the Viscous Sublayer," Max-Planck-Institut für Strömungsforschung Bericht 118/1976.
- Simpson, R. L., Strickland, J. H., and Barr, P. W. (1974), "Laser and Hot-Film Anemometer Measurements in a Separating Turbulent Boundary Layer," Rept. WT-3, Southern Methodist University, Thermal and Fluid Sciences Center. Available from NTIS as AD-A001115.
- Simpson, R. L., Strickland, J. H., and Barr, P. W. (1977), "Features of a Separating Turbulent Boundary Layer in the Vicinity of Separation," J. Fluid Mech., 79, pp. 553-594.

- Simpson, R. L. and Wallace, D. B. (1975), "Laminariscient Turbulent Boundary Layers: Experiments on Sink Flows," Project SQUID Tech Rept. SMU-1-PU.
- Spencer, B. W. and Jones, B. G. (1971), "Turbulence Measurements with the Split-Film Anemometer Probe," Proceedings of Symposium on Turbulence in Liquids, Univ. Mo.- Rolla, pp. 7-15.
- Strickland, J. H. and Simpson, R. L. (1973), "The Separating Turbulent Boundary Layer: An Experimental Study of an Airfoil Type Flow," Rept. WT-2, Thermal and Fluid Sciences Center, Southern Methodist University. Available from NTIS as AD-771170/8GA.
- Strickland, J. H. and Simpson, R. L. (1975), "Bursting Frequencies Obtained from Wall Shear Stress Fluctuations in a Turbulent Boundary Layer," Phys. Fluids, 18, pp. 306-308.
- Wallace, J. M., Eckelmann, H., and Brodkey, R. S. (1972), "The Wall Region in Turbulent Shear Flow," J. Fluid Mech., 54, pp. 39-48.
- Willmarth, W. W. (1975), "Structure of Turbulence in Boundary Layers," Advances in Applied Mechanics, 15, pp. 159-253. Academic Press.
- Young, M. F. (1976), "Calibration of Hot-wires and Hot-films for Velocity Fluctuations," Rept. TMC-3, Thermosciences Div., Dept. Mechanical Engrg., Stanford Univ.

APPENDIX A - Mean velocity and streamwise fluctuation intensity $(\bar{u}^2)^{1/2}/U_\infty$ profile data, flow C,
linearly increasing K

X = 101.2				X = 112.2				X = 118.8				X = 123.1			
N	F	INTENSITY	N	F	INTENSITY	N	F	INTENSITY	N	F	INTENSITY	N	F	INTENSITY	N
27.	.1327	0.0339	36.	.1152	0.0337	22.	.1172	0.0258	56.	.1604	0.0494	152.	.6572	0.0875	452.
32.	.1382	0.0381	43.	.1215	0.0384	28.	.1288	0.0288	61.	.1693	0.0555	157.	.6591	0.0954	510.
38.	.1491	0.0382	49.	.1351	0.0436	34.	.1292	0.0327	67.	.1863	0.0570	179.	.6733	0.0997	570.
45.	.1809	0.0484	52.	.1445	0.0478	45.	.1439	0.0409	81.	.2282	0.0648	207.	.5178	0.0999	681.
57.	.2039	0.0549	62.	.1644	0.0549	56.	.1599	0.0457	95.	.2674	0.0752	235.	.5568	0.1024	789.
65.	.2412	0.0551	71.	.1854	0.0614	70.	.1874	0.0538	109.	.3204	0.0811	291.	.6696	0.1007	853.
91.	.3136	0.0776	83.	.2157	0.0692	84.	.2174	0.0620	123.	.3431	0.0867	347.	.6904	0.0952	952.
114.	.3717	0.0883	95.	.2482	0.0778	112.	.2457	0.0802	151.	.4591	0.0954	452.	.6572	0.0875	1051.
136.	.4112	0.0922	119.	.3016	0.0902	140.	.3032	0.0898	179.	.4733	0.0997	510.	.7224	0.0813	1151.
182.	.4679	0.0947	143.	.3581	0.0951	168.	.4136	0.0950	207.	.5178	0.0999	681.	.7602	0.0681	1251.
227.	.5329	0.0959	167.	.4421	0.0996	204.	.4840	0.1021	235.	.5568	0.1024	789.	.7825	0.0598	1351.
273.	.5636	0.0940	199.	.4335	0.1035	281.	.5453	0.1020	291.	.6696	0.1007	853.	.7768	0.0551	1451.
344.	.6053	0.0950	239.	.4901	0.1035	337.	.5688	0.1011	347.	.6904	0.0952	952.	.8102	0.0524	1551.
454.	.6223	0.0904	252.	.5313	0.1035	412.	.6513	0.0949	452.	.6572	0.0875	1051.	.8191	0.0516	1651.
585.	.6535	0.0784	361.	.5927	0.1004	561.	.6621	0.0868	510.	.7224	0.0813	1151.	.8314	0.0498	1751.
687.	.6121	0.0736	476.	.6354	0.0897	701.	.7114	0.0795	710.	.7469	0.0699	1251.	.8396	0.0497	1851.
909.	.6875	0.0708	575.	.6670	0.0891	842.	.7291	0.0726	850.	.7602	0.0681	1351.	.8425	0.0458	1951.
1135.	.7079	0.0669	714.	.6869	0.0853	1122.	.7549	0.0646	1129.	.7825	0.0598	1451.	.8495	0.0458	2051.
1362.	.7171	0.0657	982.	.7194	0.0752	1467.	.7735	0.0576	1469.	.7768	0.0551	1551.	.8562	0.0448	2151.
1590.	.7215	0.0661	1190.	.7414	0.0696	1693.	.7842	0.0549	1689.	.8102	0.0524	1651.	.8624	0.0416	2251.
1818.	.7259	0.0667	1420.	.7860	0.0653	2244.	.8078	0.0519	2241.	.8191	0.0516	1751.	.8694	0.0407	2351.
2272.	.7572	0.0637	1665.	.7717	0.0637	2805.	.8162	0.0506	2247.	.8314	0.0498	1851.	.8765	0.0372	2451.
2726.	.7643	0.0673	1903.	.7822	0.0626	3366.	.8579	0.0502	2806.	.8396	0.0497	1951.	.8842	0.0358	2551.
3435.	.7771	0.0658	2379.	.7989	0.0597	4488.	.8619	0.0523	4489.	.8425	0.0458	2051.	.8917	0.0357	2651.
4344.	.8072	0.0539	2895.	.8136	0.0583	5610.	.8619	0.0515	5612.	.8495	0.0458	2151.	.8975	0.0323	2751.
5453.	.8429	0.0510	3807.	.8400	0.0576	6732.	.9236	0.0494	6734.	.8624	0.0416	2251.	.9073	0.0317	2851.
6362.	.8404	0.0511	4798.	.8449	0.0519	7855.	.9432	0.0462	7857.	.8694	0.0407	2351.	.9157	0.0306	2951.
7271.	.9178	0.0525	5710.	.8869	0.0519	8977.	.9432	0.0462	8979.	.8765	0.0372	2451.	.9275	0.0293	3051.
8179.	.9408	0.0474	6662.	.9110	0.0516	10099.	.9432	0.0462	10099.	.8842	0.0358	2551.	.9357	0.0284	3151.
9246.	.9627	0.0421	7613.	.9330	0.0494	11221.	.9432	0.0462	11221.	.8917	0.0357	2651.	.9473	0.0279	3251.
10274.	.9625	0.0333	8565.	.9518	0.0467	12623.	.9432	0.0462	12623.	.8917	0.0357	2651.	.9557	0.0264	3351.
11346.	.9625	0.0289	9517.	.9717	0.0444	14026.	.9432	0.0462	14026.	.8917	0.0357	2651.	.9637	0.0263	3451.
12456.	.9999	0.0294	10766.	.9937	0.0379	15956.	.9432	0.0462	15956.	.8917	0.0357	2651.	.9717	0.0263	3551.
13632.	1.0000	0.0203	11896.	1.0000	0.0275										

Y shift = 0.002

BEST AVAILABLE COPY

BEST AVAILABLE COPY

λ = 128.4				λ = 132.2				λ = 136.7				λ = 140.7			
λ	F	INTENSITY		λ	F	INTENSITY		λ	F	INTENSITY		λ	F	INTENSITY	
27.	.1109	0.0196		42.	.1982	0.0551		33.	.1217	0.0265		115.	.2952	0.0731	
30.	.1168	0.0246		46.	.2156	0.0618		42.	.1413	0.0304		124.	.3132	0.0738	
40.	.1271	0.0311		75.	.2259	0.0523		50.	.1506	0.0343		133.	.3306	0.0754	
45.	.1323	0.0400		82.	.2456	0.0559		67.	.1607	0.0415		138.	.3701	0.0787	
67.	.1626	0.0481		92.	.2618	0.0727		83.	.1716	0.0514		168.	.4413	0.0818	
81.	.2086	0.0554		109.	.3302	0.0609		108.	.2490	0.0584		186.	.4482	0.0819	
94.	.2449	0.0645		126.	.3724	0.0671		117.	.2696	0.0637		203.	.4794	0.0832	
108.	.2712	0.0705		144.	.4174	0.0919		133.	.2896	0.0705		226.	.5149	0.0910	
121.	.3045	0.0764		178.	.4686	0.0943		136.	.3498	0.0761		246.	.5332	0.0923	
135.	.3333	0.0801		212.	.5129	0.0944		167.	.4069	0.0797		292.	.6199	0.0978	
148.	.3622	0.0850		246.	.6137	0.0998		187.	.4516	0.0839		336.	.6718	0.0978	
162.	.3976	0.0909		280.	.6431	0.0946		208.	.4859	0.0873		360.	.7138	0.0915	
212.	.4444	0.1062		348.	.7114	0.0998		250.	.5577	0.0941		449.	.7714	0.0874	
238.	.4932	0.1009		412.	.7422	0.0921		291.	.6113	0.0947		532.	.8113	0.0745	
317.	.6116	0.1009		544.	.7915	0.0819		333.	.6679	0.0949		734.	.8652	0.0604	
484.	.6449	0.0790		648.	.8171	0.0741		410.	.7499	0.0918		911.	.8845	0.0613	
539.	.7102	0.0905		867.	.8418	0.0656		509.	.7708	0.0870		1132.	.8625	0.0561	
674.	.7675	0.0817		1032.	.8557	0.0600		668.	.8223	0.0813		1353.	.9177	0.0490	
843.	.7973	0.0730		1374.	.8695	0.0508		833.	.8516	0.0699		1755.	.9324	0.0360	
1011.	.8074	0.0716		1716.	.8812	0.0457		1041.	.8694	0.0606		2798.	.9414	0.0240	
1345.	.8183	0.0573		2058.	.8885	0.0476		1248.	.8833	0.0508		2845.	.9434	0.0244	
1805.	.8455	0.0506		2399.	.8956	0.0405		1655.	.8963	0.0407		3122.	.9577	0.0251	
2022.	.8664	0.0470		2741.	.9052	0.0373		2081.	.9037	0.0360		3504.	.9611	0.0218	
2575.	.8662	0.0445		3425.	.9155	0.0354		2498.	.9182	0.0335		4449.	.9676	0.0232	
2897.	.8794	0.0432		4108.	.9229	0.0343		2914.	.9144	0.0316		5333.	.9713	0.0228	
3371.	.8825	0.0408		4792.	.9308	0.0328		3316.	.9184	0.0300		7102.	.9758	0.0222	
4445.	.8905	0.0382		5476.	.9375	0.0318		4153.	.9276	0.0280		8871.	.9855	0.0167	
5303.	.9227	0.0357		6063.	.9426	0.0293		4996.	.9378	0.0267		10039.	.9921	0.0154	
6741.	.9377	0.0344		7977.	.9557	0.0267		6661.	.9515	0.0249		12428.	.9977	0.0090	
8599.	.9476	0.0317		10445.	.9667	0.0226		8326.	.9535	0.0216		14172.	1.0000	0.0065	
9699.	.9636	0.0288		12112.	.9654	0.0170		9901.	.9755	0.0196					
10788.	.9711	0.0250		13619.	.9913	0.0129		11656.	.9874	0.0159					
12135.	.9867	0.0192		15388.	.9956	0.0093		13321.	.9920	0.0122					
13463.	.9998	0.0132						14987.	.9962	0.0090					
15168.	1.0000							16652.	1.0000	0.0072					

γ white = 0.003

γ white = 0.001

BEST AVAILABLE COPY

Σ = 143.8				Σ = 146.8				Σ = 149.7				Σ = 152.6			
H	F	INTENSITY		H	F	INTENSITY		H	F	INTENSITY		H	F	INTENSITY	
18.	.1195	0.0134		79.	.2916	0.0467		42.	.2213	0.0513		155.	.3481	0.0452	
21.	.1222	0.0170		76.	.2254	0.0498		185.	.2449	0.0553		166.	.2677	0.0468	
21.	.1308	0.0232		182.	.2792	0.0523		131.	.2824	0.0628		183.	.3494	0.0697	
42.	.1418	0.0291		113.	.2122	0.0551		159.	.3391	0.0694		199.	.4221	0.0725	
52.	.1591	0.0346		124.	.2648	0.0648		189.	.3876	0.0743		214.	.4449	0.0732	
73.	.1759	0.0448		136.	.2334	0.0618		216.	.4416	0.0802		289.	.5177	0.0812	
90.	.2079	0.0528		152.	.3159	0.0657		237.	.4439	0.0832		292.	.5212	0.0744	
115.	.2576	0.0593		181.	.4217	0.0705		243.	.5218	0.0874		290.	.5177	0.0812	
136.	.2966	0.0637		209.	.4786	0.0742		296.	.5658	0.0883		307.	.6446	0.0796	
157.	.3496	0.0717		237.	.5404	0.0805		308.	.6489	0.0899		405.	.6976	0.0790	
183.	.3925	0.0727		265.	.5873	0.0845		394.	.6826	0.0889		443.	.7194	0.0795	
209.	.4377	0.0750		294.	.6317	0.0864		456.	.7884	0.0813		482.	.7636	0.0785	
242.	.5353	0.0918		322.	.6698	0.0874		457.	.8517	0.0708		520.	.8526	0.0787	
311.	.6224	0.0981		358.	.6716	0.0856		1891.	.9158	0.0443		596.	.9384	0.0758	
367.	.6876	0.0991		487.	.7472	0.0843		1911.	.9158	0.0443		673.	.9395	0.0770	
471.	.7558	0.0946		483.	.7949	0.0784		1911.	.9158	0.0443		749.	.9448	0.0690	
576.	.8173	0.0813		589.	.8356	0.0720		1911.	.9158	0.0443		829.	.9175	0.0619	
786.	.8972	0.0682		576.	.8516	0.0745		1911.	.9158	0.0443		916.	.9448	0.0528	
995.	.9177	0.0545		489.	.8827	0.0657		1911.	.9158	0.0443		916.	.9448	0.0528	
1204.	.9492	0.0532		482.	.8487	0.0558		1911.	.9158	0.0443		916.	.9448	0.0528	
1415.	.9336	0.0391		915.	.9472	0.0500		1911.	.9158	0.0443		916.	.9448	0.0528	
1622.	.9624	0.0513		1141.	.9746	0.0434		1911.	.9158	0.0443		916.	.9448	0.0528	
1837.	.9677	0.0349		1387.	.9493	0.0352		1911.	.9158	0.0443		916.	.9448	0.0528	
2042.	.9718	0.0317		1593.	.9554	0.0395		1911.	.9158	0.0443		916.	.9448	0.0528	
2309.	.9453	0.0201		1819.	.9596	0.0280		1911.	.9158	0.0443		916.	.9448	0.0528	
2566.	.9546	0.0276		2044.	.9634	0.0251		1911.	.9158	0.0443		916.	.9448	0.0528	
2899.	.9643	0.0287		2276.	.9676	0.0230		1911.	.9158	0.0443		916.	.9448	0.0528	
4137.	.9795	0.0222		2557.	.9676	0.0214		1911.	.9158	0.0443		916.	.9448	0.0528	
5189.	.9718	0.0197		2815.	.9676	0.0200		1911.	.9158	0.0443		916.	.9448	0.0528	
6232.	.9746	0.0179		3486.	.9746	0.0184		1911.	.9158	0.0443		916.	.9448	0.0528	
8329.	.9842	0.0158		4527.	.9746	0.0160		1911.	.9158	0.0443		916.	.9448	0.0528	
10421.	.9924	0.0132		5637.	.9619	0.0152		1911.	.9158	0.0443		916.	.9448	0.0528	
12516.	.9971	0.0102		6787.	.9659	0.0140		1911.	.9158	0.0443		916.	.9448	0.0528	
14610.	1.0000	0.0077		7918.	.9659	0.0134		1911.	.9158	0.0443		916.	.9448	0.0528	
				8848.	.9712	0.0125		1911.	.9158	0.0443		916.	.9448	0.0528	
				11397.	.9656	0.0100		1911.	.9158	0.0443		916.	.9448	0.0528	
				13544.	.9987	0.0076		1911.	.9158	0.0443		916.	.9448	0.0528	
				15825.	1.0000	0.0060		1911.	.9158	0.0443		916.	.9448	0.0528	

Σ 143.8 - 0.006

Σ 146.8 - 0.001

Σ 149.7 - 0.004

BEST AVAILABLE COPY

X = 172.5				X = 161.6				X = 172.6				X = 179.7			
N	F	INTENSITY		N	F	INTENSITY		N	F	INTENSITY		N	F	INTENSITY	
100.	.2346	0.0060		135.	.3210	0.0769		291.	.3290	0.0924		283.	.4745	0.0865	
119.	.2677	0.0719		159.	.3513	0.0806		333.	.3512	0.0944		331.	.4903	0.0832	
138.	.3145	0.0768		183.	.3768	0.0789		375.	.3852	0.0959		378.	.5119	0.0899	
156.	.3523	0.0775		207.	.3775	0.0811		416.	.4260	0.0954		425.	.5133	0.0895	
175.	.3912	0.0779		231.	.3947	0.0789		458.	.4622	0.0938		472.	.5333	0.0895	
213.	.4650	0.0780		256.	.4212	0.0788		500.	.5034	0.0911		567.	.5766	0.0867	
251.	.5242	0.0753		280.	.4528	0.0784		541.	.5356	0.0899		601.	.6095	0.0849	
289.	.5758	0.0753		328.	.5232	0.0775		624.	.5972	0.0816		756.	.6376	0.0838	
326.	.6266	0.0756		376.	.5844	0.0773		708.	.6451	0.0749		850.	.6649	0.0825	
364.	.6702	0.0764		424.	.6212	0.0762		791.	.6865	0.0712		945.	.7026	0.0834	
401.	.7054	0.0761		473.	.6565	0.0760		874.	.7229	0.0693		1065.	.7262	0.0813	
448.	.7464	0.0754		533.	.7146	0.0731		957.	.7566	0.0691		1181.	.7451	0.0797	
495.	.7844	0.0733		593.	.7495	0.0714		1062.	.7957	0.0682		1417.	.7727	0.0768	
532.	.8381	0.0658		714.	.8105	0.0708		1164.	.8234	0.0684		1654.	.7943	0.0746	
684.	.8784	0.0606		834.	.8543	0.0668		1374.	.8727	0.0558		1850.	.8152	0.0723	
778.	.9053	0.0566		955.	.8981	0.0614		1582.	.9099	0.0620		2362.	.8547	0.0687	
966.	.9492	0.0460		1196.	.9415	0.0504		1790.	.9263	0.0589		2835.	.8849	0.0659	
1155.	.9638	0.0384		1437.	.9626	0.0426		2206.	.9516	0.0497		3307.	.9121	0.0624	
1532.	.9862	0.0282		1919.	.9872	0.0259		2623.	.9679	0.0414		3780.	.9360	0.0573	
1908.	.9944	0.0217		2451.	.9944	0.0187		3039.	.9776	0.0347		4724.	.9412	0.0492	
2245.	.9979	0.0177		2884.	.9965	0.0145		3455.	.9828	0.0278		5669.	.9677	0.0403	
2682.	.9992	0.0153		3366.	.9986	0.0116		3872.	.9883	0.0219		6614.	.9871	0.0307	
3039.	1.0000	0.0137		3848.	1.0000	0.0102		4208.	.9917	0.0179		7559.	.9991	0.0155	
								5120.	.9969	0.0122		8504.	1.0000	0.0104	
								5953.	1.0000	0.0091					

y shift = -0.0004

y shift = 0.0013

y shift = 0.003

BEST AVAILABLE COPY

X = 100.83			INTENSITY
N	F		
305.	.4986		0.0835
356.	.5244		0.0818
407.	.5436		0.0816
458.	.5585		0.0812
509.	.5732.		0.0809
610.	.6020		0.0811
712.	.6162		0.0798
814.	.6297		0.0789
916.	.6451		0.0783
1017.	.6560		0.0773
1144.	.6687		0.0767
1272.	.6782		0.0760
1399.	.6956		0.0753
1524.	.7065.		0.0743
1780.	.7234		0.0727
2034.	.7362		0.0710
2543.	.7594		0.0684
3052.	.7809		0.0661
3560.	.7993		0.0640
4069.	.8127		0.0620
4578.	.8251		0.0594
5086.	.8472		0.0576
6103.	.8759		0.0532
7121.	.8865		0.0501
8138.	.9105		0.0461
9155.	.9312		0.0423
10172.	.9537		0.0382
11444.	.9193		0.0283
12715.	.9904		0.0217
13981.	.9963		0.0152
15259.	1.0000		0.0112

APPENDIX B - Mean velocity and streamwise fluctuation intensity $(\bar{u})^{1/2}/U$ profile data, flow D, nozzle flow

X = 88.0			X = 101.10			X = 106.90			X = 112.0		
N	F	INTENSITY	N	F	INTENSITY	N	F	INTENSITY	N	F	INTENSITY
65.	.1175	0.0190	64.	.1375	0.0288	43.	.1199	0.0170	66.	.1341	0.0263
67.	.1454	0.0320	65.	.1657	0.0388	64.	.1420	0.0284	68.	.1705	0.0398
69.	.1723	0.0407	127.	.2503	0.0648	66.	.1735	0.0408	132.	.2444	0.0635
134.	.2372	0.0623	170.	.3150	0.0802	129.	.2410	0.0618	176.	.3137	0.0790
178.	.2942	0.0789	212.	.3643	0.0897	171.	.3062	0.0810	219.	.3763	0.0909
223.	.3446	0.0863	276.	.4266	0.0926	214.	.3597	0.0892	285.	.4320	0.0939
290.	.4005	0.0897	340.	.4642	0.0947	279.	.4261	0.0928	351.	.4843	0.0948
357.	.4409	0.0885	425.	.5089	0.0941	343.	.4410	0.0945	439.	.5161	0.0899
446.	.4424	0.0896	531.	.5430	0.0874	429.	.5066	0.0926	549.	.5604	0.0862
558.	.5124	0.0834	617.	.5676	0.0834	536.	.5425	0.0909	658.	.5820	0.0820
669.	.5320	0.0821	849.	.5900	0.0792	643.	.5623	0.0833	878.	.6093	0.0745
892.	.5616	0.0766	1062.	.6099	0.0746	857.	.5972	0.0755	1097.	.6298	0.0709
1227.	.5988	0.0725	1274.	.6276	0.0710	1179.	.6310	0.0711	1317.	.6468	0.0668
1561.	.6198	0.0702	1699.	.6628	0.0700	1500.	.6496	0.0678	1756.	.6695	0.0633
2097.	.6467	0.0683	2123.	.6928	0.0656	1929.	.6740	0.0634	2145.	.6923	0.0614
2676.	.6791	0.0669	2760.	.7122	0.0637	2572.	.6997	0.0627	2853.	.7127	0.0608
3548.	.7194	0.0649	3397.	.7310	0.0629	3429.	.7322	0.0609	3512.	.7389	0.0590
4460.	.7580	0.0649	4246.	.7815	0.0623	4206.	.7625	0.0598	4390.	.7662	0.0608
5575.	.8011	0.0628	5368.	.8039	0.0594	5358.	.7951	0.0571	5447.	.8048	0.0585
6600.	.8469	0.0614	6369.	.8415	0.0588	6430.	.8300	0.0547	6585.	.8355	0.0579
7805.	.8893	0.0576	7431.	.8779	0.0558	7501.	.8673	0.0534	7682.	.8696	0.0574
8920.	.9275	0.0516	8492.	.9143	0.0531	8573.	.9034	0.0529	8779.	.9026	0.0551
10035.	.9588	0.0403	9554.	.9425	0.0438	9644.	.9336	0.0451	9877.	.9344	0.0485
11150.	.9934	0.0270	10615.	.9696	0.0346	10716.	.9639	0.0357	10974.	.9611	0.0337
12265.	.9969	0.0173	11677.	.9972	0.0227	11788.	.9814	0.0353	12072.	.9823	0.0264
13360.	.9997	0.0130	12738.	.9960	0.0159	12859.	.9942	0.0176	13149.	.9947	0.0201
14495.	1.0000	0.0111	13800.	1.0000	0.0138	13931.	.9988	0.0140	14267.	.9991	0.0141
			14851.	.9994	0.0114	15002.	1.0000	0.0107	15364.	1.0000	0.0117
			15923.	.9989	0.0107				16462.	.9991	0.0103

BEST AVAILABLE COPY

BEST AVAILABLE COPY

X = 117.90				X = 123.15				X = 130.60				X = 137.20			
N	F	INTENSITY		N	F	INTENSITY		N	F	INTENSITY		N	F	INTENSITY	
46.	.1942	0.0348		48.	.1215	0.0172		50.	.2098	0.0138		43.	.1288	0.0122	
69.	.2622	0.0541		73.	.1637	0.0359		66.	.1452	0.0251		54.	.1297	0.0165	
82.	.3324	0.0650		97.	.2203	0.0531		75.	.1701	0.0348		65.	.1446	0.0242	
119.	.4122	0.0751		121.	.2348	0.0567		100.	.2246	0.0541		61.	.1705	0.0373	
145.	.4737	0.0771		145.	.2739	0.0664		125.	.2904	0.0706		106.	.2132	0.0559	
231.	.5083	0.0812		194.	.3521	0.0813		151.	.3461	0.0786		135.	.2623	0.0658	
301.	.5363	0.0801		242.	.4077	0.0895		201.	.4286	0.0887		142.	.3142	0.0765	
378.	.5601	0.0792		315.	.4664	0.0946		251.	.4863	0.0918		148.	.3531	0.0837	
462.	.5795	0.0767		389.	.5096	0.0933		326.	.5579	0.0872		215.	.3939	0.0903	
578.	.5903	0.0740		445.	.5467	0.0906		401.	.6007	0.0837		269.	.4541	0.1020	
644.	.6043	0.0708		606.	.5969	0.0835		502.	.6325	0.0794		350.	.5236	0.1043	
925.	.6237	0.0658		727.	.6054	0.0746		627.	.6684	0.0714		431.	.5737	0.1016	
1159.	.6442	0.0648		949.	.6353	0.0685		753.	.6743	0.0691		538.	.6237	0.0944	
1347.	.6476	0.0607		1444.	.6703	0.0600		1003.	.6962	0.0635		673.	.6417	0.0849	
1850.	.6798	0.0613		1939.	.6919	0.0560		1505.	.7230	0.0561		808.	.6877	0.0787	
2312.	.6964	0.0567		2544.	.7136	0.0541		2007.	.7469	0.0537		1077.	.7146	0.0680	
3006.	.7198	0.0568		3150.	.7331	0.0560		2614.	.7438	0.0555		1346.	.7368	0.0629	
3699.	.7457	0.0557		3877.	.7547	0.0575		3261.	.7777	0.0573		1615.	.7525	0.0606	
4624.	.7683	0.0571		4846.	.7825	0.0589		4014.	.7996	0.0592		2154.	.7720	0.0588	
5780.	.8072	0.0585		6058.	.8196	0.0608		5017.	.8235	0.0574		2602.	.7905	0.0565	
6936.	.8417	0.0614		7269.	.8474	0.0579		6272.	.8593	0.0561		3500.	.8100	0.0531	
8082.	.8751	0.0576		8441.	.8814	0.0566		7524.	.8891	0.0540		4207.	.8134	0.0526	
9249.	.9001	0.0533		9643.	.9154	0.0501		8741.	.9150	0.0489		5304.	.8545	0.0510	
10405.	.9409	0.0432		10994.	.9452	0.0423		10035.	.9408	0.0436		6730.	.8604	0.0491	
11561.	.9641	0.0335		12116.	.9668	0.0345		11249.	.9597	0.0366		8076.	.9110	0.0451	
12717.	.9824	0.0246		13327.	.9843	0.0240		12544.	.9776	0.0272		9422.	.9206	0.0425	
13873.	.9938	0.0169		14539.	.9936	0.0170		13798.	.9906	0.0194		10748.	.9510	0.0377	
15029.	.9942	0.0125		15750.	.9989	0.0125		15052.	.9975	0.0137		12115.	.9703	0.0299	
16185.	1.0000	0.0103		16720.	1.0008	0.0107		16307.	1.0000	0.0108		13461.	.9852	0.0252	
17341.	.9996	0.0096						17310.	.9975	0.0096		14807.	.9944	0.0177	
												16153.	.9981	0.0116	
												17409.	1.0000	0.0107	
												18645.	.9991	0.0097	

BEST AVAILABLE COPY

X = 143.50				X = 149.30				X = 154.50				X = 157.80			
N	F	INTENSITY		N	F	INTENSITY		N	F	INTENSITY		N	F	INTENSITY	
57.	.1461	0.0294		48.	.1380	0.0198		53.	.1497	0.0288		42.	.1293	0.0161	
55.	.1998	0.0500		91.	.1815	0.0404		67.	.1964	0.0406		56.	.1343	0.0202	
114.	.2609	0.0630		121.	.2394	0.0570		83.	.2193	0.0514		70.	.1493	0.0289	
142.	.3126	0.0765		151.	.3024	0.0731		100.	.2560	0.0585		87.	.1743	0.0398	
171.	.3537	0.0829		181.	.3335	0.0864		133.	.3256	0.0744		105.	.2150	0.0501	
228.	.4316	0.0930		242.	.4402	0.0960		167.	.3780	0.0850		140.	.2830	0.0676	
285.	.4845	0.0950		302.	.5222	0.1035		200.	.4356	0.0923		175.	.3643	0.0829	
370.	.5568	0.0956		362.	.5742	0.1073		233.	.4050	0.1019		210.	.4221	0.0954	
456.	.6085	0.0934		423.	.6164	0.1039		267.	.5240	0.1059		279.	.5193	0.1056	
570.	.6549	0.0917		483.	.6552	0.1038		333.	.5891	0.1084		349.	.5936	0.1126	
712.	.6890	0.0833		604.	.7040	0.0966		433.	.6639	0.1088		454.	.6757	0.1089	
855.	.7074	0.0769		755.	.7403	0.0875		533.	.7180	0.0978		559.	.7229	0.1006	
1140.	.7275	0.0723		906.	.7643	0.0775		667.	.7522	0.0877		609.	.7707	0.0911	
1425.	.7512	0.0688		1208.	.7915	0.0654		833.	.7882	0.0772		873.	.8021	0.0759	
1710.	.7748	0.0523		1510.	.8155	0.0567		1000.	.8199	0.0693		1048.	.8307	0.0626	
2200.	.8002	0.0505		1812.	.8207	0.0551		1333.	.8428	0.0582		1397.	.8550	0.0544	
2450.	.8212	0.0522		2418.	.8461	0.0469		1667.	.8493	0.0599		1747.	.8693	0.0534	
3705.	.8440	0.0480		3020.	.8634	0.0450		2000.	.8743	0.0461		2066.	.8829	0.0409	
4560.	.8600	0.0454		3926.	.8808	0.0406		2667.	.8915	0.0400		2794.	.8957	0.0356	
5760.	.8825	0.0435		4832.	.8973	0.0388		3333.	.9019	0.0364		3493.	.9071	0.0329	
7125.	.9044	0.0405		6039.	.9146	0.0362		4333.	.9139	0.0319		4541.	.9229	0.0305	
8549.	.9245	0.0370		7549.	.9328	0.0336		5333.	.9251	0.0314		5569.	.9336	0.0279	
9974.	.9453	0.0336		9053.	.9510	0.0303		6667.	.9386	0.0297		6986.	.9457	0.0266	
11399.	.9648	0.0289		10549.	.9675	0.0277		8333.	.9543	0.0277		8733.	.9593	0.0259	
12824.	.9779	0.0229		12079.	.9807	0.0225		10000.	.9678	0.0254		10479.	.9714	0.0226	
14249.	.9901	0.0169		13549.	.9907	0.0164		11667.	.9798	0.0213		12226.	.9836	0.0186	
15674.	.9960	0.0116		15099.	.9962	0.0131		13333.	.9895	0.0177		13972.	.9914	0.0139	
17099.	.9990	0.0092		16608.	.9999	0.0110		15000.	.9963	0.0127		15719.	.9979	0.0106	
18524.	1.0000	0.0082		18114.	1.0000	0.0077		16667.	.9993	0.0093		17465.	1.0000	0.0087	
19449.	.9992	0.0079		19628.	.9986	0.0069		18333.	1.0000	0.0079		19212.	1.0000	0.0079	
								20000.	.9993	0.0078					

BEST AVAILABLE COPY

X = 162.00				X = 164.20				X = 166.80				X = 170.80			
N	F	INTENSITY		N	F	INTENSITY		N	F	INTENSITY		N	F	INTENSITY	
78.	.2814	0.0650		87.	.1454	0.0415		89.	.1962	0.0397		82.	.1792	0.0289	
97.	.2840	0.0657		83.	.2108	0.0438		134.	.2723	0.0559		142.	.2179	0.0382	
110.	.3143	0.0728		104.	.2424	0.0511		179.	.3624	0.0723		127.	.2684	0.0465	
136.	.3434	0.0760		125.	.3137	0.0611		223.	.4422	0.0879		143.	.3262	0.0550	
155.	.3823	0.0876		166.	.4379	0.0816		248.	.5138	0.0958		178.	.3766	0.0647	
184.	.4624	0.0998		208.	.5664	0.0876		312.	.5754	0.0994		244.	.4231	0.0712	
232.	.5139	0.1075		250.	.6159	0.0876		357.	.6167	0.0975		245.	.5113	0.0784	
271.	.5712	0.1108		291.	.6637	0.0816		446.	.6922	0.0933		366.	.5916	0.0828	
310.	.5982	0.1108		333.	.7259	0.0744		536.	.7380	0.0866		347.	.6533	0.0851	
347.	.6736	0.1032		416.	.7750	0.0672		625.	.7760	0.0829		408.	.7081	0.0860	
504.	.7302	0.0928		499.	.7990	0.0630		759.	.8163	0.0757		459.	.7434	0.0877	
620.	.7721	0.0799		582.	.8152	0.0606		803.	.8448	0.0692		549.	.7742	0.0833	
775.	.8114	0.0721		707.	.8162	0.0558		1116.	.8672	0.0564		611.	.8252	0.0763	
948.	.8374	0.0617		832.	.8478	0.0529		1339.	.8862	0.0493		713.	.8570	0.0668	
1142.	.8509	0.0513		1040.	.8668	0.0505		1785.	.9057	0.0412		815.	.8795	0.0596	
1550.	.8681	0.0449		1248.	.8764	0.0475		2231.	.9186	0.0367		1019.	.9060	0.0497	
1917.	.8758	0.0410		1664.	.8962	0.0427		2678.	.9259	0.0314		1274.	.9216	0.0395	
2712.	.9015	0.0359		2080.	.9034	0.0380		3570.	.9359	0.0276		1528.	.9314	0.0346	
3875.	.9190	0.0303		2496.	.9168	0.0350		4441.	.9454	0.0222		2030.	.9432	0.0407	
5037.	.9305	0.0290		3327.	.9238	0.0321		5801.	.9555	0.0234		2547.	.9510	0.0252	
6199.	.9408	0.0274		4149.	.9348	0.0299		7140.	.9628	0.0213		3067.	.9564	0.0230	
7749.	.9531	0.0266		5667.	.9456	0.0273		8925.	.9728	0.0199		4076.	.9647	0.0200	
9646.	.9666	0.0243		6653.	.9544	0.0259		10710.	.9822	0.0174		5095.	.9766	0.0195	
11624.	.9788	0.0207		8318.	.9628	0.0234		12445.	.9880	0.0147		6623.	.9760	0.0170	
13541.	.9904	0.0158		10306.	.9768	0.0213		14280.	.9932	0.0131		8152.	.9814	0.0161	
15498.	.9962	0.0132		12478.	.9868	0.0175		16065.	.9973	0.0100		10180.	.9873	0.0146	
17435.	.9985	0.0107		14557.	.9948	0.0129		17850.	.9991	0.0092		12228.	.9927	0.0123	
19373.	1.0000	0.0090		16637.	.9982	0.0106		19635.	1.0000	0.0083		14265.	.9971	0.0105	
19922.	.9992	0.0088		18710.	1.0000	0.0091		21420.	.9990	0.0078		16343.	.9980	0.0088	
				20796.	.9994	0.0088						18341.	1.0000	0.0079	
												20379.	.9990	0.0072	

BEST AVAILABLE COPY

X = 175.00				X = 178.30				X = 181.20				X = 182.30			
N	F	INTENSITY		N	F	INTENSITY		N	F	INTENSITY		N	F	INTENSITY	
96.	.2645	0.0465		89.	.2660	0.0626		116.	.3040	0.0438		106.	.1608	0.0215	
120.	.3203	0.0556		118.	.3184	0.0699		132.	.3273	0.0462		144.	.2312	0.0338	
144.	.3524	0.0638		146.	.3656	0.0775		165.	.3882	0.0547		180.	.2924	0.0388	
179.	.4158	0.0705		165.	.4247	0.0864		207.	.4680	0.0652		225.	.3691	0.0460	
209.	.4754	0.0763		222.	.4668	0.0925		248.	.5402	0.0707		270.	.4544	0.0562	
239.	.5138	0.0805		259.	.5375	0.0993		289.	.6042	0.0776		315.	.5204	0.0579	
289.	.5907	0.0909		286.	.5982	0.1047		331.	.6434	0.0800		360.	.5768	0.0640	
359.	.6610	0.0980		370.	.6604	0.1053		413.	.7337	0.0830		414.	.6405	0.0712	
419.	.7023	0.0938		443.	.7022	0.0982		496.	.8046	0.0812		468.	.6959	0.0720	
479.	.7460	0.0965		517.	.7448	0.0955		578.	.8439	0.0728		541.	.7591	0.0715	
508.	.8098	0.0847		561.	.7944	0.0955		661.	.8786	0.0658		631.	.8084	0.0698	
718.	.8486	0.0751		759.	.8477	0.0841		744.	.8989	0.0595		721.	.8457	0.0639	
839.	.8799	0.0651		867.	.8980	0.0699		826.	.9185	0.0522		811.	.8776	0.0579	
957.	.9020	0.0609		1035.	.9237	0.0523		982.	.9402	0.0399		901.	.9009	0.0526	
1107.	.9286	0.0482		1122.	.9436	0.0419		1157.	.9526	0.0335		1041.	.9313	0.0443	
1496.	.9441	0.0393		1478.	.9588	0.0299		1405.	.9634	0.0246		1241.	.9499	0.0377	
1705.	.9543	0.0337		1644.	.9700	0.0242		1653.	.9719	0.0206		1532.	.9665	0.0396	
2303.	.9646	0.0279		2217.	.9743	0.0210		2046.	.9768	0.0179		1802.	.9729	0.0341	
2902.	.9712	0.0245		2956.	.9808	0.0176		2479.	.9804	0.0149		2252.	.9806	0.0201	
3500.	.9762	0.0223		3695.	.9838	0.0158		3305.	.9858	0.0125		2703.	.9858	0.0173	
4786.	.9804	0.0108		4644.	.9872	0.0132		4132.	.9873	0.0113		3604.	.9903	0.0147	
5983.	.9859	0.0171		5912.	.9902	0.0127		5744.	.9925	0.0100		4505.	.9920	0.0138	
7779.	.9882	0.0156		7300.	.9919	0.0112		7437.	.9943	0.0092		5406.	.9939	0.0129	
9573.	.9917	0.0142		9647.	.9946	0.0107		9000.	.9964	0.0096		7208.	.9947	0.0116	
11946.	.9962	0.0126		11824.	.9973	0.0098		11569.	.9982	0.0086		9910.	.9967	0.0112	
14359.	.9996	0.0103		14700.	.9993	0.0095		14048.	1.0000	0.0078		12613.	.9992	0.0107	
16752.	1.0000	0.0093		17737.	1.0000	0.0078		17353.	1.0000	0.0068		15316.	1.0000	0.0099	
19146.	1.0000	0.0084		20693.	1.0000	0.0073						18019.	.9992	0.0092	

BEST AVAILABLE COPY

X = 185.80			X = 190.10		
N	F	INTENSITY	N	F	INTENSITY
133.	.1849	0.0204	240.	.5442	0.0303
155.	.2049	0.0236	260.	.5803	0.0301
177.	.2443	0.0241	321.	.6177	0.0306
222.	.3153	0.0295	401.	.6787	0.0296
277.	.4013	0.0346	481.	.7298	0.0330
333.	.4917	0.0412	561.	.7796	0.0390
388.	.5749	0.0488	641.	.8207	0.0400
444.	.6374	0.0493	721.	.8580	0.0372
510.	.7024	0.0486	801.	.8842	0.0352
577.	.7569	0.0511	902.	.9128	0.0338
644.	.8169	0.0553	1002.	.9340	0.0305
770.	.8700	0.0538	1202.	.9577	0.0242
847.	.9098	0.0477	1402.	.9738	0.0198
900.	.9330	0.0394	1603.	.9838	0.0163
1109.	.9505	0.0355	2003.	.9913	0.0124
1331.	.9746	0.0277	2605.	.9964	0.0095
1553.	.9829	0.0232	3206.	.9973	0.0089
1806.	.9861	0.0178	4007.	.9984	0.0081
2219.	.9906	0.0149	5009.	1.0000	0.0076
2662.	.9933	0.0131	6010.	.9994	0.0079
3106.	.9951	0.0122			
3641.	.9969	0.0107			
4437.	.9969	0.0103			
5546.	.9984	0.0097			
7765.	.9991	0.0091			
10538.	.9996	0.0083			
13311.	1.0000	0.0082			

APPENDIX C

ERRATA FOR REPORT SMU-1-PU

page	line	
10	bottom	"96 inches" should "93 inches"
11	6	" $3.1672 \times 10^{-4}(x)$ " should be " $3.1627 \times 10^{-4}(x)$ "
11	6	" $6.5931 \times 10^{-6}(x^2)$ " should be " $6.5931 \times 10^{-7}(x^2)$ "
11	8	" $1.1944 \times 10^{-5}(x^2)$ " should be " $1.1994 \times 10^{-5}(x^2)$ "

GOVERNMENT AGENCIES

1. British Embassy
3100 Massachusetts Avenue, N.W.
Washington, D.C. 20008
ATTN: Mr. J. Barry Jamieson
Propulsion Officer
2. Central Intelligence Agency
Washington, D.C. 20505
ATTN: CRS/ADD/Publications
3. Institute for Defense Analyses
400 Army-Navy Drive
Arlington, Virginia 22202
ATTN: Dr. Hans G. Wolfhard,
Sen. Staff
4. Defense Documentation Center
Cameron Station
Alexandria, Virginia 22314
5. EPA Technical Center
Research Triangle Park
North Carolina 27711
ATTN: Dr. W. Herget, P-222
6. Esso Research and Engineering Company
Government Research Laboratory
P.O. Box 8
Linden, New Jersey 07036
ATTN: Dr. William F. Taylor
7. Arnold Air Force Station
Tennessee 36389
ATTN: AEDC (DYF)
8. Arnold Air Force Station
Tennessee 37389
ATTN: R.E. Smith, Jr., Chief
T-Cells Division
Engine Test Facility
9. Air Force Aero Propulsion Laboratory
Wright-Patterson Air Force Base
Ohio 45433
ATTN: STINFO Office
10. Air Force Eastern Test Range
MU-135
Patrick Air Force Base
Florida 32925
ATTN: AFETR Technical Library
11. Air Force Office of Scientific Research
Bolling Air Force Base, Building 410
Washington, D.C. 20332
ATTN: Dr. Joseph F. Nasi
12. Air Force Aero Propulsion Laboratory
Wright-Patterson AFB, Ohio 45433
ATTN: AFAPL/TBC
Dr. Kervyn Mach
13. Air Force Aero Propulsion Laboratory
Wright-Patterson AFB, Ohio 45433
ATTN: AFAPL/TBC
Francis R. Ostdek
14. Air Force Rocket Propulsion Laboratory
Department of Defense
Edwards AFB, California 93523
ATTN: LCG (Mr. Selph)
15. U.S. Army Air Mobility Research and
Development Laboratory
Eustis Directorate
Fort Eustis, Virginia 23604
ATTN: Propulsion Division
(SAVDL-EU-PP)
16. U.S. Army Artillery Combat
Developments Agency 73503
Fort Sill, Oklahoma
ATTN: Commanding Officer
17. U.S. Army Missile Command
Redstone Arsenal, Alabama 35809
ATTN: AMSM-RR
18. U.S. Army Missile Command
Redstone Scientific Information Center
Redstone Arsenal, Alabama 35809
ATTN: Chief, Document Section
19. Indiana State Library
140 North Senate Avenue
Indianapolis, Indiana 46204
ATTN: Patricia Matkovic
Reference Librarian
% Indiana Division
20. NASA Headquarters
600 Independence
Washington, D.C. 20546
ATTN: Dr. Gordon Banerian
21. NASA Headquarters
Aeronautical Propulsion Division
Code RL, Deputy Director
Office of Advanced Research & Technology
Washington, D.C. 20546
ATTN: Mr. Nelson F. Rekos
22. NASA Ames Research Center
Deputy Chief Aeronautics Division
Mail Stop 27-4
Moffett Field, California 94035
ATTN: Mr. Edward W. Perkins
23. NASA Ames Research Center
Aerodynamics Branch 227-8
Moffett Field, California 94305
ATTN: Mr. Ira R. Schwartz
24. NASA Lewis Research Center
21000 Brookpark Road
Cleveland, Ohio 44135
ATTN: D. Morris, Mail Stop 60-3
25. NASA Lewis Research Center
Hypersonic Propulsion Section
Mail Stop 6-1
21000 Brookpark Road
Cleveland, Ohio 44135
ATTN: Dr. Louis A. Povinelli
26. NASA Marshall Space Flight Center
S&E ASTN-P
Huntsville, Alabama 35812
ATTN: Mr. Keith Chandler
27. National Science Foundation
Engineering Energetics
Engineering Division
Washington, D.C. 20550
ATTN: Dr. George Lee
28. National Science Foundation
Engineering Energetics
Engineering Division
Washington, D.C. 20550
ATTN: Dr. M. Ojalvo
29. National Science Foundation
Engineering Energetics
Engineering Division
Washington, D.C. 20550
ATTN: Dr. Royal Rostenbach
30. Naval Air Development Center
Commanding Officer (AD-5)
Warminster, Pennsylvania 18974
ATTN: NADC Library
31. Naval Air Propulsion Test Center (R&T)
Trenton, New Jersey 08628
ATTN: Mr. Al Martino

AD-A037 441

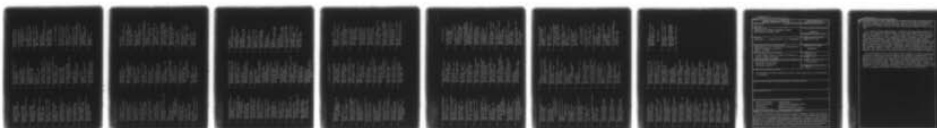
PURDUE UNIV LAFAYETTE IND PROJECT SQUID HEADQUARTERS F/G 20/4
LAMINARISCENT TURBULENT BOUNDARY LAYERS: EXPERIMENTS ON NOZZLE --ETC(U)
JAN 77 R L SIMPSON, C R SHACKLETON N00014-75-C-1143

UNCLASSIFIED

SQUID-SMU-2-PU

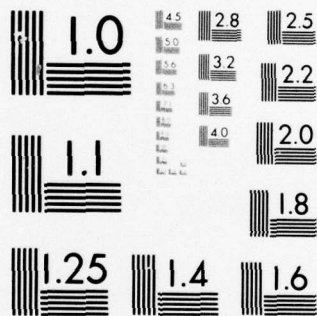
NL

2 OF 2
AD
A037441



END

DATE
FILMED
4 - 77



MICROCOPY RESOLUTION TEST CHART
NATIONAL BUREAU OF STANDARDS-1963-A

32. Naval Air Systems Command
Department of the Navy
Washington, D.C. 20360
ATTN: Research Administrator
AIR 310
33. Naval Air Systems Command
Department of the Navy
Washington, D.C. 20360
ATTN: Propulsion Technology Admin.
AIR 330
34. Naval Air Systems Command
Department of the Navy
Washington, D.C. 20360
ATTN: Technical Library Division
AIR 604
35. Naval Ammunition Depot
Research and Development Department
Building 190
Crane, Indiana 47522
ATTN: Mr. B.E. Douda
36. Naval Ordnance Laboratory Commander
White Oak
Silver Springs, Maryland 20910
ATTN: Library
37. Naval Ordnance Systems Command
Department of the Navy
Washington, D.C. 20360
ATTN: ORD 0331
38. Naval Postgraduate School
Department of Aeronautics, Code 57
Monterey, California 93940
ATTN: Dr. Allen E. Fuhs
39. Naval Postgraduate School
Library (Code 2124)
Monterey, California 93940
ATTN: Superintendent
40. Naval Postgraduate School
Monterey, California 93940
ATTN: Library (Code 0212)
41. Office of Naval Research Branch Office
1030 East Green Street
Pasadena, California 91106
ATTN: Dr. Rudolph J. Marcus
42. Office of Naval Research Branch Office
536 South Clark Street
Chicago, Illinois 60605
ATTN: Commander
43. Office of Naval Research Branch Office
495 Summer Street
Boston, Massachusetts 02210
ATTN: Commander
44. Office of Naval Research
Power Branch, Code 473
Department of the Navy
Arlington, Virginia 22217
45. Office of Naval Research
Fluid Dynamics Branch, Code 438
Department of the Navy
Washington, D.C. 22217
ATTN: Mr. Morton Cooper
46. Naval Research Lab
Code 7710
Washington, D.C. 20390
ATTN: W.W. Balwanz
47. Naval Research Laboratory Director
Washington, D.C. 20390
ATTN: Technical Information Division
48. Naval Research Laboratory Director
Washington, D.C. 20390
ATTN: Library Code 2629 (ONRL)
49. Naval Ship Research and Development Center
Annapolis Division
Annapolis, Maryland 21402
ATTN: Library, Code A214
50. Naval Ship Systems Command
Department of the Navy
Washington, D.C. 20360
ATTN: Technical Library
51. Naval Weapons Center Commander
China Lake, California 93555
ATTN: Airbreathing Propulsion Branch
Code 4583
52. Naval Weapons Center
Chemistry Division
China Lake, California 93555
ATTN: Dr. William S. McEwan
Code 605
53. Naval Weapons Center
Commander
China Lake, California 93555
ATTN: Technical Library
54. Naval Weapons Center
Code 608, Thermochemistry Group
China Lake, California 93555
ATTN: Mr. Edward W. Price, Head
55. Naval Weapons Laboratory
Dahlgren, Virginia 22448
ATTN: Technical Library
56. Naval Undersea Research and
Development Center
San Diego, California 92132
ATTN: Technical Library
Code 13110
57. Naval Underwater Systems Center
Fort Trumbull
New London, Connecticut 06320
ATTN: Technical Library
58. Naval Underwater Systems Center
Code 58-331
Newport, Rhode Island 02840
ATTN: Dr. Robert Lazar
59. Picatinny Arsenal
Commanding Officer
Dover, New Jersey 07801
ATTN: Technical Information Library
60. State Documents Section
Exchange and Gift Division
Washington, D.C. 20540
ATTN: Library of Congress
- U.S. INDUSTRIES AND LABORATORIES
61. AeroChem Research Laboratories, Inc.
P.O. Box 12
Princeton, New Jersey 08540
ATTN: Dr. Arthur Fontijn
62. AeroChem Research Laboratories, Inc.
P.O. Box 12
Princeton, New Jersey 08540
ATTN: Library
63. Aerojet Liquid Rocket Company
P.O. Box 13222
Sacramento, California 95813
ATTN: Technical Information Center
64. Aeronautical Research Association
of Princeton
50 Washington Road
Princeton, New Jersey 08540
ATTN: Dr. C. Donaldson
65. AeroProjects, Inc.
West Chester
Pennsylvania 19380

66. The Aerospace Corporation
P.O. Box 92957
Los Angeles, California 90009
ATTN: Mr. Alexander Muraszew
67. Atlantic Research Corporation
5390 Cherokee Avenue
Alexandria, Virginia 22314
ATTN: Dr. Andrej Macek
68. Atlantic Research Corporation
5390 Cherokee Avenue
Alexandria, Virginia 22314
ATTN: Librarian
69. Atlantic Research Corporation
5390 Cherokee Avenue
Alexandria, Virginia 22314
ATTN: Dr. Kermit E. Woodcock
Manager, Propulsion
70. Avco Everett Research Laboratory
Everett, Massachusetts 02149
ATTN: Librarian
71. Avco Lycoming Corporation
550 South Main Street
Stratford, Connecticut 06497
ATTN: Mr. John W. Schrader
72. Ballistics Research Laboratory
Commanding Officer
Aberdeen Proving Ground, Maryland 21005
ATTN: Librarian
73. Battelle
Columbus Laboratories
505 King Avenue
Columbus, Ohio 43201
ATTN: Mr. Abbott A. Putnam
Atmospheric Chemistry &
Combustion Systems Division
74. Beech Aircraft Corporation
9709 East Central
Wichita, Kansas 67201
ATTN: William M. Byrne, Jr.
75. Fell Aerospace Company
P.O. Box 1
Buffalo, New York 14240
ATTN: Technical Library
76. Bureau of Mines
Bartlesville Energy Research Center
Box 1398
Bartlesville, Oklahoma 74003
77. Calspan Corporation
4455 Genessee Street
Buffalo, New York 14221
ATTN: Head Librarian
78. Computer Genetics Corporation
Wakefield, Massachusetts 01880
ATTN: Mr. Donald Leonard
Technical Director
79. Convair Aerospace Division
Manager of Propulsion
P.O. Box 748
Fort Worth, Texas 76101
ATTN: L. H. Schreiber
80. Detroit Diesel Allison Division
P.O. Box 894
Indianapolis, Indiana 46206
ATTN: Dr. Sanford Fleeter
81. Dynalysis of Princeton
20 Nassau Street
Princeton, New Jersey 08540
ATTN: Dr. H.J. Herring
82. Fairchild Industries
Fairchild Republic Division
Farmingdale, New York 11735
ATTN: Engineering Library
83. Flame Research, Inc.
P.O. Box 10502
Pittsburgh, Pennsylvania 15235
ATTN: Dr. John Manton
84. Forest Fire and Engineering Research
Pacific Southwest Forest & Range
Experiment Station
P.O. Box 245
Berkeley, California 94701
ATTN: Assistant Director
85. Garrett Corporation
AirResearch Manufacturing Company
Sky Harbor Airport
402 South 36th Street
Phoenix, Arizona 85034
ATTN: Mr. Aldo L. Romanin, Mgr.
Aircraft Propulsion Engine
Product Line
86. General Dynamics
Electro Dynamic Division
P.O. Box 2507
Pomona, California 91766
ATTN: Library MZ 620
87. General Dynamics
P.O. Box 748
Fort Worth, Texas 76101
ATTN: Technical Library MZ 2246
88. General Electric Company
AEG Technical Information Center
Mail Drop N-32, Building 700
Cincinnati, Ohio 45215
ATTN: J.J. Brady
89. General Electric Company
SP0-Bldg, 174AE
1000 Western Avenue
West Lynn, Massachusetts 01910
ATTN: Mr. W. Bruce Gist
90. General Electric Space Sciences Lab
Valley Forge Space Technology Center
Room M-9144
P.O. Box 8555
Philadelphia, Pennsylvania 19101
ATTN: Dr. Theodore Baurer
91. General Motors Corporation
Detroit Diesel Allison Division
P.O. Box 894
Indianapolis, Indiana 46206
ATTN: Mr. P.C. Tram
92. General Motors Technical Center
Passenger Car Turbine Development
General Motors Engineering Staff
Warren, Michigan 48090
ATTN: T.F. Nagey, Director
93. Grumman Aerospace Corporation
Manager Space Vehicle Development
Bethpage, New York 11714
ATTN: Mr. O.S. Williams
94. Mr. Daniel L. Harshman
11131 Embassy Drive
Cincinnati, Ohio 45240
95. Hercules Incorporated
Allegany Ballistics Laboratory
P.O. Box 210
Cumberland, Maryland 21502
ATTN: Mrs. Louise S. Derrick
Librarian
96. Hercules Incorporated
P.O. Box 98
Magna, Utah 84044
ATTN: Library 100-H

97. LTV Vought Aeronautics Company
Flight Technology, Project Engineer
P.O. Box 5907
Dallas, Texas 75222
ATTN: Mr. James C. Utterback
98. Lockheed Aircraft Corporation
Lockheed Missiles and Space Company
Huntsville, Alabama 35804
ATTN: John M. Banefield
Supervisor Propulsion
99. Lockheed-Gear Company
Dept. 72-47, Zone 259
Marietta, Georgia 30060
ATTN: William A. French
100. Lockheed Missiles and Space Company
2251 Hanover Street
Palo Alto, California 94304
ATTN: Palo Alto Library 52-52
101. Lockheed Propulsion Company
Scientific and Technical Library
P.O. Box 111
Redlands, California 92373
ATTN: Head Librarian
102. Los Alamos Scientific Laboratory
P.O. Box 1663
Los Alamos, New Mexico 97544
ATTN: J. Arthur Freed
103. The Marquardt Company
CCI Aerospace Corporation
16555 Saticoy Street
Van Nuys, California 91409
ATTN: Library
104. Martin-Marietta Corporation
P.O. Box 179
Denver, Colorado 90201
ATTN: Research Library 6617
105. Martin-Marietta Corporation
Orlando Division
P.O. Box 5837
Orlando, Florida 32805
ATTN: Engineering Library, mp-30
106. McDonnell Aircraft Company
P.O. Box 516
St. Louis, Missouri 63166
ATTN: Research & Engineering Library
Dept. 218 - Bldg. 101
107. McDonnell Douglas Corporation
Project Propulsion Engineer
Dept. 243, Bldg. 66, Level 25
P.O. Box 516
St. Louis, Missouri 63166
ATTN: Mr. William C. Paterson
108. McDonnell Douglas Astronautics Company
5301 Bolsa Avenue
Huntington Beach, California 92647
ATTN: A3-328 Technical Library
109. Nielsen Engineering and Research, Inc.
510 Clyde Avenue
Mountain View, California 94040
ATTN: Dr. Jack N. Nielsen
110. Northrop Corporation
Ventura Division
1515 Rancho Conejo Boulevard
Newbury Park, California 91230
ATTN: Technical Information Center
111. Mr. J. Richard Perrin
16261 Darcia Avenue
Encino, California 91316
112. Philco-Ford Corporation
Aeronutronic Division
Ford Road
Newport Beach, California 92663
ATTN: Technical Information Center
113. Pratt and Whitney Aircraft
Project Engineer, Advanced
Military System
Engineering Department - 28
East Hartford, Connecticut 06108
ATTN: Mr. Donald S. Rudolph
114. Pratt and Whitney Aircraft Division
United Aircraft Company
400 South Main Street
East Hartford, Connecticut 06108
ATTN: Mr. Dana B. Waring
Manager-Product Technology
115. Pratt and Whitney Aircraft
Program Manager, Advanced
Military Engineer
Engineering Department - 28
East Hartford, Connecticut 06108
ATTN: Dr. Robert I. Strough
116. Pratt and Whitney Aircraft
Florida Research and Development Company
P.O. Box 2691
West Palm Beach, Florida 33402
ATTN: Mr. William R. Alley
Chief of Applied Research
117. Rocket Research Corporation
11441 Willow Road
Redmond, Washington 98052
ATTN: Thomas A. Groudie
118. Rocketdyne Division
North American Rockwell
6633 Canoga Avenue
Canoga Park, California 91304
ATTN: Technical Information Center
D 596-108
119. Sandia Laboratories
P.O. Box 969
Livermore, California 94550
ATTN: Dr. Dan Hartley, Div. 8115
120. Sandia Laboratories
Livermore, California 94550
ATTN: Robert Gallagher
121. Sandia Laboratories
P.O. Box 5800
Albuquerque, New Mexico 87115
ATTN: Technical Library, 3141
122. Solar
2200 Pacific Highway
San Diego, California 92112
ATTN: Librarian
123. Standard Oil Company (Indiana)
P.O. Box 400
Naperville, Illinois 60540
ATTN: R. E. Pritz
124. Stauffer Chemical Company
Richmond, California 94802
ATTN: Dr. J. H. Morgenthaler
125. Teledyne CAE
1330 Laskey Road
Toledo, Ohio 43601
ATTN: Technical Library
126. TRW Systems
One Space Park
Redondo Beach, California 90278
ATTN: Mr. F.E. Fendell (R1/1004)
127. TRW Systems Group
One Space Park
Bldg. 0-1, Room 2080
Redondo Beach, California 90278
ATTN: Mr. Donald H. Lee Manager
128. United Technologies Research Center
East Hartford, Connecticut 06108
ATTN: Librarian
129. Valley Forge Sapce Technology Center
P.O. Box 8555
Philadelphia, Pennsylvania 19101
ATTN: Dr. Bert Zauderer
130. Vought Missiles and Space Company
P.O. Box 6267
Dallas, Texas 75222
ATTN: Library - 3-41000

U.S. COLLEGES AND UNIVERSITIES

131. Boston College
Department of Chemistry
Chestnut Hill, Massachusetts 02167
ATTN: Rev. Donald MacLean, S.J.
Associate Professor
132. Brown University
Division of Engineering
Box D
Providence, Rhode Island 02912
ATTN: Dr. R. A. Dobbins
133. California Institute of Technology
Department of Chemical Engineering
Pasadena, California 91109
ATTN: Professor W. H. Corcoran
134. California Institute of Technology
Jet Propulsion Laboratory
4800 Oak Grove Drive
Pasadena, California 91103
ATTN: Library
135. University of California, San Diego
Dept. of Engineering Physics
P.O. Box 109
La Jolla, California 92037
ATTN: Professor S.S. Penner
136. University of California
School of Engineering and
Applied Science
7513 Boelter Hall
Los Angeles, California 90024
ATTN: Engineering Reports Group
137. University of California
Lawrence Radiation Laboratory
P.O. Box 808
Livermore, California 94550
ATTN: Technical Information Dept. L-3
138. University of California
General Library
Berkeley, California 94720
ATTN: Documents Department
139. Case Western Reserve University
10900 Euclid Avenue
Cleveland, Ohio 44106
ATTN: Sears Library - Reports
Department
140. Case Western Reserve University
Division of Fluid Thermal and
Aerospace Sciences
Cleveland, Ohio 44106
ATTN: Professor Eli Reshotko
141. Colorado State University
Engineering Research Center
Fort Collins, Colorado 80521
ATTN: Mr. V. A. Sandborn
142. The University of Connecticut
Department of Mechanical Engineering
U-139
Storrs, Connecticut 06268
ATTN: Professor E. K. Dabora
143. Cooper Union
School of Engineering and Science
Cooper Square
New York, New York 10003
ATTN: Dr. Wallace Chintz
Associate Professor of ME
144. Cornell University
Department of Chemistry
Ithaca, New York 14850
ATTN: Professor Simon H. Bauer
145. Franklin Institute Research Laboratories
Philadelphia, Pennsylvania 19103
ATTN: Dr. G.P. Wachtell
146. George Washington University
Washington, D.C. 20052
ATTN: Dr. Robert Goulard
Dept. of Civil, Mechanical and
Environmental Engineering
147. George Washington University Library
Washington, D.C. 20006
ATTN: Reports Section
148. Georgia Institute of Technology
Atlanta, Georgia 30332
ATTN: Price Gilbert Memorial Library
149. Georgia Institute of Technology
School of Aerospace Engineering
Atlanta, Georgia 30332
ATTN: Dr. Ben T. Zinn
150. University of Illinois
Department of Energy Engineering
Box 4348
Chicago, Illinois 60680
ATTN: Professor Paul H. Chung
151. University of Illinois
College of Engineering
Department of Energy Engineering
Chicago, Illinois 60680
ATTN: Dr. D. S. Hacker
152. The Johns Hopkins University
Applied Physics Laboratory
Johns Hopkins Road
Laurel, Maryland 20810
ATTN: Chemical Propulsion
Information Agency
153. The Johns Hopkins University
Applied Physics Laboratory
Johns Hopkins Road
Laurel, Maryland 20810
ATTN: Document Librarian
154. The Johns Hopkins University
Applied Physics Laboratory
Johns Hopkins Road
Laurel, Maryland 20810
ATTN: Dr. A. A. Westenberg
155. University of Kentucky
Department of Mechanical Engineering
Lexington, Kentucky 40506
ATTN: Dr. Robert E. Peck
156. Massachusetts Institute of Technology
Department of Chemical Engineering
Cambridge, Massachusetts 02139
ATTN: Dr. Jack B. Howard
157. Massachusetts Institute of Technology
Libraries, Room 14 E-210
Cambridge, Massachusetts 02139
ATTN: Technical Reports
158. Massachusetts Institute of Technology
Room 10-408
Cambridge, Massachusetts 02139
ATTN: Engineering Technical Reports

159. Massachusetts Institute of Technology
Dept. of Mechanical Engineering
Room 3-350
Cambridge, Massachusetts 02139
ATTN: Dr. M. Cardillo
160. Massachusetts Institute of Technology
Dept. of Mechanical Engineering
Room 3-246
Cambridge, Massachusetts 02139
ATTN: Professor James Fay
161. Midwest Research Institute
425 Volker Boulevard
Kansas City, Missouri 64100
ATTN: Dr. T. A. Milne
162. New Mexico State University
Dept. of Mechanical Engineering
Box 3450
Las Cruces, New Mexico 88003
ATTN: Dr. Dennis M. Zallen
163. New York Institute of Technology
Wheatley Road
Old Westbury, New York 11568
ATTN: Dr. Fox
164. University of North Carolina
Periodicals and Serials Division
Drawer 870 Library
Chapel Hill, North Carolina 27514
ATTN: Mr. Stephen Berk
165. University of Notre Dame
Serials Record
Memorial Library
Notre Dame, Indiana 46556
ATTN: B. McIntosh
166. University of Notre Dame
College of Engineering
Notre Dame, Indiana 46556
ATTN: Dr. Stuart T. McComas
Assistant Dean for Research
and Special Projects
167. Ohio State University
Dept. of Chemical Engineering
140 West 19th Avenue
Columbus, Ohio 43210
ATTN: Dr. Robert S. Brodkey
168. The Pennsylvania State University
Room 207, Old Main Building
University Park, Pennsylvania 16802
ATTN: Office of Vice President
for Research
169. Princeton University
Dept. of Aerospace and Mechanical
Sciences
James Forrestal Campus
Princeton, New Jersey 08540
ATTN: Dr. Martin Summerfield
170. Princeton University
James Forrestal Campus Library
P.O. Box 710
Princeton, New Jersey 08540
ATTN: V. N. Simosko, Librarian
171. Rice University
Welch Professor of Chemistry
Houston, Texas 77001
ATTN: Dr. Joseph L. Franklin
172. University of Rochester
Dept. of Chemical Engineering
Rochester, New York 14627
ATTN: Dr. John R. Ferron
173. Stanford University
Dept. of Aeronautics and Astronautics
Stanford, California 94305
ATTN: Dr. Walter G. Vincenti
174. State University of New York - Buffalo
Dept. of Mechanical Engineering
228 Parker Engineering Building
Buffalo, New York 14214
ATTN: Dr. George Rudinger
175. Stevens Institute of Technology
Department of Mechanical Engineering
Castle Point Station
Hoboken, New Jersey 07030
ATTN: Professor Fred Sisto
176. University of Virginia
Department of Aerospace Engineering
School of Engineering and Applied Science
Charlottesville, Virginia 22901
ATTN: Dr. John E. Scott
177. University of Virginia
Science/Technology Information Center
Charlottesville, Virginia 22901
ATTN: Dr. Richard H. Austin
178. Yale University
Mason Laboratory
9 Hillhouse Avenue
New Haven, Connecticut 06520
ATTN: Professor Peter P. Wegener
- FOREIGN INSTITUTIONS
179. A/S Kongsberg Vaapenfabrikk
Gas Turbine Division
3601 Konsber, NORWAY
ATTN: R.E. Stanley
Senior Aerodynamicist
180. Conservatoire National des Arts
et Metiers
292, Rue Saint Martin
75141 Paris Cedex 03, FRANCE
ATTN: Professor J. Gossee
Chaire de Thermique
181. DFVLR-Forschungszentrum Gottingen
Institut Fur Stromungsmechanik
Abteilung Theoretische Gashynamik
D-3400 Gottingen
Bunsenstrabe 10, GERMANY
ATTN: Professor Klaus Oswatitsch
182. Ecole Royale Militaire
30 Avenue de la Resaissance
Bruxelles B-1040, BELGIUM
ATTN: Professor Emile Tits
183. Fysisch Laboratorium
Fijksuniversiteit Utrecht
Sorbonnelaan, Utrecht,
THE NETHERLANDS
ATTN: Dr. F. Van der Valk
184. Imperial College
Department of Chemical Engineering
London SW7, ENGLAND
ATTN: Professor F. J. Weinberg
185. Imperial College of Science
and Technology
Department of Mechanical Engineering
Exhibition Road
London, SW7, ENGLAND
ATTN: Professor Gaydon
186. Imperial College of Science
and Technology
Department of Mechanical Engineering
Exhibition Road
London SW7, ENGLAND
ATTN: D. E. Spalding
- 187/1 Laboratoire de Mecanique des Fluides
36, Route de Dardilly, 36
B.P. No. 17
69130 Ecully, FRANCE
ATTN: G. Assassa

- 187/2 Laboratoire de Mecanique des Fluides
Ecole Centrale Lyonnaise
36, Route de Dardilly
69130 Ecully, FRANCE
ATTN: Dr. K. Papiliou
188. Ministry of Defense
Main Building, Room 2165
Whitehall Gardens
London SW1, ENGLAND
ATTN: Mr. L.D. Nicholson ED, idc
Vice Controller of Aircraft
Procurement Executive
189. Mitglied des Vorstands der Fried
Krupp GmbH
43 Essen, Altendorferstrabe 103
GERMANY
ATTN: Professor Dr.-Ing.
Wilhelm Dettmering
190. National Aerospace (NLR)
Voorsterweg 31
Noord-Oost-Polder-Emmelord
THE NETHERLANDS
ATTN: Mr. F. Jaarsma
191. National Research Council
Division of Mechanical Engineering
Montreal Road, Ottawa
Ontario, CANADA KIA 0R6
ATTN: Dr. R.B. Whyte
192. Nissan Motor Co., LTD.
3-5-1, Momoi, Suginami-Ku
Tokyo, JAPAN 167
ATTN: Dr. Y. Toda
193. Norwegian Defense Research Establishment
Superintendent NDRE
P.O. Box 25
2007 Kjeller, NORWAY
ATTN: Mr. T. Krog
194. ONERA
Energie and Propulsion
29 Avenue de la Division Leclure
92 Chatillon sous Bagneux, FRANCE
ATTN: Mr. M. Barre
195. ONERA
Energie and Propulsion
29 Avenue de la Division Leclure
92 Chatillon sous Bagneux, FRANCE
ATTN: Mr. J. Fabri
196. ONERA
Energie and Propulsion
29 Avenue de la Division Leclure
92 Chatillon sous Bagneux, FRANCE
ATTN: Mr. Viaud
197. ONERA-DED
External Relations and Documentation
Department
29, Avenue de la Division Leclure
92320 Chatillon, sous Bagneux, FRANCE
ATTN: Mr. M. Salmon
198. Orta Dogu Teknik Universitesi
Mechanical Engineering Department
Ankara, TURKEY
ATTN: Professor H. Sezgen
199. Queen Mary College
Department of Mechanical Engineering
Thile Eld Road
London E1, ENGLAND
ATTN: Professor M. W. Thring
200. Rolls-Royce (1971) Limited
Derby Engine Division
P.O. Box 31
Derby DE2 8BJ
London, ENGLAND
ATTN: C. Freeman, Installation
Research Department
201. Rome University
Via Bradano 28
00199 Rome, ITALY
ATTN: Professor Gaetano Salvatore
202. Sener
Departamento de Investigation
Km. 22.500 de la antigua carretera
Madrid - Barcelona, SPAIN
ATTN: Mr. J. T. Diez Roche
203. Service Technique Aeronautique Moteurs
4 Avenue de la Parte d'Issy
75753 Paris Cedex 15, FRANCE
ATTN: Mr. M. Pianko, Ing. en chef
204. The University of Sheffield
Dept. of Chemical Engineering
and Fuel Technology
Mappin Street, Sheffield S1 3JD
ENGLAND
ATTN: Dr. Norman Chigier
205. Sophia University
Science and Engineering Faculty
Kioi 7 Tokyo-Chiyoda JAPAN 102
ATTN: Professor M. Susuki
206. The University of Sydney
Dept. of Mechanical Engineering
N.S.W. 2006
Sydney, AUSTRALIA
ATTN: Professor R. W. Bilger
207. Technical University of Denmark
Fluid Mechanics Department
Building 404 2800 Lyngby
DK-DENMARK
ATTN: Professor K. Refslund
208. University of Leeds
Leeds, ENGLAND
ATTN: Professor Dixon-Lewis
209. Universite de Poitiers Laboratoire
D'energetique et de Detonique
(L.A. au C.N.R.S. No. 193)
ENSMA - 86034 Poitiers, FRANCE
ATTN: Professor N. Manson
210. University of Tokyo
Department of Reaction Chemistry
Faculty of Engineering
Bunkyo-ku
Tokyo, JAPAN 113
ATTN: Professor T. Hikita
211. Vrije Universiteit Brussel
Fac. Toeg. Wetenschh.
A. Buyllaan 105
1050 Brussels, BELGIUM
ATTN: Ch. Hirsch
- PROJECT SQUID CONTRACTORS
1975-76 and 1976-77 (New)
212. AeroChem Research Laboratory, Inc.
Reaction Kinetics Group
P.O. Box 12
Princeton, New Jersey 08540
ATTN: Dr. Arthur Fontijn
213. Aeronautical Research Associates of
Princeton, Inc.
P.O. Box 2229
50 Washington Road
Princeton, New Jersey 08540
ATTN: Dr. Ashok K. Varma
214. California Institute of Technology
Div. of Engineering and
Applied Science
Mail Stop 205-50
Pasadena, California 91109
ATTN: Dr. Anatol Roshko
215. Case Western Reserve University
Div. of Fluid, Thermal and Aerospace
Sciences
Cleveland, Ohio 44106
ATTN: Dr. J.S. T'ien

216. Colorado State University
Engineering Research Center
Foothills Campus
Fort Collins, Colorado 80521
ATTN: Dr. Willy Z. Sadeh
217. General Electric Company
Corporate Research and Development
P.O. Box 8
Schenectady, New York 12301
ATTN: Dr. Marshall Lapp
218. Massachusetts Institute of Technology
Chemistry Department, Room 6-123
77 Massachusetts Avenue
Cambridge, Massachusetts 02139
ATTN: Dr. John Ross
219. Michigan State University
Department of Mechanical Engineering
East Lansing, Michigan 48824
ATTN: Dr. John Foss
220. Pennsylvania State University
Applied Research Laboratory
University Park, Pennsylvania 16802
ATTN: Dr. Edgar P. Bruce
221. Polytechnic Institute of New York
Department of Aerospace Engineering
and Applied Mechanics
Farmingdale, New York 11735
ATTN: Dr. Samuel Lederman
222. Southern Methodist University
Thermal and Fluid Sciences Center
Institute of Technology
Dallas, Texas 75275
ATTN: Dr. Roger L. Simpson
223. Stanford University
Mechanical Engineering Department
Stanford, California 94305
ATTN: Dr. James P. Johnston
224. Stanford University
Mechanical Engineering Department
Stanford, California 94305
ATTN: Dr. S. J. Kline
225. Stanford University
Mechanical Engineering Department
Stanford, California 94305
ATTN: Dr. Sidney Self
226. TRW Systems
Engineering Sciences Laboratory
One Space Park
Redondo Beach, California 90278
ATTN: Dr. J. E. Broadwell
227. United Technologies Research Center
400 Main Street
East Hartford, Connecticut 06108
ATTN: Mr. Franklin O. Carta
228. United Technologies Research Center
400 Main Street
East Hartford, Connecticut 06108
ATTN: Dr. Alan C. Eckbreth
229. University of California - San Diego
Department of Aerospace and
Mechanical Engineering
La Jolla, California 92037
ATTN: Dr. Paul Libby
230. University of Colorado
Department of Aerospace
Engineering Sciences
Boulder, Colorado 80304
ATTN: Dr. Mahinder S. Uberoi
231. University of Michigan
Department of Aerospace Engineering
Ann Arbor, Michigan 48105
ATTN: Dr. T. C. Adamson, Jr.
232. University of Michigan
Department of Aerospace Engineering
Ann Arbor, Michigan 48105
ATTN: Dr. Martin Sichel
233. University of Missouri - Columbia
Department of Chemistry
Columbia, Missouri 65201
ATTN: Dr. Anthony Dean
234. University of Southern California
Department of Aerospace Engineering
University Park
Los Angeles, California 90007
ATTN: Dr. F. K. Browand
235. University of Washington
Department of Mechanical Engineering
Seattle, Washington 98195
ATTN: Dr. F.B. Gessner
236. Virginia Polytechnic Institute and
State University
Mechanical Engineering Department
Blacksburg, Virginia 24601
ATTN: Dr. Walter F. O'Brien, Jr.
237. Virginia Polytechnic Institute and
State University
Mechanical Engineering Department
Blacksburg, Virginia 24061
ATTN: Dr. Hal L. Moses
238. Yale University
Engineering and Applied Science
Mason Laboratory
New Haven, Connecticut 06520
ATTN: Dr. John B. Fenn
239. School of Aeronautics and Astronautics
Grissom Hall
West Lafayette, Indiana 47907
ATTN: Library
240. School of Mechanical Engineering
Mechanical Engineering Building
West Lafayette, Indiana 47907
ATTN: Library
- 241-250. Purdue University Advisors

Unclassified

SECURITY CLASSIFICATION OF THIS PAGE (When Data Entered)

REPORT DOCUMENTATION PAGE		READ INSTRUCTIONS BEFORE COMPLETING FORM
1. REPORT NUMBER SMU-2-PU ✓	2. GOVT ACCESSION NO.	3. RECIPIENT'S CATALOG NUMBER
4. TITLE (and Subtitle) LAMINARISCENT TURBULENT BOUNDARY LAYERS: EXPERIMENTS ON NOZZLE FLOWS		5. TYPE OF REPORT & PERIOD COVERED Technical
		6. PERFORMING ORG. REPORT NUMBER
7. AUTHOR(s) Professor R. L. Simpson and Mr. C. R. Shackleton		8. CONTRACT OR GRANT NUMBER(s) N00014-75-C-1143 ✓
9. PERFORMING ORGANIZATION NAME AND ADDRESS Department of Civil and Mechanical Engineering ✓ Southern Methodist University Dallas, TX 75275		10. PROGRAM ELEMENT, PROJECT, TASK AREA & WORK UNIT NUMBERS NR-098-038
11. CONTROLLING OFFICE NAME AND ADDRESS Project SQUID, Thermal Science and Propulsion Center, Purdue University West Lafayette, IN 47907		12. REPORT DATE January 1977
		13. NUMBER OF PAGES 87
14. MONITORING AGENCY NAME & ADDRESS (if different from Controlling Office) Office of Naval Research Department of the Navy Arlington, VA 22217		15. SECURITY CLASS. (of this report) Unclassified
		15a. DECLASSIFICATION/DOWNGRADING SCHEDULE
16. DISTRIBUTION STATEMENT (of this Report) This document has been approved for public release and sale; its distribution is unlimited.		
17. DISTRIBUTION STATEMENT (of the abstract entered in Block 20, if different from Report)		
18. SUPPLEMENTARY NOTES		
19. KEY WORDS (Continue on reverse side if necessary and identify by block number) Bursting frequency Intermittency Cross-correlation Laminariscient boundary layers Dissipation Turbulence intensities Entrainment Velocity fluctuation spectra Hot-film anemometer Viscous sublayer structure		
20. ABSTRACT (Continue on reverse side if necessary and identify by block number) Because a turbulent boundary layer in a nozzle undergoes strong acceleration, a laminariscient boundary layer with the benefit of a lower surface heat transfer rate can result for some short distance. Here, and in a previous report (Simpson and Wallace, 1975) several phenomena which accompany laminarescence produced by strong acceleration are examined for nozzle-flow and sink-flow accelerational distributions, respectively. Several different type measurements of the structure of two nozzle-type flows are reported to determine how an initially normal		

Unclassified

SECURITY CLASSIFICATION OF THIS PAGE (When Data Entered)

Unclassified

SECURITY CLASSIFICATION OF THIS PAGE(When Data Entered)

20. turbulent boundary layer approaches the laminar-like state, including mean velocity and Reynolds stresses profiles, spectra, turbulent/non-turbulent interfacial structure, and wall bursting and sublayer spanwise spatial structure.

As a result of these experiments, it appears that the surface skin-friction is not reduced to laminar values in sink flows unless $K(=\nu U_{\infty}^{-2} dU_{\infty}/dx)$ is greater than about 3.6×10^{-6} . In nozzle-type flows, K must also be greater than this value over a short distance in order to produce a short relaminarized region downstream. The large-eddy structure of the outer region governs the bursting frequency, the intermittent bulge passage frequency, and influences the wall flow behavior downstream. After the cessation of entrainment of free-stream fluid, these frequencies approach constant values. The wall spanwise structure appears to lag behind local conditions and to reflect upstream flow behavior. After retransition to a low acceleration turbulent boundary layer downstream, much larger spanwise scale structures are observed.

The entrainment rate of non-turbulent fluid decreases to zero at about the streamwise location at which the shape factor reaches a minimum value. The cessation of entrainment by the eruption and engulfment action of the large eddies can be traced to the reduction of available turbulence energy for diffusion to free-stream fluid. This reduction of available energy is due to the negative normal stresses turbulence energy production term. Spectral distributions of the streamwise fluctuation $F(n)$ possess a frequency region where $nF(n)$ is constant for laminar-like boundary layers at large K values.

Unclassified

SECURITY CLASSIFICATION OF THIS PAGE(When Data Entered)